

ISSN • 2708-6437 (Online)  
• 2708-6429 (Print)

# Journal of Engineering Advancements

**Editor-in-Chief:**

**Prof. Dr. Mohammad Mashud**

**Volume 02 Issue 04**

---



**Published by:**  
**SciEn Publishing Group**

# Journal of Engineering Advancements

Apt. # 6 C-D, House # 191  
Road # 9/A, Dhanmondi R/A  
Dhaka-1209, Bangladesh

Email: [jea@scienpg.com](mailto:jea@scienpg.com)

Website: [www.scienpg.com/jea/](http://www.scienpg.com/jea/)

## *Editor-in-Chief*

Prof. Dr. Mohammad Mashud  
Khulna University of Engineering & Technology  
Khulna-9203, Bangladesh.  
Tel: +880-41-769468 Ext. 405  
Email: [mdmashud@me.kuet.ac.bd](mailto:mdmashud@me.kuet.ac.bd)

## *Executive Editors*

Dr. Md. Arifuzzaman  
Khulna University of Engineering & Technology  
Khulna-9203, Bangladesh.  
Email: [arif48@me.kuet.ac.bd](mailto:arif48@me.kuet.ac.bd)

Dr. Md. Shariful Islam  
Khulna University of Engineering & Technology  
Khulna-9203, Bangladesh.  
Email: [msislam@me.kuet.ac.bd](mailto:msislam@me.kuet.ac.bd)

## *Editors*

Dr. Abul Mukid Mohammad Mukaddes  
Shahjalal University of Science and Technology  
Email: [mukaddes1975@gmail.com](mailto:mukaddes1975@gmail.com)  
Bangladesh

Dr. Md. Rashedul H. Sarker  
University of Indianapolis  
Email: [sarkerm@indy.edu](mailto:sarkerm@indy.edu)  
USA

Dr. Chu Chi Ming  
University Malaysia Sabah  
Email: [chrischu@ums.edu.my](mailto:chrischu@ums.edu.my)  
Malaysia

Dr. Seock Sam Kim  
University Malaysia Sabah  
Email: [sskim@ums.edu.my](mailto:sskim@ums.edu.my)  
Malaysia

Dr. Mohammad H. Rahman  
University of Wisconsin-Milwaukee  
Email: [rahmanmh@uwm.edu](mailto:rahmanmh@uwm.edu)  
USA

Dr. Sabuj Mallik  
University of Derby  
Email: [s.mallik@derby.ac.uk](mailto:s.mallik@derby.ac.uk)  
UK

Dr. Sivakumar Kumaresan  
University Malaysia Sabah  
Email: [shiva@ums.edu.my](mailto:shiva@ums.edu.my)  
Malaysia

Dr. Mohd Suffian Bin Misaran  
University Malaysia Sabah  
Email: [suffian@ums.edu.my](mailto:suffian@ums.edu.my)  
Malaysia

Dr. Md. Mizanur Rahman  
World University of Bangladesh  
Email: [mizanur.rahman@mte.wub.edu.bd](mailto:mizanur.rahman@mte.wub.edu.bd)  
Bangladesh

Dr. Zahir Uddin Ahmed  
Khulna University of Engineering & Technology  
Email: [zuahmed@me.kuet.ac.bd](mailto:zuahmed@me.kuet.ac.bd)  
Bangladesh

Dr. Riaz U. Ahmed  
University of Wisconsin-Green Bay  
Email: [ahmedm@uwgb.edu](mailto:ahmedm@uwgb.edu)  
USA

Dr. Mohammad Ilias Inam  
Khulna University of Engineering & Technology  
Email: [iliasinam@me.kuet.ac.bd](mailto:iliasinam@me.kuet.ac.bd)  
Bangladesh

Dr. Kazi Mostafijur Rahman  
Khulna University of Engineering & Technology  
Email: [mostafij@me.kuet.ac.bd](mailto:mostafij@me.kuet.ac.bd)  
Bangladesh

Dr. Md. Mahfuz Sarwar  
AECOM  
Email: [mahfuzsarwar@yahoo.com](mailto:mahfuzsarwar@yahoo.com)  
Australia



Published in: December 2021  
Published by: SciEn Publishing Group

Dr. Md. Abdullah Al Bari  
Khulna University of Engineering & Technology  
Email: [abdullahalbari@me.kuet.ac.bd](mailto:abdullahalbari@me.kuet.ac.bd)  
Bangladesh

# Journal of Engineering Advancements

Volume 02, Issue 04

December 2021

## CONTENTS

### Original Articles

01. Numerical and Experimental Study on Optimization of Coil Springs used in Vehicles' Suspension System  
*Mostafizur Rahman, Saeem Bin Abdullah* 169
02. Investigation of Mechanical Properties of Banana-Glass Fiber Reinforced Hybrid Composites  
*Kazi Jubair, Md Shariful Islam, Dipto Chakraborty* 175
03. Numerical Analysis of Natural Convection Heat Transfer Inside an Inverted T-Shaped Cavity Filled with Nanofluid  
*Gopal Sen, Mohammad Ilias Inam* 180
04. Assessment of Arsenic and Copper Pollution of the Benya Lagoon, Ghana By Neutron Activation Analysis  
*Michael Kwame Vowotor, Raymond Edziah, Samuel Sonko Sackey, Emmanuel Kofi Amewode, Sandra Baaba Frempong* 189
05. A Review of Methodological Approaches and Modeling Techniques in Service Quality Evaluation of Surface Transportation during the Last Decade  
*Nayeem Islam* 197
06. The Periodicity of the Accuracy of Numerical Integration Methods for the Solution of Different Engineering Problems  
*Toukir Ahmed Chowdhury, Towhedul Islam, Ahmad Abdullah Mujahid, Md. Bayazid Ahmed* 203
07. Volume Charge Density in Geometric Product Lorentz Transformation  
*Md. Ashrafal Alam, Atikur Rahman Baizid* 217
08. Predicting Retinal Diseases using Efficient Image Processing and Convolutional Neural Network (CNN)  
*Asif Mohammad, Mahruf Zaman Utso, Shifat Bin Habib, Amit Kumar Das* 221

This page is intentionally left blank.

# Journal of Engineering Advancements

Editor-in-Chief

Prof. Dr. Mohammad Mashud  
Department of Mechanical Engineering,  
Khulna University of Engineering & Technology, Khulna, Bangladesh

Executive Editors

Dr. Md. Shariful Islam  
Department of Mechanical Engineering,  
Khulna University of Engineering & Technology, Khulna, Bangladesh

&

Dr. Md. Arifuzzaman  
Department of Mechanical Engineering,  
Khulna University of Engineering & Technology, Khulna, Bangladesh



**Published by: SciEn Publishing Group**

Apt. # 6 C-D, House # 191, Road # 9/A  
Dhanmondi, Dhaka-1209, Bangladesh  
Email Address: [jea@scienpg.com](mailto:jea@scienpg.com)

[www.scienpg.com/jea/](http://www.scienpg.com/jea/)

This page is left intentionally blank

# Numerical and Experimental Study on Optimization of Coil Springs used in Vehicles' Suspension System

*Mostafizur Rahman\**, *Saeem Bin Abdullah*

Department of Mechanical Engineering, Chittagong University of Engineering and Technology,  
Chattogram-4349, Bangladesh.

Received: July 28, 2021, Revised: September 24, 2021, Accepted: September 30, 2021, Available Online: October 03, 2021

## ABSTRACT

In general, the suspension systems are used to absorb vibrations, bump, rolls, dip from shock loads due to road surface irregularities. It performs its major role without affecting the vehicles' stability and overall handling during operation. Coil springs are used as suspension element in light vehicles to attenuate unwanted vibrations. A spring is an elastic object used to store mechanical energy and it can be twisted, pulled or extended by some force and can return to its initial position when the force is released. In this study, mild steel material was taken into consideration in designing and fabricating coil springs. Theoretical and experimental investigations were conducted to calculate springs' stiffness and to make validation between them. Three model of springs having coils 10, 11, 14 respectively are designed which have slight stiffness difference both theoretically and experimentally. The models were analyzed to determine mechanical behaviors for randomly chosen loading conditions ranging from 29.4 N to 176.4 N which are better suited with spring size. It is noted from both numerical and experimental investigations that deflection is high when the stiffness is less and vice-versa. In addition, shear stress formation increases with the increment of stiffness and applied load. Hence, springs having high stiffness are used in suspension system to reduce vibration and other disturbances. This study shows springs of having high stiffness are comparatively compact in size and cost economic as well.

Keywords: Suspension system, Coil spring, Stiffness, Deflection, Stress formation.



This work is licensed under a [Creative Commons Attribution-Non Commercial 4.0 International License](https://creativecommons.org/licenses/by-nc/4.0/).

## 1 Introduction

Automobile engineering known as automotive engineering deals with design, development, manufacturing, and safety testing field of vehicles. Automotive engineering, aerospace engineering, and naval architecture are branch of vehicle engineering that incorporates mechanical, electrical, and control engineering elements applied to the design, manufacturing, and operation of vehicles. Automotive manufacturing needs a big team of experts specializing in particular elements. These specializations include aerodynamics, mechanics of machineries, control systems, and control of emissions [1]. In addition, it involves improved modification on suspension system as well. Suspension systems are used to carry load, maintain a good contact between road and wheel, to improve handling as well as ride quality, which are sometimes at conflict [2]. Suspension mechanism connects a vehicle to its wheels and allows relative motion between them. It includes tires, springs, shock absorbers, and linkages. Furthermore, three main elements, which are used in suspension system of vehicles, are the wishbones, springs, and mostly the shock absorber [3]. These elements are used not to transmit the exerted forces from the road surface in the vehicle body. The first workable spring suspension required extensive metallurgical knowledge and ability, and it was only conceivable with the onset of industrialization that it became possible [4]. The above mentioned suspension elements are very sophisticated parts in engineering applications. Hence, proper investigations are needed to conduct by both numerically and experimentally to get concrete results before using them in engineering applications. Springs namely coil, compression, tension, torsional, leaf, and many more springs are used in suspension system. Coil springs are widely used in light vehicles'

suspension system due to its outstanding mechanical properties and easy manufacturing. A variety of mechanical behaviors, reliability, and life cycles are needed to study considering real operating conditions before using them in automobile because replacing, maintenance would take time and matter of cost as well if failure is occurred often and then. That's why Das et al. [5] investigated failure analysis of helix shaped man-made coil springs used in passenger car. Authors modified coil diameter, spring mean diameter, free length, and amount of coil turns per unit length to make the optimal design. They showed that springs normally fail owing to elevated cycle fatigue where the stress applied is below the point of yield strength and the charging cycle is more than  $10^5$  cycles /sec. In addition, premature failure of coil spring's suspension was investigated and it was failed after some months putting into services. However, Vukelic et al. [6] studied failure analysis of coil springs used in motor vehicle suspension system for different static and cyclic loading condition. Furthermore, Nohut et al. [7] analyzed failure probability of ceramic coil springs. Ceramic springs are accessible commercially and a thorough assessment of reliability of these parts, would be helpful for their implementation in advanced engineering applications. In Contrast, Pastorcic et al. [8] conducted failure and fatigue analysis of coil springs used in light vehicles. The failed coil springs were examined to determine the causes of fracture using experimental procedures such as, visual observations, optical, and scanning electron microscopy. Furthermore, Assaad Alsahlani et al. [9] investigated design and failure of coil springs in vehicles using finite elements method. Suspension system in vehicle plays a very significant role to absorb and dissipate energy so that the suspension systems can offer the passengers comfortness, safety riding, and mechanical stability as well. Authors performed

spring simulation using Solid Works 2018 with particular measurements and analyzed it with ANSYS 14 finite element analyzer. Researches are needed to carry out on spring materials to find out best one which shows outstanding mechanical properties operating by various conditions. Logavigneshwaran et al. [10] investigated design, fabrication, and analysis of helical coil springs made of alloy steel used in suspension systems so that it could withstand the deformation occurred in springs. Authors also demonstrated the application of composite materials to fabricate helical coil springs. In addition, Tausif M. Mulla et al. [11] researched the stress analysis of helical coil compression springs made of ASTM A227 used in Indian automotive market's three-wheeler auto-rickshaw. Quasi-static approach to the assessment of finite elements in the time domain was used to predict the fatigue life of the helical compression coil springs. Model of Morrow and model of Smith-Watson Topper were used under variable amplitude charging for fatigue life calculations for the springs. It is noted that, Sreenivasan et al. [12] investigated use of different fibre materials to fabricate springs used in suspension systems and assessed their performance. Autodesk inventor was used to design a suspension system and ansys 16.0 software was used to perform Finite element analysis (FEA). Comparative structural analysis was carried out using different loads in relation to the motorcycle's payload to calculate the overall deformation, stress, and strain of the suspension in static conditions. In contrast, Sathish et al. [13] investigated the optimal methods to design and production of coil spring using lathe centre. The tumbler gear mechanism is used to form a coil spring on lathe machine which is powered by a simple electric motor having variable operating speeds. To the authors of best knowledge, springs made of various materials used in suspension systems are needed to design and fabricate robustly to improve reliability, performances, and life cycles considering real operating conditions. Deep numerical and experimental studies are needed to conduct to access their properties. This study focuses on optimization on coil springs used suspension systems by both numerically and experimentally.

## 2 Methodology and Design

### 2.1 Methodology

Fig. 1 shows the total procedures followed in this study as analyzing the dimensions of springs, designing three springs using solidWORKS, fabricating three springs using required material in workshop, evaluation of properties and optimization of the designs by different tests, and analyzing results and recommendation for use.

### 2.2 Design

Three model of springs having stiffness of 2000 N/m, 2500 N/m, and 3000 N/m are designed using solidWORKS and their parameters are chosen accordingly. Fig. 2 shows a model of coil spring used in suspension system [14], where  $D$ =spring coil mean diameter (mm),  $D_o$ =spring coil's outside diameter (mm),  $D_i$ = spring coil's inside diameter (mm),  $d$ =spring wire's diameter,  $N$ = active coils number,  $N_t$ =number of total coil,  $G$ =modulus of rigidity of the spring materials,  $F$ =spring's axial load,  $C$ =spring index,  $P$ =pitch (mm),  $L$ = spring's free length (mm),  $K$ = Wahl factor,  $k$ =spring stiffness.

Fig. 3 represents the designed three model of springs varying their parameters. Fig. 3 (a) shows a typical coil spring model and spring model 1, spring model 2, spring model 3, and fabricated

spring are shown in Fig. 3 (b), Fig. 3 (c), Fig. 3 (d), and Fig. 3 (e) respectively.

shows the specifications of the designed and fabricated springs. It is worthy to mention that three models are designed and fabricated just varying number of coils and other parameters keeping unchanged. It is noted that spring model 2 is more stiffened than spring model 1 and spring model 3 is more stiffened than both.

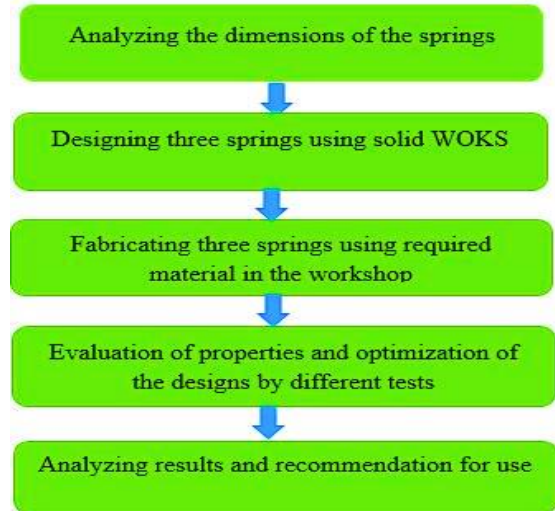


Fig. 1 Flow diagram of research work

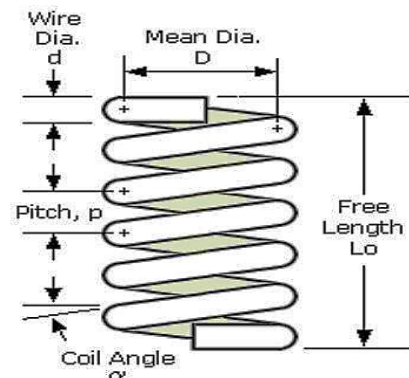


Fig. 2 Terminology used in spring design (Design adapted from [14])

Equation (1) is used to calculate spring stiffness theoretically, where  $G$  is the modulus of rigidity of spring material. Spring deflections and actual stiffness of springs are determined using Eq. (2), where  $\delta$  is the deflection of spring end from its equilibrium position. Equation (3) is used to calculate shear stress developed in the springs for various loading.

Spring stiffness,

$$k = \frac{G \times d^4}{8 \times D^3 \times N} \text{ N/mm} \quad (1)$$

Spring deflection,

$$\eta = \frac{J}{2\pi} \cdot \frac{K_T}{K_Q} \quad (2)$$

Shear stress,

$$\eta = \frac{J}{2\pi} \cdot \frac{K_T}{K_Q} \quad (3)$$

Table 1 Specifications of the springs

SI. No.	Name	Wire dia. (d), mm	Mean coil dia. (D), mm	No. of coil (N)	Free length, mm	Stiffness (k), N/m
01	Model 1	4	45	14	165.10	2000
02	Model 2	4	45	11	165.10	2500
03	Model 3	4	45	10	165.10	3000

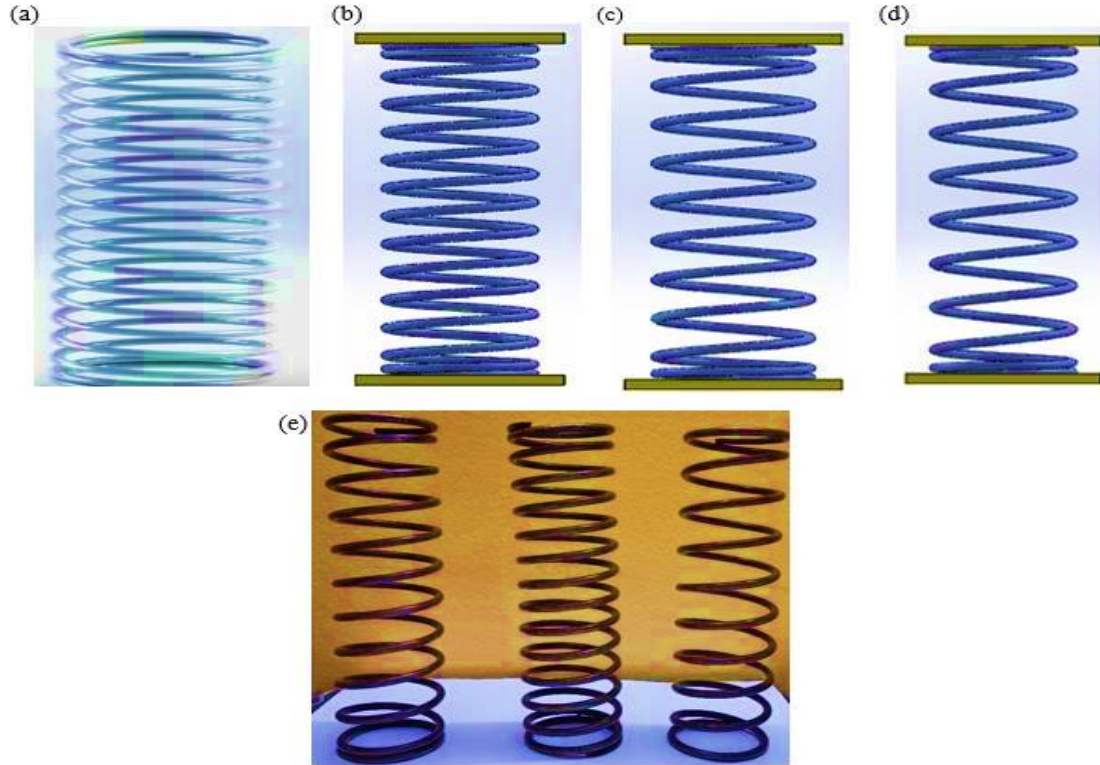


Fig. 3 Graphical representation of (a) a typical spring design (b) spring model 1 (c) spring model 2 (d) spring model 3 (e) fabricated springs

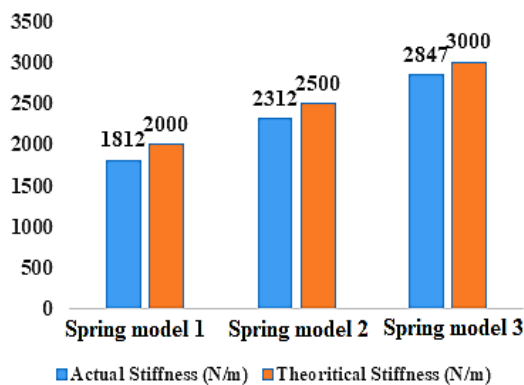


Fig. 4 Variation between actual and theoretical stiffness of designed springs

However, small amount of alloying elements in mild steel makes it comparatively inexpensive when compared to other steels [15]. The price, weldability, and machinability of this mild steel make it a popular customer choice. Spring assembly machine is used to manufacture those springs. In addition, spring stiffness and spring deflections are measured using Camry spring tester machine. A variety of deflections are taken for different applied load. Load values and deflections are taken from display. Theoretical and actual stiffness of the models are calculated and a little bit variation is observed as shown in Fig. 4 due to

fabrication errors. Deformation variation and stress formation variation are observed due to this stiffness difference which is discussed later.

### 3 Results and Discussion

Three model of designed springs are simulated using various conditions to understand their mechanical behaviors that are helpful to predict fatigue failure, reliability, and life cycles. Static structure analysis was performed taking boundary conditions of springs fixed both end on a flat plate. Exact chemical and mechanical properties of mild steel are taken into account for simulating. Low stiffness spring element constraint method is used to give different loads on spring ends. Applied loading values ranging from 29.4 N to 176.4 N are chosen randomly and used in the both simulation and experimental process. Loading values and other conditions could be varied in real operating cases. However, those results would be useful to reach in concrete decision in designing coil springs used in suspension system. Fig. 5 shows deflection variation of springs for 29.4 N. It is noticed that 16.022 mm deflection has been observed for spring model 1 whereas, 12.511 mm deflection for spring model 2, and 11.158 mm deflection for spring model 3. Equation (2) termed as ‘deflection measurement of springs’ signifies that spring deflection decreases with decrease of turns [16]. Springs are designed considering operating conditions so that good performances can be obtained.

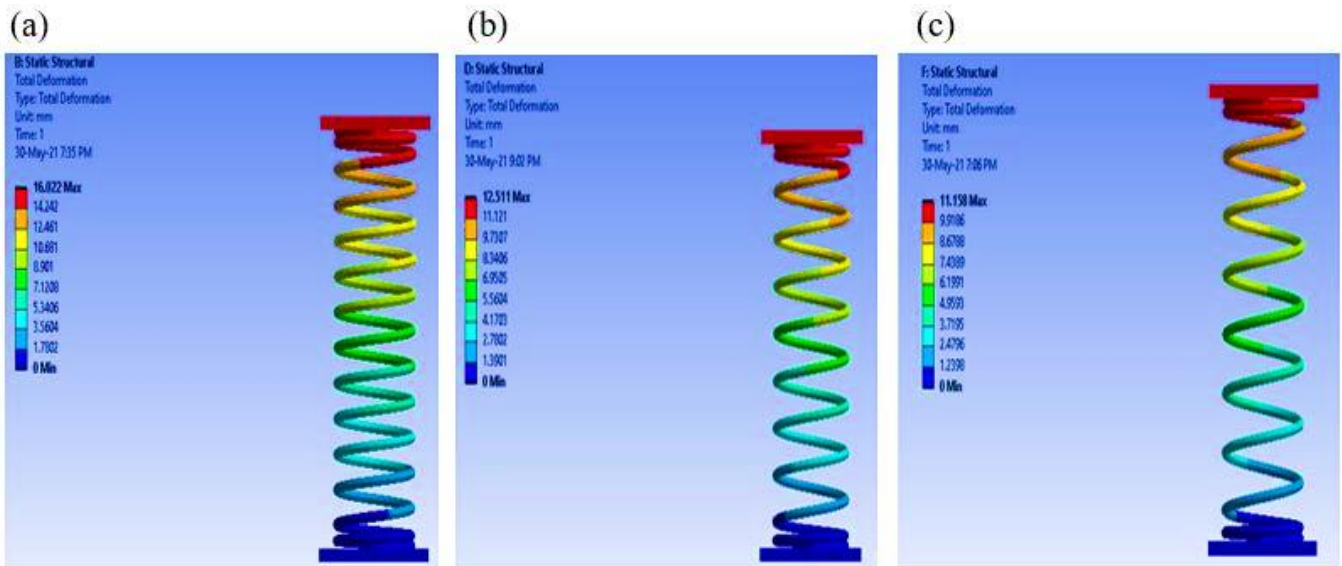


Fig. 5 Variation of deflection for 29.4 N load on (a) spring model 1 (b) spring model 2 (c) spring model 3

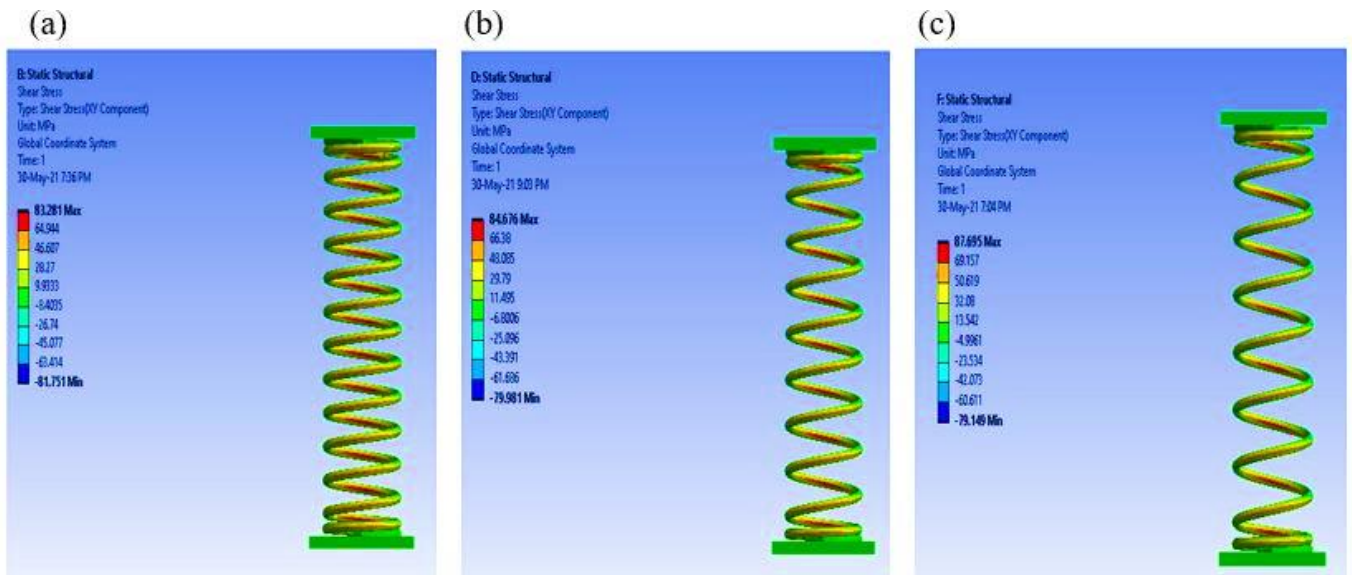


Fig. 6 Variation of shear stress for 29.4 N load on (a) spring model 1 (b) spring model 2 (c) spring model 3

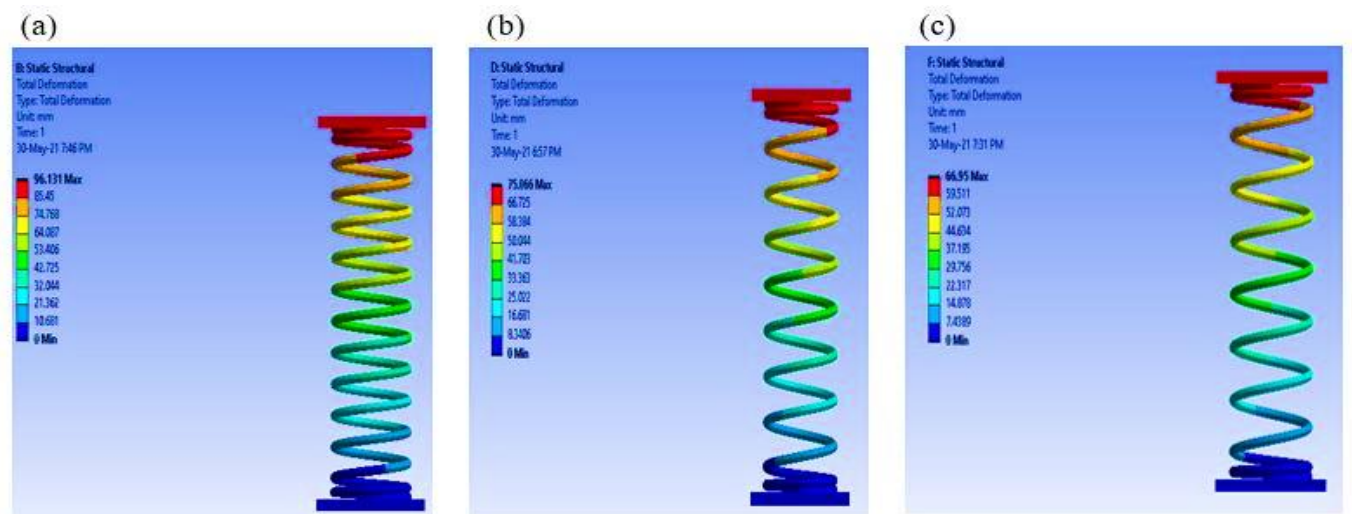


Fig. 7 Variation of deflection for 176.4 N load on (a) spring model 1 (b) spring model 2 (c) spring model 3

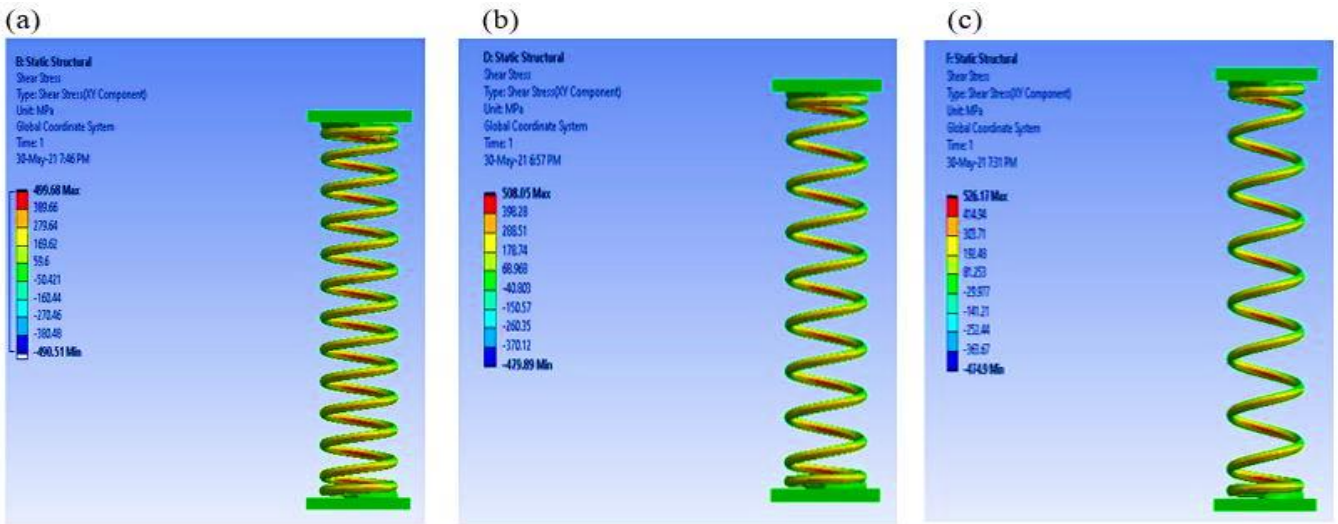


Fig. 8 Variation of shear stress for 176.4 N load on (a) spring model 1 (b) spring model 2 (c) spring model 3

It is known to all that stress is formed on mechanical parts subjected to static, dynamic, and cyclic loading conditions [17]. Parts are designed as they can withstand those stressed conditions to provide satisfactory performances. Stress variation on three designed springs having different turns are shown in Fig. 6. Maximum 87.695 MPa stress has been found to form on spring model 3, whereas, 83.281 MPa stress on spring model 1 and 84.676 MPa on spring model 2.

were also simulated for loading values 58.8 N, 88.2 N, 117.6 N, and 147 N to make a comparison of their behaviors as shown in Fig. 10, Fig. 11 and Fig. 12.

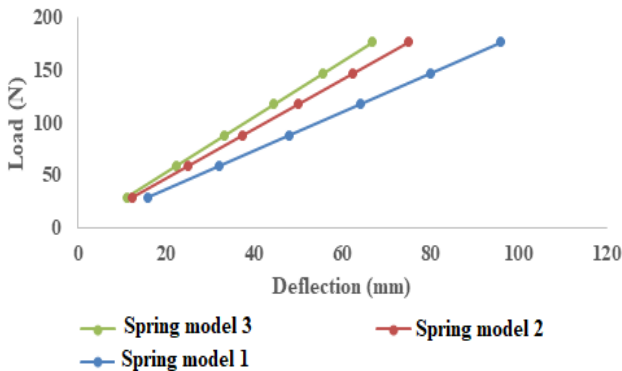


Fig. 9 Variation of theoretical deflection for loads on designed springs

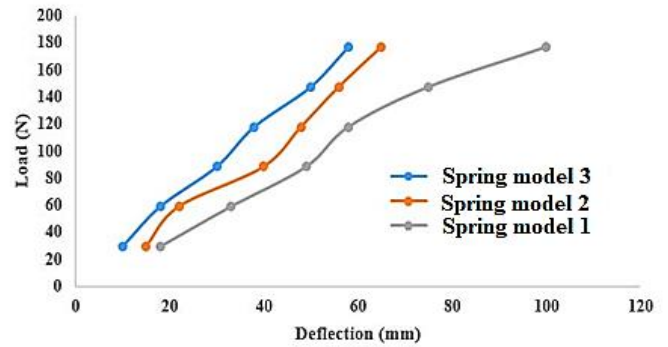


Fig. 11 Variation of experimental deflection for loads on designed springs

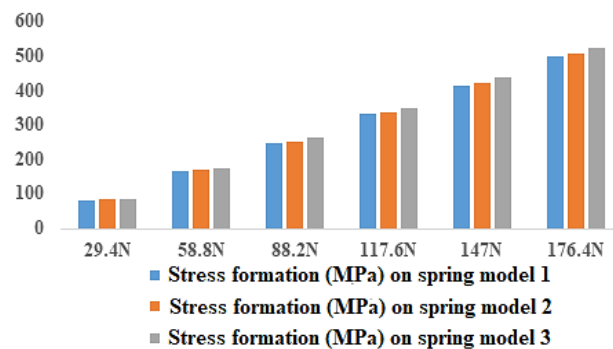


Fig. 10 Variation of theoretical shear stress for loads on designed springs

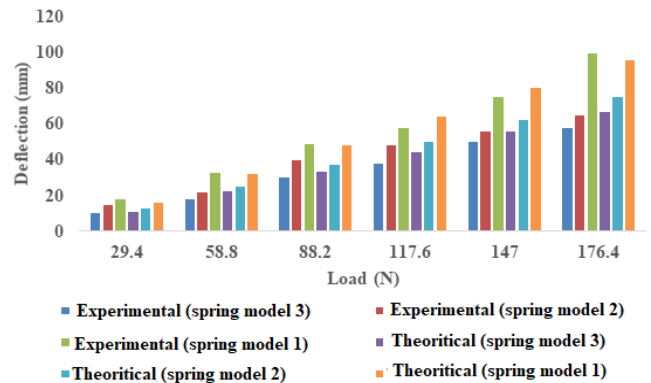


Fig. 12 Variation of actual and experimental deflection for loads on designed springs

Furthermore, it is noticed that 96.131 mm deflection has been observed for spring model 1, 75.066 mm for spring model 2, and 66.95 mm for spring model 3 due to 176.4 N load as shown in Fig. 7. In addition, maximum 526.17 MPa stress has been found to form on spring model 3, 508.08 Mpa for model spring 2, and 499.68MPa for spring model 1. Moreover, those springs

According to spring force Eq. (2), deflection is increased with the increase of spring force [16]. Fig. 9 represents the proportional increase of deflection with the change of Load. The horizontal axis represents deflection in mm and the vertical axis represents the load in Newton. It is noted spring model 1 shows maximum deflection and spring model 3 shows minimum deflection for a specific load. Hence, it is concluded that springs are designed as per requirements to fulfill static loading conditions. Equations (1) - (2) which represent that spring deflection decreases with the decrease of turns. Decreasing

spring turns keeping other parameters unchanged increases spring stiffness. Spring deflection decreases with increase of stiffness for a specific load as from Eq. (2). Lowering number of spring turns and keeping all parameters unchanged are making springs optimized in sense of size, weight, and cost also. This is main theme of this study to optimize coil springs used in vehicles' suspension system. In addition, Fig. 10 represents the variation of shear stress developed on each design for every specific load. It is noticed that the shear stress is increasing with the increase of applied load. Shear stress formation increases with the increase of stiffness and spring model 3 validates this. Shear stress is maximum on spring model 3 for every specific load whereas, shear stress developed on spring model 2 is less than spring model 3 but more than spring model 1 for every specific load.

It is known to all that experimental results do not validate 100% accurately the aforementioned theories due to some human, technical, and methodological errors. Fig. 11 represents experimental deflection of springs with the increase of load. Loads have been applied on the three designed springs using a spring tester having a digital display. It is clearly noticeable that the deflection is increasing but it is not proportional like the theoretical deflection as shown before. For every specific load, spring model 3 shows comparatively less deflection than spring model 2 and spring model 1. A slight deflection difference is observed between spring model 2 and spring model 1. On the contrary, noticeable deflection difference is observed in case of spring model 1.

Fig. 12 shows a detailed comparative representation between theoretical and experimental deflection of designed springs for six loads. A little bit difference has been observed between theoretical and experimental results for every specific load on each design due to slight stiffness difference.

#### 4 Conclusion

This study represents design, fabrication, analysis, and size optimization of coil springs used in vehicles' suspension system. Springs are designed varying number of turns and keeping other parameters unchanged. Mild steel was used to fabricate those springs due to its low cost and easy availability. Stiffness was calculated theoretically and experimentally before performing simulation and experimental investigations. A slight stiffness difference was observed due to impurities in materials, human, technical, and methodological errors throughout the process. It is concluded that spring having 10 number of turns showed less deflection compared to others and more shear stress developed as well. Spring designers would design springs as per requirements during service conditions considering reliability and life cycles. Optimization of size, weight, and shape of springs would make the cost economic and have effects on reliability and life cycles. Some drawback of this study exists. A comparative study could be done using various materials to find out the best results. Analysis of fatigue failure due to cyclic loading would add a significant dimension in this research field.

#### Acknowledgments

Authors would like to express their gratefulness to Department of Mechanical Engineering, Chittagong University of Engineering and Technology, Chattogram-4349, Bangladesh for providing financial and experimental facility to do this research work.

#### References

- [1] Shala, A., Hajrizi, E. and Likaj, R., 2010. Modelling and Simulation of road Vehicle. IFAC Proceedings Volumes, 43(25), pp.65-68.
- [2] Putra, T.E. and Machmud, M.N., 2020. Predicting the fatigue life of an automotive coil spring considering road surface roughness. Engineering Failure Analysis, 116, p.104722.
- [3] Tsubouchi, T., Takahashi, K. and Kuboki, T., 2014. Development of coiled springs with high rectangular ratio in cross-section. Procedia Engineering, 81, pp.574-579.
- [4] Mitra, A.C., Soni, T. and Kiranchand, G.R., 2016. Optimization of automotive suspension system by design of experiments: a nonderivative method. Advances in Acoustics and Vibration, 2016.
- [5] Das, S.K., Mukhopadhyay, N.K., Kumar, B.R. and Bhattacharya, D.K., 2007. Failure analysis of a passenger car coil spring. Engineering failure analysis, 14(1), pp.158-163.
- [6] Vukelic, G. and Brcic, M., 2016. Failure analysis of a motor vehicle coil spring. Procedia Structural Integrity, 2, pp.2944-2950.
- [7] Nohut, S. and Schneider, G.A., 2009. Failure probability of ceramic coil springs. Journal of the European Ceramic Society, 29(6), pp.1013-1019.
- [8] Pastorcic, D., Vukelic, G. and Bozic, Z., 2019. Coil spring failure and fatigue analysis. Engineering Failure Analysis, 99, pp.310-318.
- [9] Al Sahlani, A., Khashan, M.K. and KHALEEL, H.H., 2018. Design and analysis of coil spring in vehicles using finite elements method. Int. J. Mech. Product. Eng. Res. Dev, 8(4), pp.615-624.
- [10] Logavigneshwaran, S., Sriram, G. and Arunprakash, R., 2015. Design and Analysis of Helical Coil Spring in Suspension System. International journal for trends in engineering & technology, 9(1), pp. 1-5.
- [11] Mulla, T.M., 2016. Fatigue life estimation of helical coil compression spring used in front suspension of a three wheeler vehicle. Proceedings of the modern era research in mechanical engineering-2016 (MERME-16), Urun Islampur, India, 29.
- [12] Sreenivasan, M., Kumar, M.D., Krishna, R., Mohanraj, T., Suresh, G., Kumar, D.H. and Charan, A.S., 2020. Finite element analysis of coil spring of a motorcycle suspension system using different fibre materials. Materials Today: Proceedings, 33, pp.275-279.
- [13] Sathish, T., Sabarirajan, N., Chandramohan, D. and Karthick, S., 2020. A novel technique to design and production of coil spring in centre lathe. Materials Today: Proceedings, 33, pp.2521-2523.
- [14] Abidin, M.I.Z., Mahmud, J., Abd Latif, M.J. and Jumahat, A., 2013. Experimental and numerical investigation of SUP12 steel coil spring. Procedia Engineering, 68, pp.251-257.
- [15] Ekanthappa, J., Shankar, G.S., Amith, B.M. and Gagan, M., 2016, September. Fabrication and experimentation of FRP helical spring. In IOP Conference Series: Materials Science and Engineering (Vol. 149, No. 1, p. 012098). IOP Publishing.
- [16] Pawar, H.B. and Desale, D.D., 2018. Optimization of three wheeler front suspension coil spring. Procedia manufacturing, 20, pp.428-433.
- [17] Kim, K.T., 2010. A study on mechanical properties and flow-induced vibrations of coil-shaped holddown spring. Nuclear engineering and design, 240(4), pp.747-755.

# Investigation of Mechanical Properties of Banana-Glass Fiber Reinforced Hybrid Composites

*Kazi Jubair, Md. Shariful Islam\* and Dipto Chakraborty*

Department of Mechanical Engineering, Khulna University of Engineering and Technology, Khulna-9203, Bangladesh.

Received: February 24, 2021, Revised: October 23, 2021, Accepted: October 31, 2021, Available Online: November 09, 2021

## ABSTRACT

Banana stems are very cheap and abundant in nature which can be used to extract fiber. In this paper, banana fiber is used as a reinforcement and epoxy as a matrix to manufacture banana fiber-reinforced epoxy composite. Glass fiber mat, and roving are also used as reinforcement along with banana fiber to manufacture hybrid composites. The objective of this paper is to compare the mechanical properties of hybrid composites with that of pure banana fiber-reinforced composites. The hand lay-up method is used to manufacture all the composites, and tensile and flexural properties are investigated according to the corresponding ASTM standard. It is found that the tensile and flexural strength of banana and glass fiber roving hybrid composites are much higher compared to pure banana fiber-reinforced epoxy composites which make this hybrid composite suitable for low strength application.

Keywords: Banana Fiber; Hybrid Composite; Tensile Strength; Flexural Strength.



This work is licensed under a [Creative Commons Attribution-Non Commercial 4.0 International License](https://creativecommons.org/licenses/by-nc/4.0/).

## 1 Introduction

The typical composite material consists of reinforcement and matrix phase where the constituent materials are distinguishable by observing their appearance. It is very popular in the aerospace and automobile industries because of its higher strength to weight ratio [1]. Based on the type of reinforcement, it is classified as natural fiber and synthetic fiber composite. Natural fiber composite includes jute, flax, bamboo, banana, kenaf fiber, etc., which are directly extracted from natural sources. Synthetic fiber includes glass, carbon, Kevlar fiber, etc. If more than one type of fiber is used for reinforcement, then the composite is known as a hybrid composite. In this paper, both natural and synthetic fiber-reinforced composite is studied along with their hybrid composite.

Hybrid composites with more than one reinforcing material shows preferable mechanical properties because the mechanical properties can be tailored according to specific needs. Natural fiber and its hybrid composites could be used as a replacement of wood in shelves, partitions, tabletop, and it can also be used as interior parts in automobile industries, and as construction materials such as walls and roofs, packaging industries, fishing boats etc. [2], [3] and [4]. Munoz et al. studied mechanical properties of flax fiber-reinforced bio-epoxy composites for various fiber volume fractions and found that swelled flax fiber composites showed preferable mechanical properties over the dried one [5]. Islam et al. studied the mechanical properties of banana and rattan fiber reinforced epoxy composite and reported that the tensile strength of the banana fiber is higher compared to rattan fiber [6]. Maleque et al. investigated the mechanical properties of woven banana fiber reinforced composites with epoxy as a matrix [7]. Pothan et al. found the optimum fiber volume fraction is 40 % while investigating the mechanical properties of banana fiber reinforced polyester composite [8]. An investigation on banana fiber reinforced green composite carried out by Sharma et al. reveals that the mechanical properties are better at 15 wt% fiber reinforcement [9]. The effect of fiber length and volume fraction is studied by Venkateshwaran et al.

where they have found 15 mm fiber length and 16% fiber volume fraction give optimum properties [10]. Joseph et al. studied the mechanical properties of banana and glass fiber reinforced hybrid composite and reported that hybrid composite with better mechanical properties can be manufactured using banana and glass fiber as reinforcements which leads to this investigation [11].

In this paper, the mechanical properties of banana, glass fiber roving, glass fiber mat, and hybrid banana/glass fiber (both mat and roving) are extensively studied. Since the strength of the glass fiber mat and roving is higher compared to banana fiber, it is expected that the hybrid composite would give better strength compared to pure banana fiber-reinforced composite. This paper compares the mechanical properties of banana/glass fiber mat and banana/glass fiber roving composites with that of pure banana fiber-reinforced composites. The following sections describe the composite manufacturing process, mechanical testing, results and discussions followed by the conclusion.

## 2 Materials and Methods

### 2.1 Materials

Banana, E-glass fiber mat, and roving are used as reinforcements, and LY 556 epoxy with HY 951 hardener is used for matrix material in this investigation. Banana stem is purchased from the local market, and this banana stem is used to extract the fiber, as discussed in the following section.

### 2.2 Fiber Extraction

The stem is the part of the banana plant that looks like a trunk that is used for fiber extraction. This part of the plant was squeezed out about 60% of the water and lignin. After that, it was left 10 to 15 days within rotten water. After 15 days, the lignin of the banana stem is completely dissolved in the water and then the fiber is washed with clean water. The extracted fiber is then dried in the open air at room temperature. Fig. 1 shows the different steps involved in the fiber extraction process.

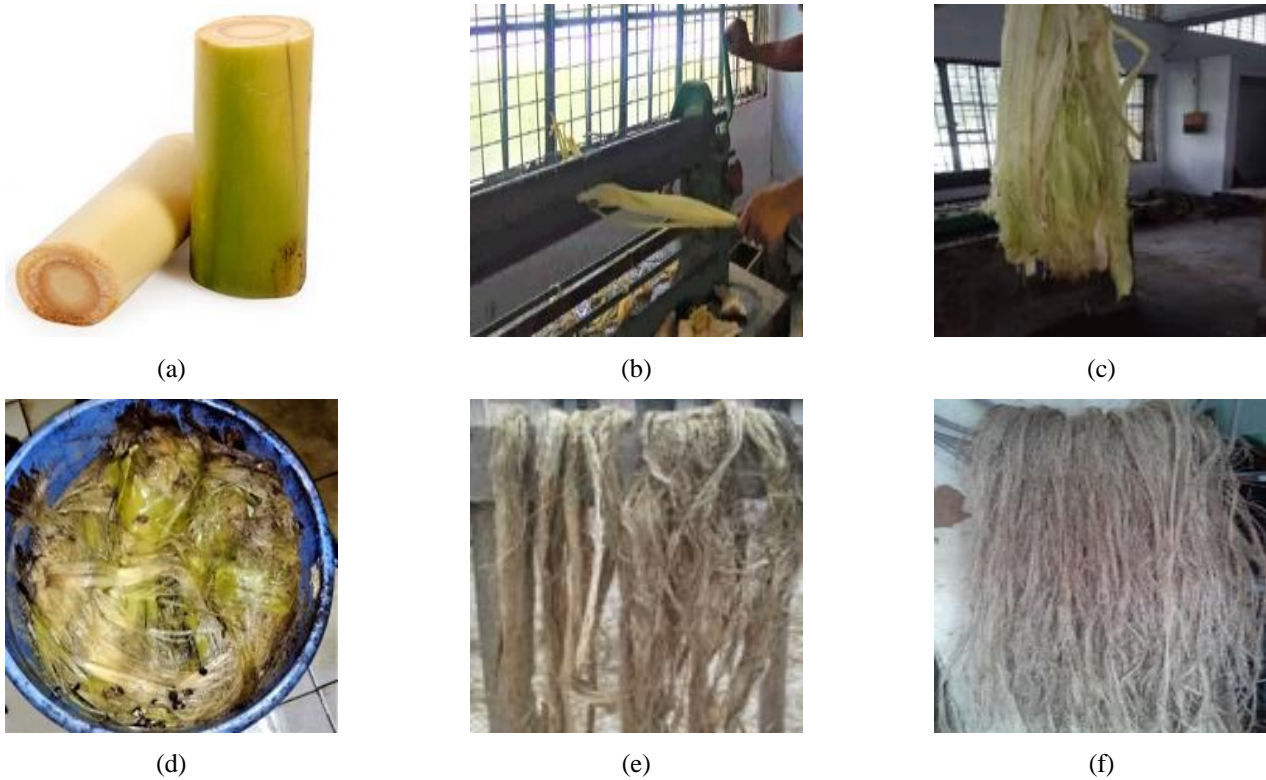


Fig. 1 Extraction of banana fiber (a) banana stem, (b) manual rolling of the stem, (c) rolled stem, (d) stem in rotten water, (e) drying of extracted fiber, and (f) extracted fiber.

### 2.3 Composite Fabrication

The hand lay-up technique is used to manufacture the composites, which is a popular and effective way [12], [13]. Fig. 2 shows [14] the typical hand lay-up molding process. The mold release agent is applied over the top and bottom mold plate at the beginning, and then epoxy and hardener mixture is applied on the bottom mold plate with the help of a brush. A roller is then used to evenly distribute the epoxy. The first layer of the reinforcing materials is then placed on top of that and again epoxy is poured and rolled over the layer. This process is repeated until the final layer of the reinforcing material. Once all the reinforcing layer is stacked, then the top mold plate is placed and a pressure of 100 MPa is applied on top of the mold plate. The set-up is kept like this way for 24 hours at room temperature to allow the matrix to cure. After 24 hours, the manufactured composite is demolded and cut into small pieces according to the corresponding ASTM standard for mechanical testing. Fig. 3 shows the manufactured composite.



Fig. 3 Manufactured composite.

#### Hand Lay-Up

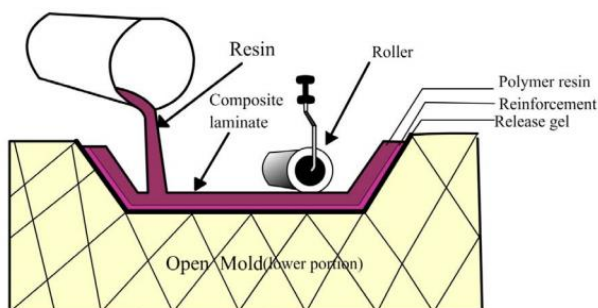


Fig. 2 Schematic diagram of hand lay-up process [14].

### 2.4 Tensile Test

Tensile tests on four types (banana, glass, hybrid 1, and hybrid 2) manufactured composites are performed according to ASTM D3039 standard [15]. Hybrid 1 consists of two layers of banana fiber and two layers of glass fiber mat while hybrid 2 consists of two layers of banana fiber along with two layers of glass fiber roving. For hybrid composites, the glass fiber (mat/roving) layers are used as the top and bottom layers since these layers experience maximum stress compared to the inner two layers. Specimens are cut along parallel to the fiber direction, and 5 specimens are tested for each type of composite. Fig. 4 shows the tensile test specimen with dimension, the average thickness of the specimens is 6 mm. Tensile specimens are

loaded on a SHIMADZU (AGX-300KNV) universal testing machine while the loading rate is 2 mm/min and tested until the specimens fail. Equation 1 is used to calculate the ultimate tensile strength according to the ASTM D3039 standard [15].

$$F^{tu} = P^{max} / A \tag{1}$$

Where,  $F^{tu}$  is ultimate tensile strength, MPa  
 $P^{max}$  is the maximum force before failure, N  
 $A$  is the cross-sectional area, mm<sup>2</sup>.

Tensile chord modulus of elasticity is calculated according to equation 2, and for this calculation, the absolute tensile strain of 0.001 to 0.003 is used as suggested by ASTM D3039 standard [15].

$$E^{chord} = \Delta\sigma / \Delta\varepsilon \tag{2}$$

Where,  $E^{chord}$  is the tensile chord modulus of elasticity, GPa,

$\Delta\sigma$  is the difference in applied tensile stress between the two strain points (0.001 and 0.003), MPa  $\Delta\varepsilon$  is the difference between two strains (0.002).

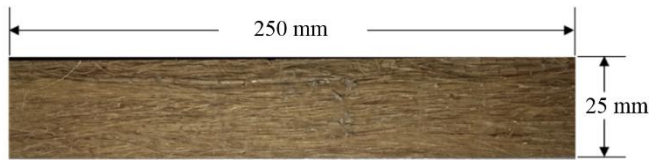


Fig. 4 Tensile test specimen with dimension.

2.5 Flexural Test

The flexural properties of the manufactured composites are determined by performing three-point bending tests. The test specimens are cut and tested according to ASTM D 7264 [16] with a span-to-thickness ratio of 32:1. Five specimens of each type are tested in the same SHIMADZU (AGX-300KNV) universal testing machine, and the loading rate of 1.0 mm/min is maintained. All the specimens are tested until failure. Fig. 5 shows the three-point bending test specimen with dimension.

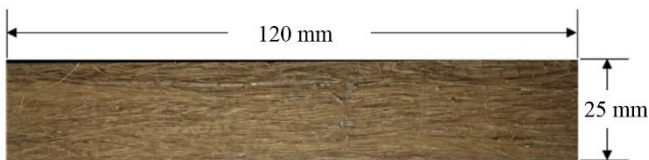


Fig. 5 Three-point bend test specimen with dimension.

The flexural strength of the specimens is calculated using the following equation from ASTM D 7264 [16].

$$\sigma = \frac{3PL}{2bh^2} \tag{3}$$

Where,  $\sigma$  is the flexural strength, MPa  
 $P$  is the maximum applied force, N  
 $L$  is the support span, mm  
 $b$  is the specimen width, mm  
 $h$  is the thickness of the specimen, mm.

Flexural chord modulus of elasticity is calculated by following ASTM D 7264 [16] standard with a similar equation of (2).

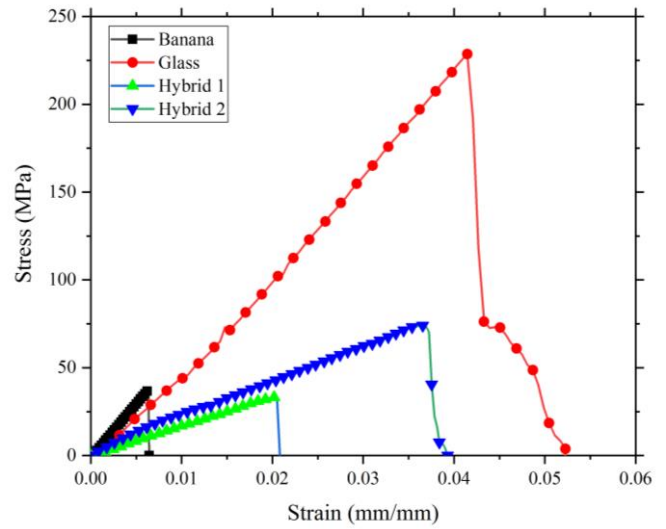
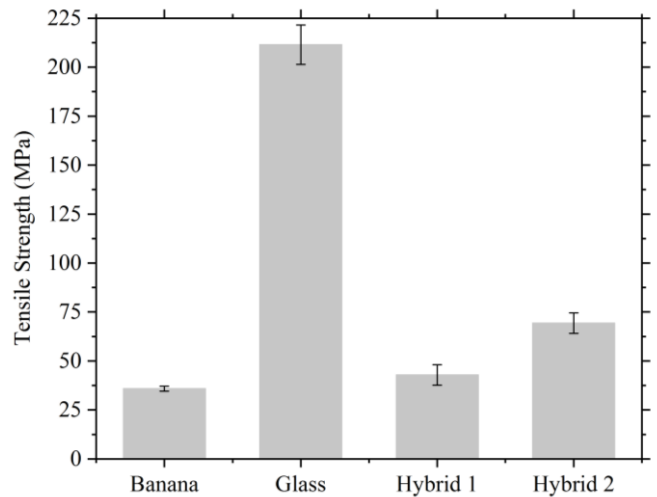
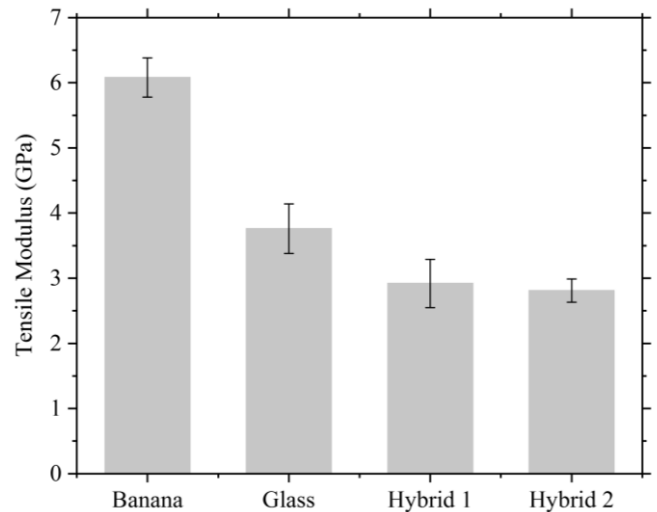


Fig. 6 Stress-strain diagram for the tensile test.



(a)



(b)

Fig. 7 Tensile test results (a) Strength and (b) Modulus.

### 3 Results & Discussion

#### 3.1 Tensile test

The typical stress-strain diagram for all four types of composites is shown in Fig. 6. It is observed from this figure, that the maximum stress is minimum for banana fiber composite and maximum for glass fiber composite. The maximum stresses of hybrid 1 and hybrid 2 are between the banana and glass fiber composite which can be also found in Fig. 7 (a). The slope of the stress-strain diagram for banana fiber composite is maximum which indicates that the tensile modulus (refer to Fig. 7 (b)) is maximum for banana fiber composite.

The tensile strength of different composites is shown in Fig. 7 (a) and the tensile modulus is shown in Fig. 7 (b). From Fig. 7 (a), it is found that the tensile strength of the banana fiber is minimum and that of glass fiber is maximum, while for hybrid composite, the tensile strength is in between banana and glass fiber composites. The average tensile strength of banana fiber composite is 35.86 MPa, for hybrid 1 is 42.83 MPa and for hybrid 2 is 69.28 MPa. This indicates 19.44 % and 93.20 % increase in tensile strength for hybrid 1 and hybrid 2 respectively compared to banana fiber composite.

The tensile modulus of the Banana fiber composite is higher compared to the other three composites as shown in Fig. 7 (b). For hybrid 1 and 2, 51.97 % and 53.78 % lower flexural modulus is found compared to Banana fiber composites. One reason could be the lay-up because two glass fiber layers were placed in between two Banana fiber layers.

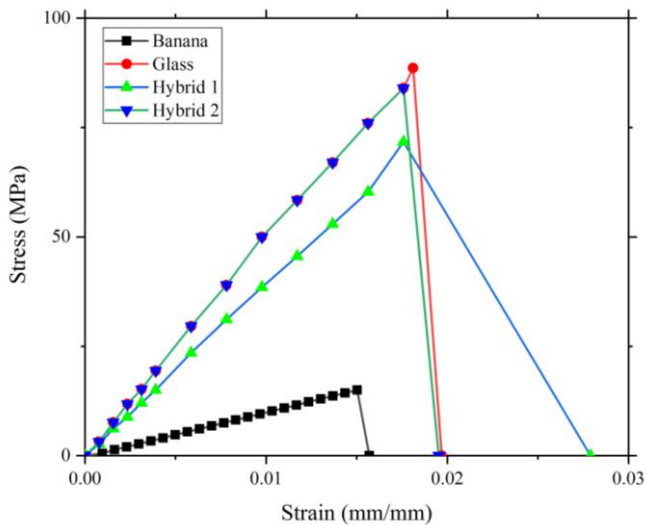


Fig. 8 Stress-strain diagram for the flexural test.

#### 3.2 Flexural Test

The typical stress-strain diagram for all four types of composites is shown in Fig. 8. It is observed from this figure that the maximum stress for banana fiber is minimum compared to other composites which indicates that flexural strength for banana fiber composite is lower than the other composites. Flexural modulus is calculated for these composites using this stress-strain diagram and shown in Fig. 9 (b).

Fig. 9 shows flexural strength and flexural modulus of different composites. It is perceived from Fig. 9 that the flexural strength of Banana fiber composite is minimum and for Glass fiber is maximum. For hybrid 1 and 2, the flexural strength is found between the Banana and Glass fiber composites. The average flexural strength of Banana fiber composite is 15.68

MPa, for hybrid 1 is 55.95 MPa and for hybrid 2 is found to be 79.99 MPa which suggests a 256.82 % and 410.14 % increase in flexural strength of hybrid 1 and 2 respectively compared to Banana fiber-reinforced composite. The flexural modulus also follows a similar trend of flexural strength.

From the above discussion, it can be said that adding two layers of Glass fiber roving along with two Banana fiber layers can significantly increase the tensile and flexural strength of the composite compared to pure Banana fiber-reinforced composite.

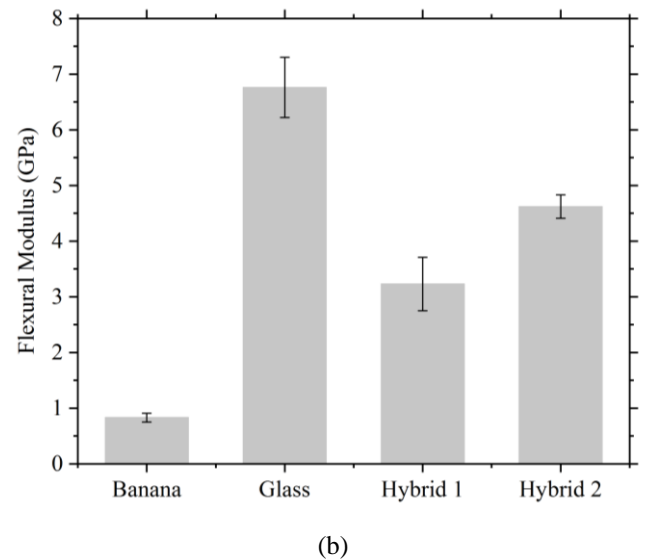
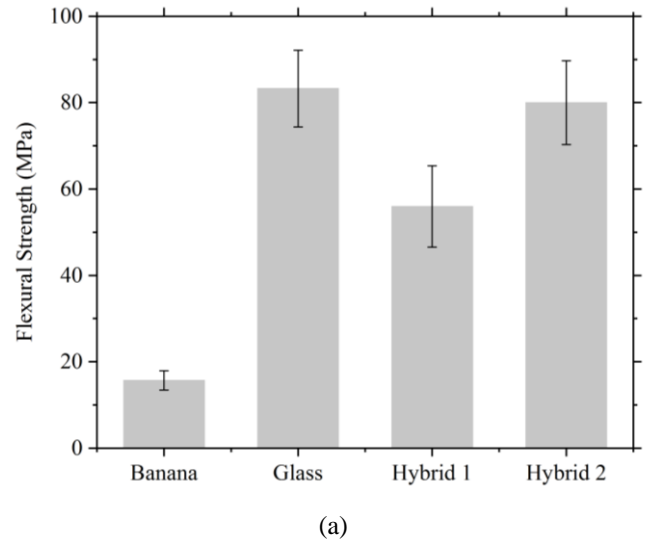


Fig. 9 Flexural test results (a) Strength and (b) Modulus.

### 4 Conclusion

In this paper, the mechanical properties of four different types of composites are investigated. It is found that adding glass fiber layers along with Banana fiber can significantly increase the tensile and flexural strength compared to banana fiber reinforced composite. Adding glass fiber mat layers in banana fiber composite increased the tensile and flexural strength by 19.44 % and 256.82 % respectively while adding glass fiber roving increased these strengths by 93.20 % and 410.14 %. So, significant improvement in the tensile and flexural strength is found by adding glass fiber roving with banana fiber. This investigation suggests that the hybrid composites can be used in the automobile door panel, household roofing panel etc.

## References

- [1] Islam, M.S., Avila, R., Castellanos, A.G. and Prabhakar, P., 2016. Hybrid textile composites as potential cryogenic tank materials. In 57th AIAA/ASCE/AHS/ASC Structures, Structural Dynamics, and Materials Conference (p. 1237).
- [2] Elbadry, E.A., Aly-Hassan, M.S. and Hamada, H., 2012. Mechanical properties of natural jute fabric/jute mat fiber reinforced polymer matrix hybrid composites. *Advances in Mechanical Engineering*, 4, pp.354547.
- [3] Gupta, M.K. and Srivastava, R.K., 2016. Mechanical, thermal and water absorption properties of hybrid sisal/jute fiber reinforced polymer composite. *Indian Journal of Engineering & Materials Sciences*, 23, pp. 231-238.
- [4] Rafiquzzaman, M., Islam, M., Rahman, H., Talukdar, S. and Hasan, N., 2016. Mechanical property evaluation of glass-jute fiber reinforced polymer composites. *Polymers for Advanced Technologies*, 27(10), pp.1308-1316.
- [5] Muñoz, E. and García-Manrique, J.A., 2015. Water absorption behaviour and its effect on the mechanical properties of flax fibre reinforced bioepoxy composites. *International journal of polymer science*, 2015.
- [6] Islam, M.S., Azmy, S. and Almamun, A., 2019. Comparative study on mechanical properties of banana and rattan fiber reinforced epoxy composites. *American Journal of Engineering Research (AJER)*, 8(2), pp.1-6.
- [7] Maleque, M.A., Belal, F.Y. and Sapuan, S.M., 2007. Mechanical properties study of pseudo-stem banana fiber reinforced epoxy composite. *The Arabian journal for science and engineering*, 32(2B), pp.359-364.
- [8] Pothan, L.A., Oommen, Z. and Thomas, S., 2003. Dynamic mechanical analysis of banana fiber reinforced polyester composites. *Composites Science and technology*, 63(2), pp.283-293.
- [9] Sharma, N.K. and Kumar, V., 2013. Studies on properties of banana fiber reinforced green composite. *Journal of Reinforced Plastics and Composites*, 32(8), pp.525-532.
- [10] Venkateshwaran, N., ElayaPerumal, A. and Jagatheeshwaran, M.S., 2011. Effect of fiber length and fiber content on mechanical properties of banana fiber/epoxy composite. *Journal of Reinforced Plastics and Composites*, 30(19), pp.1621-1627.
- [11] Joseph, S., Sreekala, M.S., Oommen, Z., Koshy, P. and Thomas, S., 2002. A comparison of the mechanical properties of phenol formaldehyde composites reinforced with banana fibres and glass fibres. *Composites Science and Technology*, 62(14), pp.1857-1868.
- [12] Asif, M., Rahman, K.A., Faisal, M.O. and Islam, M.S., 2020. Comparative Study on Mechanical Properties of Bamboo and Bamboo-glass Fiber Reinforced Hybrid Composites. *Journal of Engineering Advancements*, 1(01), pp.06-10.
- [13] Chakrabarti, D., Islam, M.S., Jubair, K. and Sarker, M.R.H., 2020. Effect of Chemical Treatment on the Mechanical Properties of Luffa Fiber Reinforced Epoxy Composite. *Journal of Engineering Advancements*, 1(02), pp.37-42.
- [14] <https://www.eppcomposites.com/hand-layup-process.html> last accessed October 22, 2021.
- [15] Standard, A.S.T.M., 2008. Standard test method for tensile properties of polymer matrix composite materials. ASTM D3039/D M, 3039, p.2008.
- [16] ASTM D7264, 2007. Standard test method for flexural properties of polymer matrix composite materials. American Society for Testing and Materials Annual Book of ASTM Standards.

# Numerical Analysis of Natural Convection Heat Transfer Inside an Inverted T-Shaped Cavity Filled with Nanofluid

Gopal Sen\*, Mohammad Ilias Inam

Department of Mechanical Engineering, Khulna University of Engineering & Technology, Khulna-9203, Bangladesh

Received: August 19, 2021, Revised: November 12, 2021, Accepted: November 13, 2021, Available Online: November 29, 2021

## ABSTRACT

This assessment is centered on the characteristics of natural convection heat transfer of Aluminium Oxide-Air nanofluid inside an inverted T-shaped enclosure with differentially heated sidewalls. The left edges of the enclosed cavity have been treated as a heated wall and are kept at a constant temperature. The right edges are also maintained at a constant temperature but lower than the heated wall. The top and bottom faces of the cavity have been considered adiabatic. The evaluation has been numerically investigated using ANSYS fluent. The effect of different significant parameters like volume fraction of nanoparticles, the shape of the enclosure, and Rayleigh number on the heat transfer characteristics inside an inverted T shape enclosure have been investigated. In this numerical analysis, a series of DNS simulations have been conducted for different Rayleigh numbers in the range of  $10^3$  to  $10^6$ , the volume fraction of particles in the range  $0 \leq \phi \leq 0.1$ , and for the different aspect ratios for the inverted T shape have been conducted. The outcomes of this CFD analysis indicate a remarkable rise in the average heat transfer coefficient with the rising volume fraction of  $Al_2O_3$  particles in the air. An increase of the average Nusselt number was also observed with the increase of Rayleigh number, but it drops slightly at a higher volume fraction of nanoparticles due to an increase in conductive heat transfer. For Rayleigh numbers  $\geq 10^4$ , both the average Nusselt number and average heat transfer coefficient decrease up to a certain shape of the cavity aspect ratio. After that cavity aspect ratio, both the parameters value increase. But in the case of Rayleigh number =  $10^3$ , both of the values decrease with the increase in the cavity aspect ratio.

Keywords: Natural Convection, Inverted T-shape,  $Al_2O_3$  Nanoparticle, CFD, Nusselt Number.



This work is licensed under a [Creative Commons Attribution-Non Commercial 4.0 International License](https://creativecommons.org/licenses/by-nc/4.0/).

## 1 Introduction

The natural convective heat transfer process has been practiced by engineers as well as scientists all over the world within the ancient time having a noteworthy augmentation in the cooling mechanism of enormous engineering systems because of its being simple, cheap at cost, comparatively low commotion, little in size, and for having unwavering quality. A survey has been demonstrated that investigating the natural convection characteristics in closed cavities having different shapes and sizes has originated significant zeal among analysts in the preceding decades. In the greater part of such investigations, it has been invented that using only base fluids as a heat transfer medium in the enclosure possesses lower thermal conductivity, which puts a limit on the increment of heat transfer in the walled-in area. Conventional fluids, as like water, ethylene glycol, and also different engine oils are typically utilized as base heat transfer fluids. Nanofluids, which are created from dispersed nano-sized particles in general conventional fluids are profoundly effective liquids in the case of heat transfer that is used in various industrial and mechanical applications. Choi [1] built up the possibility of a nanofluid and it made a tremendous transformation in the case of heat transfer in fluids. The nanoparticle size utilized in nanofluids is from 1 nm to 100 nm. Such nanoparticles can be made of variant metal materials, for instance, copper, silver, or from metal oxides, for example, aluminum oxide, copper and diamond oxide, and carbon nanotubes [2]. It is normal that using nanoparticles in nanofluids gradually enhance the heat conductivity and in this way generously upgrade various heat transfer characteristics of those nanofluids. Eastman et al. [3], Xie et al. [4], and Jana et al. [5]

demonstrated that higher heat transfer ability can be accomplished in thermal systems using nanofluids. Xuan and Li [6] tentatively concentrated on the heat conductivity of a nanofluid comprising Cu nanoparticles mixed with base fluid. Their information clarified that dispersed nanoparticles expanded the heat conductivity than using pure fluid only. Thermal conductivity of nanofluid increases in a gradual way with expanding the volume portion of nanoparticles. For instance, the heat conductivity of Cu–water nanofluid rises from 1.24 to 1.78 then the base fluid when the volume fraction of Cu particles has been changed from 2.5 to 7.5%. Comparable behavior was accounted for by Eastman et al. [7], who got a 60% expansion in heat conductivity with a 5% volume fraction of CuO particles dispersed in water. Nnanna [8] tentatively analyzed the heat transfer conduct of a buoyancy-driven  $Al_2O_3$ -water nanofluid in a 2-D rectangular enclosed cavity that has differentially heating vertical walls and adiabatic horizontal walls. He built up an experimental relation for Nusselt number having a close relationship with the volume fraction percentage of the nanoparticles as well as Rayleigh number and contended that the upgraded heat transfer value can be accomplished at a little volume portion of nanoparticles.

Mohamed Ali et al. [9] experimented on natural convection heat transfer that has been carried out inside vertical and circular enclosures and that are filled with Aluminium–water nanofluid having different concentrations such as 0.0%, 0.85%, 1.98, and 2.95% by mass. The results of this experiment show that the Nusselt number found for alumina–water nanofluid is less than base fluid. C.J. Ho et al. [10] undertook an experiment on natural convection heat transfer of alumina-water nanofluid in some

vertical square enclosures having different sizes. For the nanofluid containing a much lower particle fraction of 0.1 volume, the percentage of heat transfer increased by around 18% compared with that of water. It is apparent from the discussion that the heat conductivity of nanofluids is a summation component of conductivity of base fluid and the nanoparticle material, volume fraction percentage, the enclosure surface portion, and the shape of nanoparticles dispersed. There has not any hypothetical formula as of the present time accessible for determining the exact forecast of the heat conductivity of nanofluid. A few examinations of convective heat transfer using nanofluid have been accounted for in the discussion. Literature discussion shows that there is no comprehensive and analytical study on natural convection heat transfer of nanofluid inside an inverted T-shaped cavity including an air-based mixture of nanoparticles functionalized multi-walled Aluminium made cavity. There is no comprehensive and analytical study on natural convection heat transfer of nanofluid inside an inverted T-shaped cavity having an air-based mixture of nanoparticles functionalized multi-walled Aluminium made cavity. T shape cavities can be used in different heat transfer applications. Air is abundant in the environment and can be easily collected. Its collection is a very cheap process. But it is rarely used as a heat transfer base fluid because it is very low thermal conductive. As air is low heat-conductive, particle volume fraction up to 10% has been used here. Very few assessments can be found where such a huge amount of volume fraction has been used. Therefore, the purpose of the analytical study is for considering the natural convection of nanofluid inside of an inverted T-shaped cavity for various Rayleigh numbers, particle volume percentage, and geometric variables.

## 2 Problem Statement

The geometry of an inverted T-shaped cavity is shown in Fig. 1. The uppermost surface is denoted as  $x$  and the bottom surface is denoted as  $L$ . The length of  $L$  is constant 0.1 m. Then the analysis has been performed for different  $x/L$  Ratios. That ratio is been expressed by  $\chi$ . It is to be noted that  $x=y$  for all the enclosure shapes. Firstly, free convective heat transfer characteristics were determined using only air inside the cavity. Then the nanoparticles have been added gradually. The nanofluid is air-based which has  $Al_2O_3$  as nanoparticles. In this study,  $Al_2O_3$  nanoparticles with a 2 nm average diameter were mixed with air with different concentrations (1–10% volume fraction). A series of Rayleigh numbers that vary from  $10^3$  to  $10^6$  was considered for the determination of the average heat transfer coefficient and the average Nusselt number. On this direct simulation process, it has been assumed that the flow was steady, incompressible, and 2D. Additionally, Boussinesq approximation has also been considered running these DNS simulations. Therefore, the purpose of the numerical study is to analyze natural convection heat transfer of nanofluid inside an inverted T-shaped cavity for various Rayleigh numbers, particle volume percentage, and geometric variables.

### 2.1 Boundary Conditions

The temperature of the heated wall is 310K and it is constant. On the other side, the temperature of the cooled wall is 300K as constant. The flow inside the enclosure has been assumed to be laminar. The upper and lower walls of the cavity are kept thermally insulated (denoted by  $x$  and  $L$  in Fig. 1). It is assumed that the base fluid of the mixture (i.e. air) and the

nanosized particles are in a thermal equilibrium state as well as a no-slip condition has been assigned between them. The thermo-physical properties of the nanofluid are thought to be consistent except for the variation of density and which is approximated by the Boussinesq model.

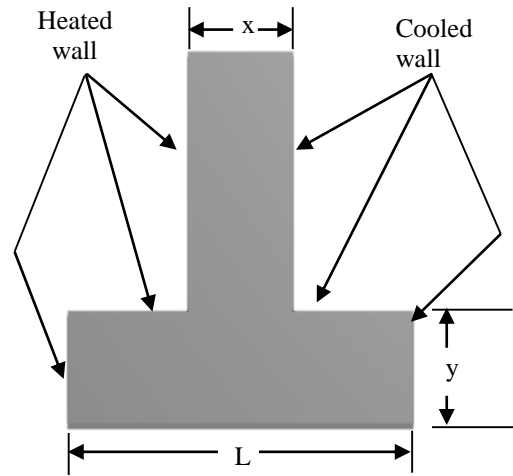


Fig. 1 Geometry as well as the boundary conditions of the inverted T shaped enclosure considered in this analysis

## 3 Mathematical Modeling Details

The continuity, momentum equation following Boussinesq approximation, and energy equations that have been used for the laminar and steady-state natural convection heat transfer inside the 2-D shaped enclosure can be written in dimensional forms as follows:

*Continuity Equation for mixture model:*

$$\frac{\partial}{\partial t} (\rho_m) + \nabla \cdot (\rho_m \vec{v}_m) = 0 \quad (1)$$

where  $\vec{v}_m$  is the mass-averaged velocity and  $\rho_m$  is the mixture density.

*Momentum Equation for mixture model:*

$$\begin{aligned} \frac{\partial}{\partial t} (\rho_m \vec{v}_m) + \nabla \cdot (\rho_m \vec{v}_m \vec{v}_m) \\ = -\nabla p + \nabla \cdot [\mu_m (\nabla \cdot \vec{v}_m + \nabla \cdot \vec{v}_m^T)] \\ + \rho_m \vec{g} + \vec{F} \\ + \nabla \cdot \left( \sum_{k=1}^n \alpha_k \rho_k \vec{v}_{dr,k} \vec{v}_{dr,k} \right) \end{aligned} \quad (2)$$

where  $n$  is the number of phases,  $\vec{F}$  is a body force, and,  $\mu_m$  is the viscosity of the mixture.  $\vec{v}_{dr,k}$  is the drift velocity for secondary phase  $k$ .

*Energy Equation for mixture model:*

$$\begin{aligned} \frac{\partial}{\partial t} \sum_{k=1}^n (\alpha_k \rho_k E_k) + \nabla \cdot \sum_{k=1}^n (\alpha_k \vec{v}_k (\rho_k E_k + p)) \\ = \nabla \cdot (k_{eff} \nabla T) + S_E \end{aligned} \quad (3)$$

where  $k_{eff}$  is the effective conductivity ( $\sum \alpha_k (k_k + k_t)$ ), where  $k_t$  is the turbulent thermal conductivity, defined according

to the turbulence model being used. The first term on the right-hand side of Eq. (6) represents energy transfer due to conduction.  $S_E$  includes any other volumetric heat sources.

The effective density ( $\rho_{nf}$ ) and heat capacitance ( $(\rho C_p)_{nf}$ ) of the nanofluid are defined as [11]:

$$\rho_{nf} = (1 - \phi)\rho_f + \rho_s\phi \tag{4}$$

$$(\rho C_p)_{nf} = (\rho C_p)_f(1 - \phi) + (\rho C_p)_s\phi \tag{5}$$

where  $\phi$  is the solid volume fraction of nanoparticles in the mixture. Thermal diffusivity of the nanofluids is,

$$\alpha_{nf} = \frac{k_{nf}}{(\rho C_p)_{nf}} \tag{6}$$

and the thermal expansion coefficient of the nanofluids has been determined by the following equation,

$$\beta_{nf} = \beta_f(1 - \phi) + \beta_s\phi \tag{7}$$

The equation of dynamic viscosity of the nanofluids given by Brinkman [12] is,

$$\mu_{nf} = \frac{\mu_f}{(1 - \phi)^{2.5}} \tag{8}$$

The effective thermal conductivity of nanofluid can be estimated by the Maxwell–Garnetts [13] model as following:

$$\frac{k_{nf}}{k_f} = \frac{k_s + 2k_f - 2\phi(k_s - k_f)}{k_s + 2k_f + 2\phi(k_s - k_f)} \tag{9}$$

The use of Eq. (9) is restricted for spherical sized nanoparticles only so that it cannot be accounted for other shapes of nanoparticles

Nusselt number and Rayleigh number are defined as follows:

$$Nu = \frac{hL}{k} \tag{10}$$

$$Ra = \frac{g\beta\Delta T x^3}{\nu\alpha}$$

The thermophysical properties of base fluid air and Nanoparticles are given in Table 1 below:

Table 1 Thermophysical properties of air [14] and nano-particle [15].

Property	Unit	Air	Al <sub>2</sub> O <sub>3</sub>
$\rho$	(kg/m <sup>3</sup> )	1	3880
$C_p$	(J/kgK)	1006.43	765
$K$	(W/mK)	0.0242	42.64
$\beta$	(1/K)	3.2*10 <sup>-9</sup>	8.46*10 <sup>-6</sup>

## 4 Results and Discussion

### 4.1 Grid Independence Test

The solutions found for using different mesh sizes in geometry have been studied for generating the independence of each solution. The grid independence test has been conducted for

an enclosure having an x/L ratio of 0.5. The cavity has been assumed to be filled with air and 1% Al<sub>2</sub>O<sub>3</sub> mixture nanofluid. The test has been conducted for Ra=10<sup>5</sup> as well as the average Nusselt number for each mesh has been recorded. The meshes have been produced using the all triangular method. It is clear from Fig. 2 that there is a slight change in the average Nusselt number for mesh elements 30000.

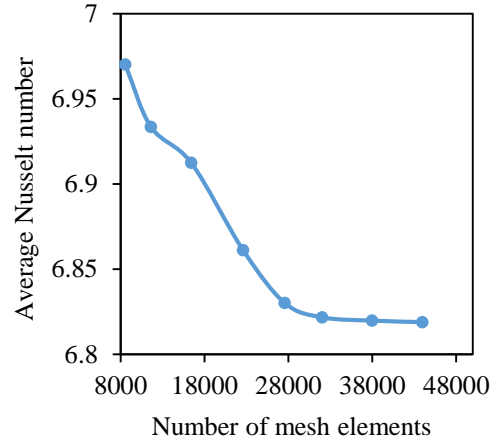


Fig. 2 Variation of average Nusselt number with the mesh elements

### 4.2 Model Validation

The model has been validated with solutions obtained from two previously published research articles that are shown in Table 2. Natural convection occurs air inside a square-shaped hollow cavity whose two sides are kept in different temperatures keeping the upper and lower surfaces at an adiabatic state might be a perfect case for model validation. The average Nusselt number has been calculated for the air-filled square cavity for four different Rayleigh numbers. Then the present work values have been compared with the values available within the literature. As a result, the values of average Nusselt numbers obtained from the present investigation are approximately the same within the values in the literature.

Table 2 Comparison of average Nusselt number for an air-filled square enclosure obtained by various studies with present study for various Rayleigh numbers.

Ra	Nu		
	Present work	N. C. Markatos [14]	Vahl Davis [15]
10 <sup>3</sup>	1.117	1.108	1.118
10 <sup>4</sup>	2.248	2.201	2.243
10 <sup>5</sup>	4.55	4.430	4.519
10 <sup>6</sup>	8.949	8.754	8.799

### 4.3 Effects of Volume Fraction of Nanoparticle on Heat Transfer

The effects of nanoparticles on the stream functions and temperature distribution are shown in Fig. 3 to Fig. 14 for  $\chi=0.3, 0.6,$  and  $0.9$  with nanoparticles for Ra= 10<sup>5</sup> and 10<sup>6</sup>. As it is seen the velocity components increase gradually with increasing particle volume fraction and it accelerates the energy transport within the nanofluid inside the enclosed cavity.

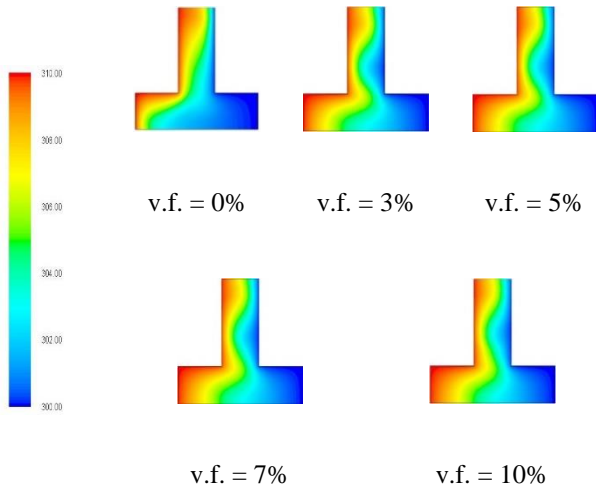


Fig. 3 Contours of Static temperature with and without Nanoparticle (For  $\chi=0.3$  and  $Ra=10^5$ )

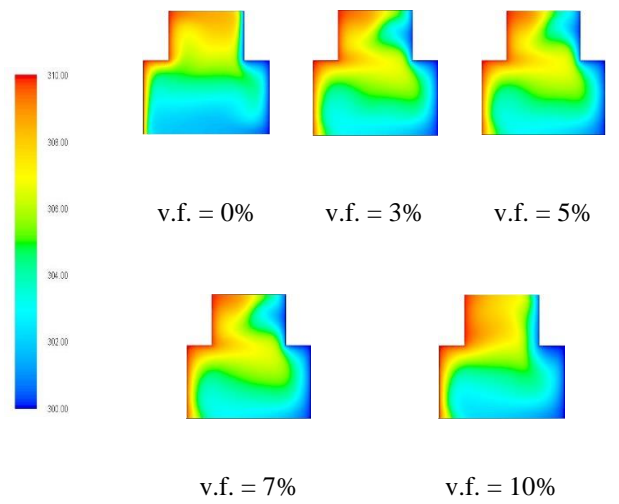


Fig. 6 Contours of Static temperature with and without Nanoparticle (For  $\chi=0.6$  and  $Ra=10^6$ )

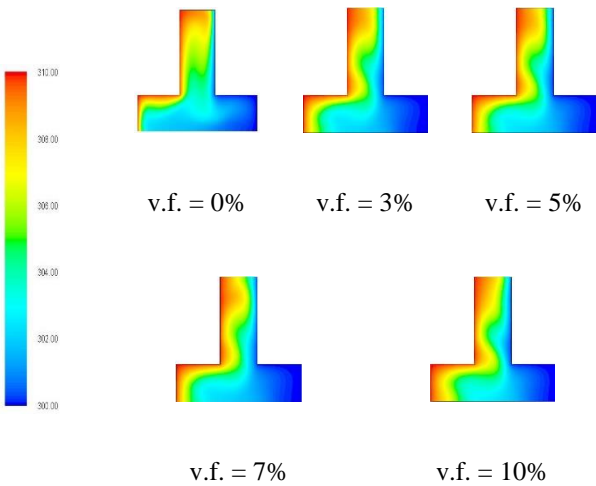


Fig. 4 Contours of Static temperature with and without Nanoparticle (For  $\chi=0.3$  and  $Ra=10^6$ )

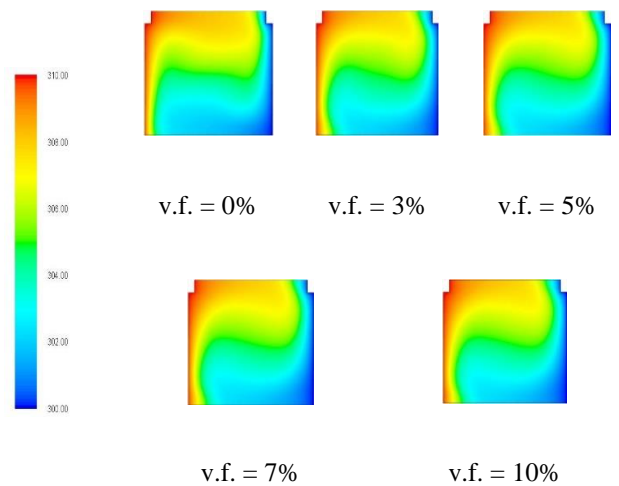


Fig. 7 Contours of Static temperature with and without Nanoparticle (For  $\chi=0.9$  and  $Ra=10^5$ )

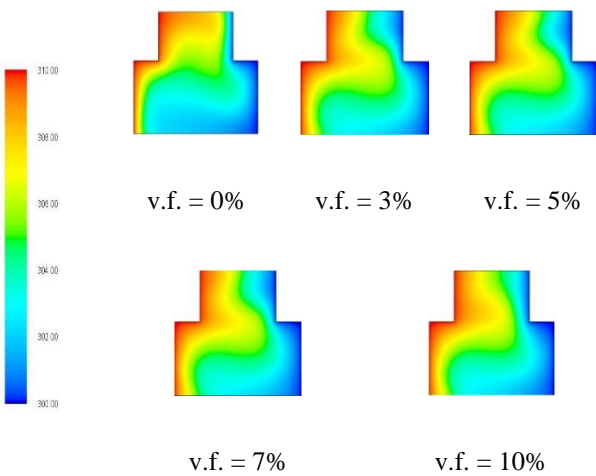


Fig. 5 Contours of Static temperature with and without Nanoparticle (For  $\chi=0.6$  and  $Ra=10^5$ )

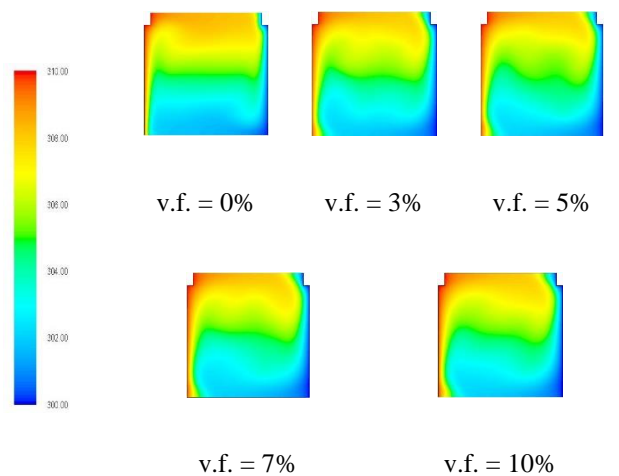


Fig. 8 Contours of Static temperature with and without Nanoparticle (For  $\chi=0.9$  and  $Ra=10^6$ )

Thus, the real values of stream functions pointing that the strength of flow rises with the gradual rising of the volume fraction of nanofluid on the air and so the contour gets formed into a regular shape with the higher volume fraction. Maximum values of the stream functions are being increased with the increasing volume fraction and so, the streamline contours take a more regular shape in higher volume fractions. The change is due to equivalent thermal conductivity. For lesser volume fractions, the temperature change apportions within the fluid is also less than those of higher volume fractions. For high volume fraction change in temperature distribution is more prominent than a lower volume.

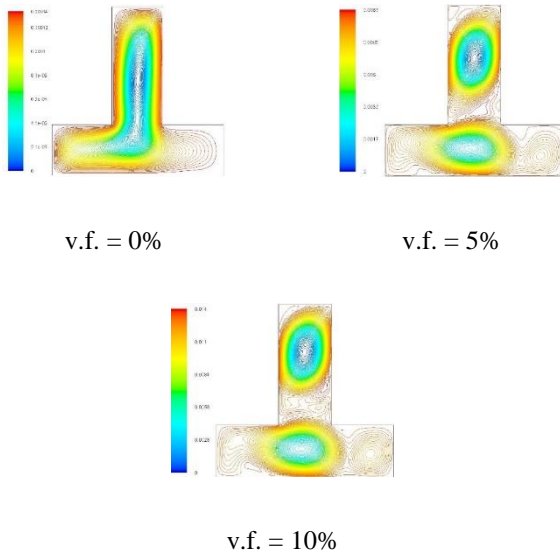


Fig. 9 Contours of Stream function with and without Nanoparticle (For  $\chi=0.3$  and  $Ra=10^5$ )

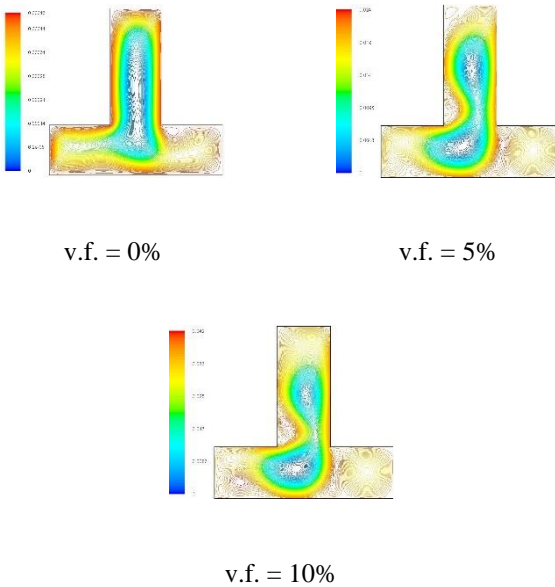


Fig. 10 Contours of Stream function with and without Nanoparticle (For  $\chi=0.3$  and  $Ra=10^6$ )

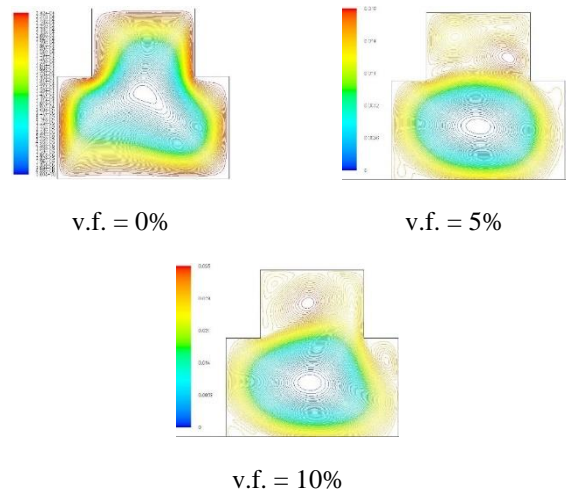


Fig. 11 Contours of Stream function with and without Nanoparticle (For  $\chi=0.6$  and  $Ra=10^5$ )

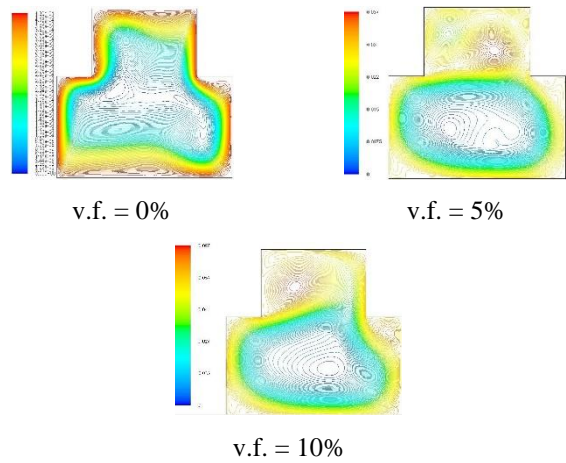


Fig. 12 Contours of Stream function with and without Nanoparticle (For  $\chi=0.6$  and  $Ra=10^6$ )

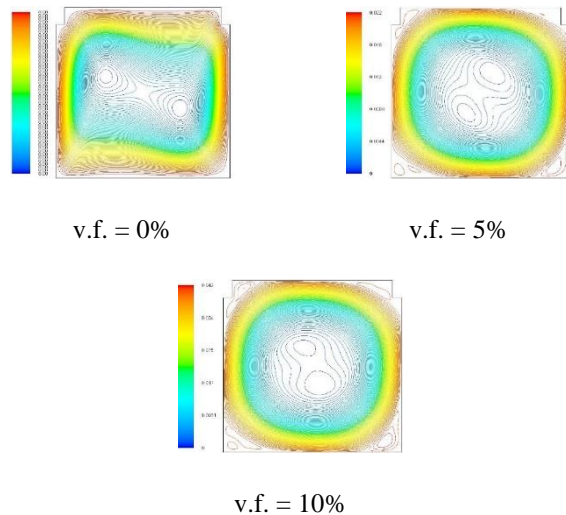


Fig. 13 Contours of Stream function with and without Nanoparticle (For  $\chi=0.9$  and  $Ra=10^5$ )

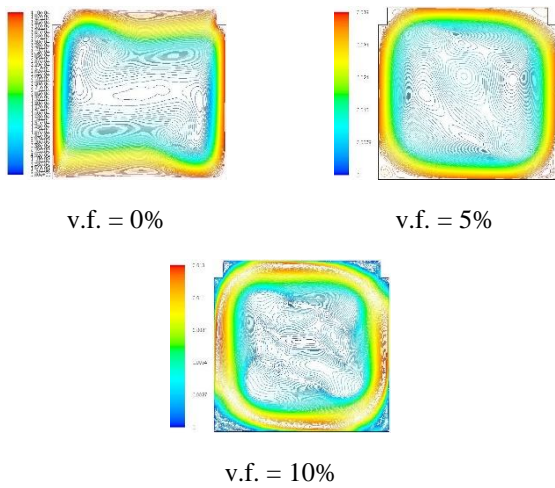
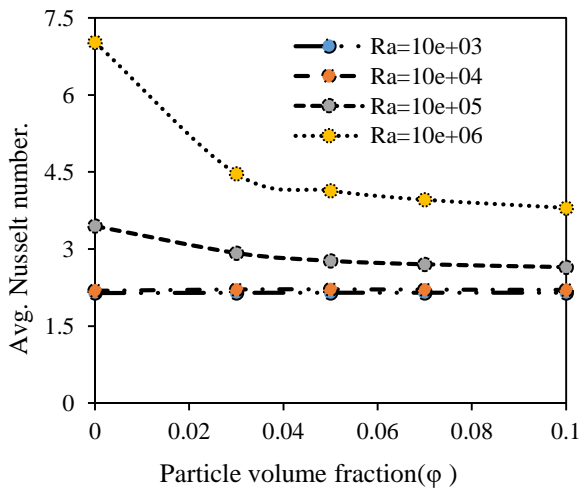
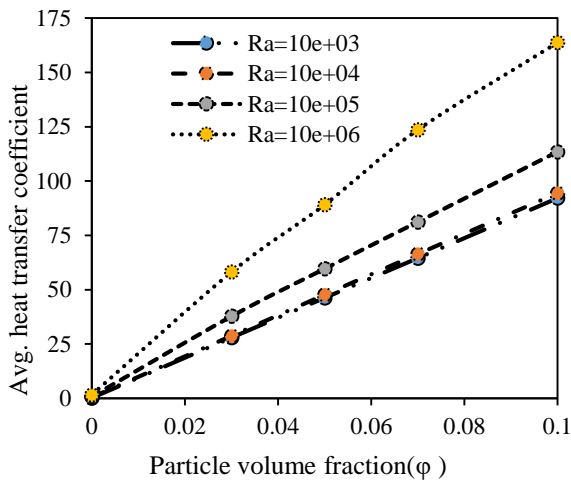


Fig. 14 Contours of Stream function with and without Nanoparticle (For  $\chi=0.9$  and  $Ra=10^6$ )



(a)



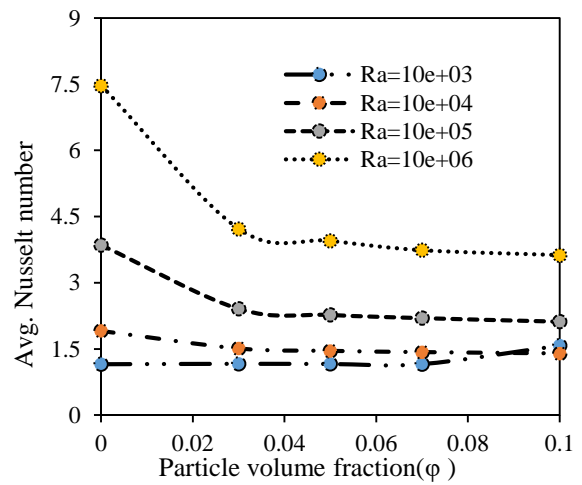
(b)

Fig. 15 Variation of average (a) Nusselt number and (b) Average convective heat transfer coefficient with volume fraction for different Rayleigh numbers (for  $\chi=0.3$ )

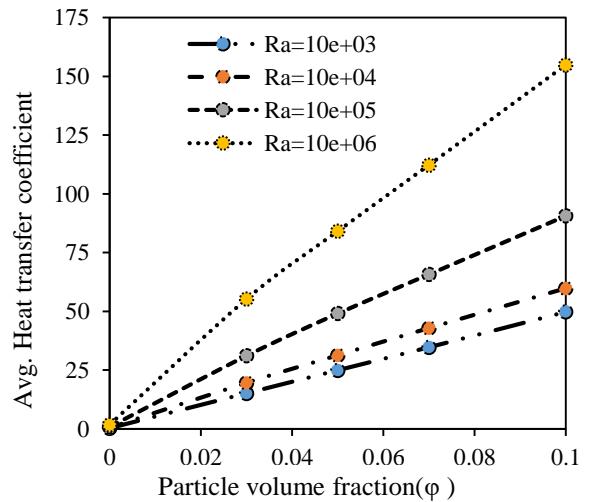
A higher rate of thermal conductivity of nanofluid may be attained by having a higher rate of thermal diffusivity. The high thermal diffusivity results in a drop of temperature gradients and so increases the boundary thickness. Such an increase in the thermal boundary layer thickness reduces the Nusselt number.

With the rising Rayleigh number, the highest magnitude of the stream functions also rise. These phenomena occur because of the buoyancy effect. The consequences of the Rayleigh number on the average Nusselt number and average heat transfer coefficient can also be seen in the figures. Both of those parameter values gradually rise with the increment of Rayleigh number in all the shapes of enclosures.

A variation on temperature and stream function for different  $x/L$  ratios of the cavity ( $\chi$ ) can also be seen on the contours above. With the increasing value of  $\chi$ , there is a significant difference in the contours. It has been seen by analyzing the contours that temperature distribution, as well as stream function, is prominently maximum when  $\chi$  approximates unity.



(a)



(b)

Fig. 16 Variation of average (a) Nusselt number and (b) convective heat transfer coefficient with volume fraction for different Rayleigh numbers (for  $\chi=0.6$ )

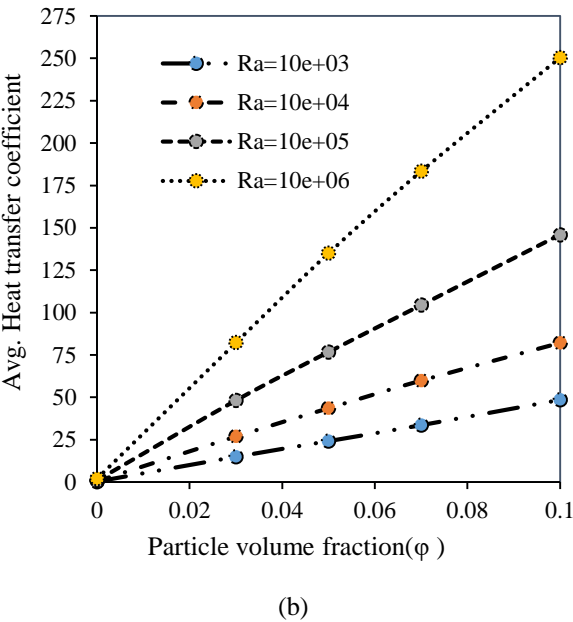
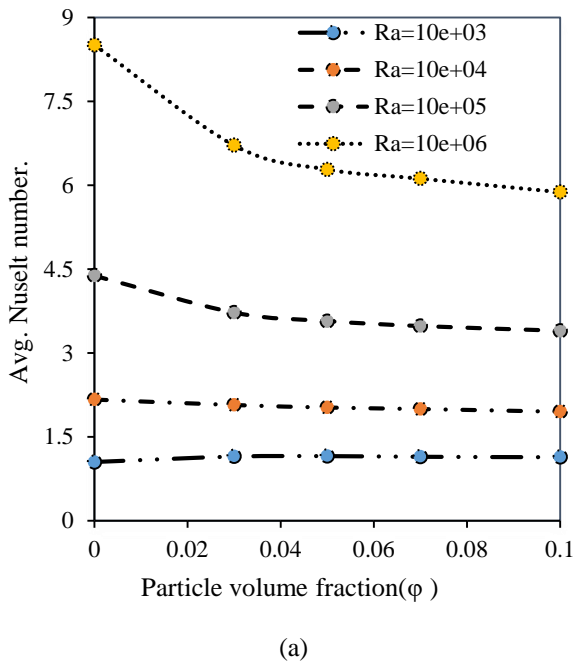


Fig. 17 Variation of average (a) Nusselt number and (b) convective heat transfer coefficient with volume fraction for different Rayleigh numbers (for  $\chi=0.9$ )

Fig. 15-Fig. 17 show that the average heat transfer coefficient rises with the growing volume fraction and Nusselt number downfalls with the rising volume fraction. The reason for happening this is, besides the increasing convective heat transfer coefficient, thermal conductivity also rises so that increase in conductive heat transfer is more significant than convection. From Fig. 9(a), Fig. 10(a) and Fig. 11(a), an increase of average Nusselt number can be observed with the increase of Rayleigh number, but it drops slightly at a higher volume fraction of nanoparticles due to an increase in conductive heat transfer.

#### 4.4 Effect of Rayleigh Number on Heat Transfer

Contours of static temperature and stream functions are exhibited in Fig. 18-23. With the increasing Rayleigh number, there occur noteworthy changes in the contours. For less value of

Rayleigh number, there is a slight change in the contour, but with the gradual rise of Rayleigh number, there is noteworthy variation in temperature distribution. In the case of stream function, with rising Rayleigh number highest magnitude of stream function also rises. These phenomena occur because of the buoyancy effect. The consequences of the Rayleigh number on the average Nusselt number and average heat transfer coefficient can also be seen in Fig. 15-17. Both of those parameter values gradually rise with the increment of Rayleigh number in all the shapes of enclosures.

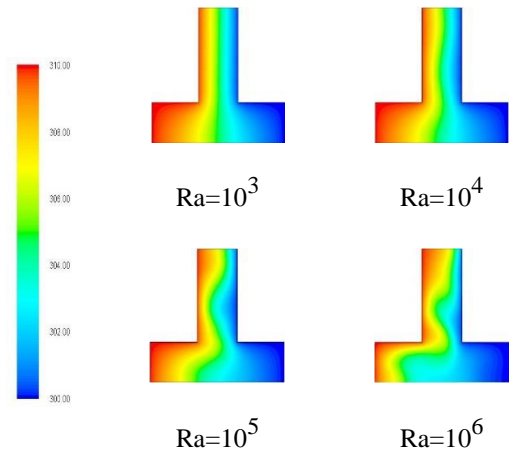


Fig. 18 Contours of Static temperature for different Rayleigh number (for  $\phi = 0.1$  and  $\chi = 0.3$ )

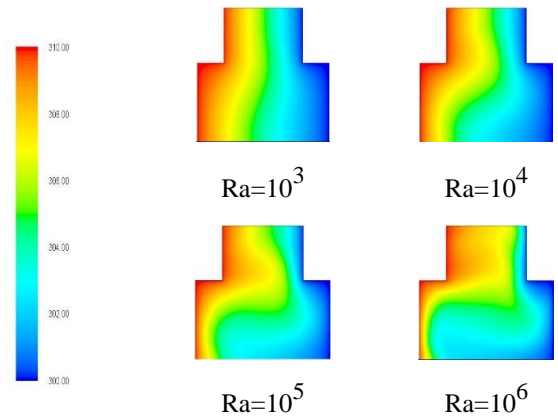


Fig. 19 Contours of Static temperature for different Rayleigh number (for  $\phi = 0.1$  and  $\chi = 0.6$ )

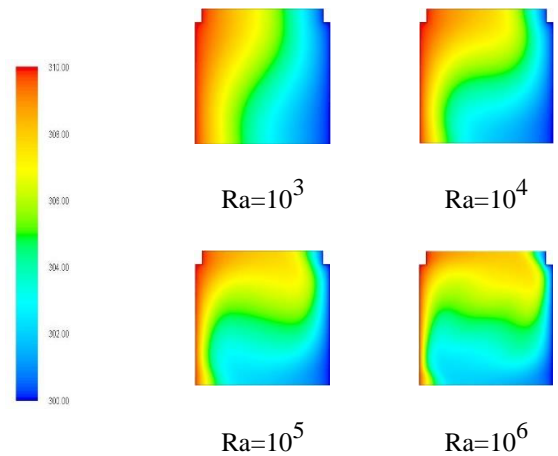


Fig. 20 Contours of Static temperature for different Rayleigh number (for  $\phi = 0.1$  and  $\chi = 0.9$ )

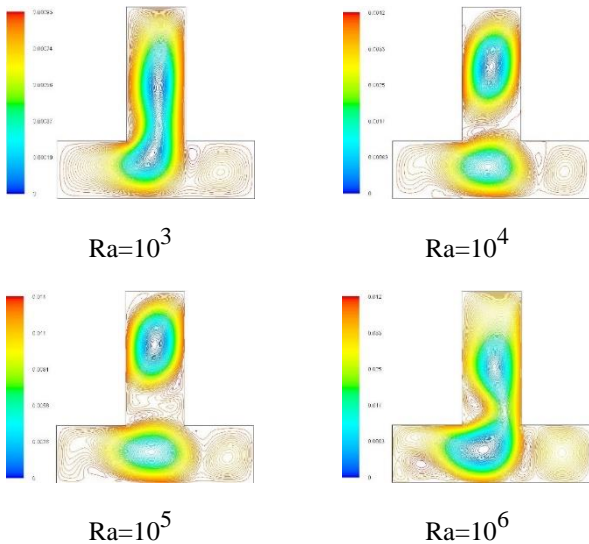


Fig. 21 Contours of Streamlines for different Rayleigh number (for  $\phi = 0.1$  and  $\chi = 0.3$ )

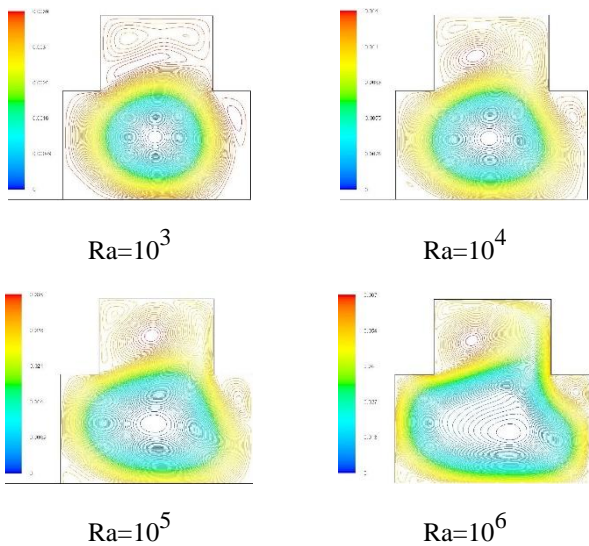


Fig. 22 Contours of Streamlines for different Rayleigh number (for  $\phi = 0.1$  and  $\chi = 0.6$ )

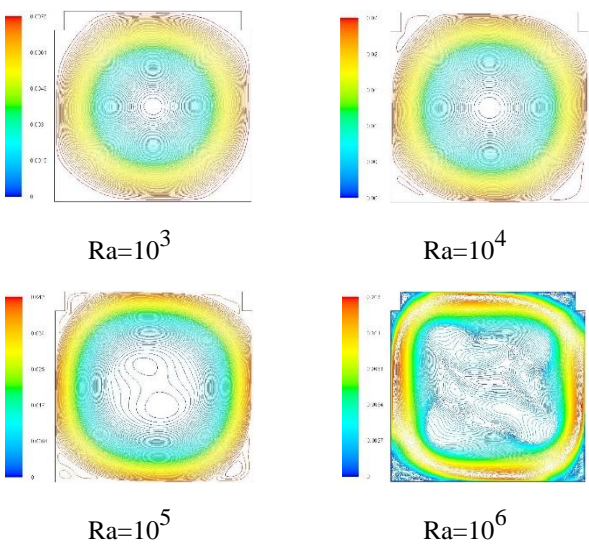
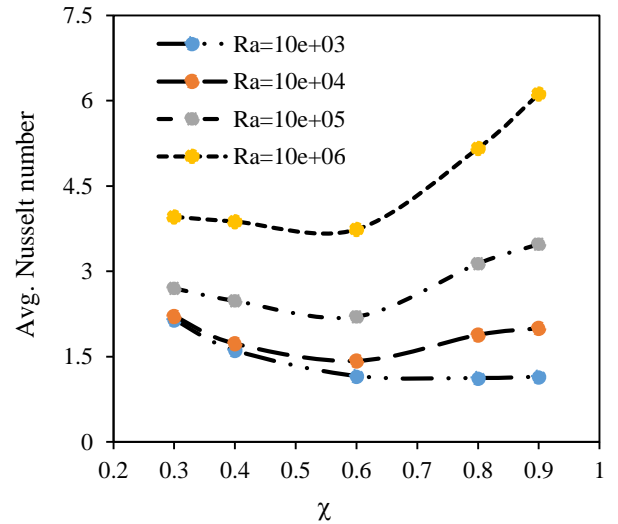


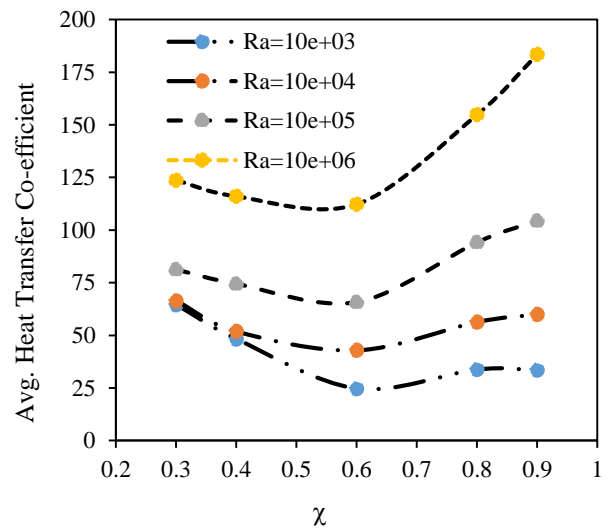
Fig. 23 Contours of Streamlines for different Rayleigh number (for  $\phi = 0.1$  and  $\chi = 0.9$ )

#### 4.5 Effect of $\chi$ of Enclosure on Heat Transfer

Contours of static temperature and streamlines are shown in Fig. 18-23 for different  $x/L$  ratios of the cavity ( $\chi$ ). With the increasing value of  $\chi$ , there is a significant difference in the contours. It has been seen by analyzing the contours that temperature distribution is prominently maximum when  $\chi$  approximates unity. Variations of the average heat transfer coefficient and average Nusselt number are shown in Fig. 24. It is seen that both the average heat transfer coefficient and average Nusselt number decrease up to  $\chi=0.6$  along with the increasing value of the Rayleigh number. Both the parameter value further increase with the increase of the Rayleigh number.



(a)



(b)

Fig. 24 Variation of average (a) Nusselt number and (b) convective heat transfer coefficient with different  $x/L$  ratios for different Rayleigh numbers ( $\phi = 0.07$ )

#### 5 Conclusion

A comprehensive and detailed analysis of natural convection in an inverted T-shaped enclosed cavity filled with nanofluid has been performed. The assessment has been executed to study the enormous increase in heat transfer using

nanofluid instead of pure heat transfer fluids. The parameters that have been investigated in this analysis are -nanoparticle volume fraction, Rayleigh number, and  $x/L$  ratio. Results found in this analysis indicate that-

- A remarkable increase in average heat transfer occurs with the gradual increase in the volume fraction of nanoparticles in the nanofluid. On the other side, the average Nusselt number decreases instead. A maximum 10% nanoparticle volume fraction has been used in this experiment. This analysis could be done using nanoparticle volume fraction beyond 10%. The reduction of the average Nusselt number is slight for lower Rayleigh numbers ( $Ra = 10^3$  and  $10^4$ ), whereas the reduction is prominent in higher Rayleigh numbers ( $Ra = 10^5$  and  $10^6$ )
- Both the Nusselt number and average heat transfer coefficient decrease with an increase in  $x/L$  up to 0.6. After that value of  $x/L$ , both of the parameters start increasing. This occurrence can be seen for  $Ra \geq 10^4$ . In the case of  $Ra=10^3$ , both the parameter's values reduce with the  $x/L$ .
- The value of average heat transfer coefficient as well as avg. Nusselt number rises with the increase of the Rayleigh number.

## References

- [1] Choi, S.U. and Eastman, J.A., 1995. *Enhancing thermal conductivity of fluids with nanoparticles* (No. ANL/MSD/CP-84938; CONF-951135-29). Argonne National Lab., IL (United States).
- [2] Maxwell, J.C., 1873. *A treatise on electricity and magnetism* (Vol. 1). Clarendon press.
- [3] Eastman, J.A., Choi, S.U.S., Li, S., Yu, W. and Thompson, L.J., 2001. Anomalous increased effective thermal conductivities of ethylene glycol-based nanofluids containing copper nanoparticles. *Applied Physics Letters*, 78(6), pp.718-720.
- [4] Xie, H., Lee, H., Youn, W. and Choi, M., 2003. Nanofluids containing multiwalled carbon nanotubes and their enhanced thermal conductivities. *Journal of Applied Physics*, 94(8), pp.4967-4971.
- [5] Jana, S., Salehi-Khojin, A. and Zhong, W.H., 2007. Enhancement of fluid thermal conductivity by the addition of single and hybrid nano-additives. *Thermochimica Acta*, 462(1-2), pp.45-55.
- [6] Xuan, Y. and Li, Q., 2000. Heat transfer enhancement of nanofluids. *International Journal of Heat and Fluid Flow*, 21(1), pp.58-64.
- [7] Eastman, J.A., Choi, U.S., Li, S., Thompson, L.J. and Lee, S., 1996. Enhanced thermal conductivity through the development of nanofluids. *MRS Online Proceedings Library (OPL)*, 457.
- [8] Nnanna, A.A., 2007. Experimental model of temperature-driven nanofluid, *Journal of Heat Transfer*, 129(6), pp. 697-704.
- [9] Ali, M., Zeitoun, O., Almotairi, S. and Al-Ansary, H., 2013. The effect of alumina-water nanofluid on natural convection heat transfer inside vertical circular enclosures heated from above. *Heat Transfer Engineering*, 34(15), pp.1289-1299.
- [10] Ho, C.J., Liu, W.K., Chang, Y.S. and Lin, C.C., 2010. Natural convection heat transfer of alumina-water nanofluid in vertical square enclosures: An experimental study. *International Journal of Thermal Sciences*, 49(8), pp.1345-1353.
- [11] Saleh, H., Roslan, R. and Hashim, I., 2011. Natural convection heat transfer in a nanofluid-filled trapezoidal enclosure. *International Journal of Heat and Mass Transfer*, 54(1-3), pp.194-201.
- [12] Brinkman, H.C., 1952. The viscosity of concentrated suspensions and solutions. *The Journal of Chemical Physics*, 20(4), pp.571-571.
- [13] Maxwell-Garnett, J.C., 1904. Colours in metal glasses and in metallic films. *Phil. Trans. R. Soc. Lond, A*, 203, pp.385-420.
- [14] Ghasemi, B. and Aminossadati, S.M., 2009. Natural convection heat transfer in an inclined enclosure filled with a water-CuO nanofluid. *Numerical Heat Transfer, Part A: Applications*, 55(8), pp.807-823.
- [15] Abouali, O. and Ahmadi, G., 2012. Computer simulations of natural convection of single phase nanofluids in simple enclosures: a critical review. *Applied Thermal Engineering*, 36, pp.1-13.

## NOMENCLATURE

Symbol	Full meaning	Unit of symbol
$S$	Height and Width of Cavity	m
$\phi$	Fraction of nanoparticle volume	
$T$	Temperature	K
$P$	Pressure	Pa
$t$	Time	second
$x, y$	Dimensional Space Coordinate	m
$g$	Gravitational acceleration	$ms^{-2}$
$Ra$	Rayleigh number	
$h$	Heat transfer coefficient	$W\cdot m^{-2}K^{-1}$
$\alpha$	Thermal diffusivity	$m^2s^{-1}$
$\beta$	Thermal expansion coefficient	$K^{-1}$
$\mu$	Dynamic viscosity	$Nsm^{-2}$
$\nu$	Kinematic viscosity	$m^2s^{-1}$
$\rho$	Density	$kg/m^3$
$k$	Thermal conductivity	$W\cdot m^{-1}K^{-1}$
$C_p$	Specific heat	$J\cdot kg^{-1}K^{-1}$
$Nu$	Nusselt number	
$nf$	Nanofluid	
$\chi$	$x/L$ Ratio of the enclosure	

# Assessment of Arsenic and Copper Pollution of the Benya Lagoon, Ghana By Neutron Activation Analysis

M. K. Vowotor\*, R. Edziah, S. S. Sackey, E. K. Amewode, S. B. Frempong

Department of Physics, University of Cape Coast, Cape Coast, Ghana.

Received: October 29, 2021, Revised: December 09, 2021, Accepted: December 10, 2021, Available Online: December 15, 2021

## ABSTRACT

Heavy metal concentrations in some water bodies and the soil beneath these waters. These would have detrimental consequences on these water users and consumers of the fish in that water. Instrumental Neutron Activation Analysis technique using the Ghana Research Reactor-1 was employed to find out the concentrations of two heavy metals, Arsenic (As) and Copper (Cu) in the sediments, fishes, and water collected from the Benya Lagoon in the KEEA, Ghana. Cumulatively, Copper was found to be greater in concentration than Arsenic concerning the three parts of the ecology under study. On the other hand, Arsenic was more concentrated in the sediments than Copper, and Copper was more concentrated in the water and fish than Arsenic. Cumulatively, the level of contamination of Arsenic and Copper decreased in the order fish > sediment > water. Though Arsenic and Copper were found in elevated amounts in both water and fish which rendered the Lagoon water unsuitable for human use and the fish from the Lagoon unsafe for consumption, their concentrations in the sediment were found to have a low ecological risk index on the environment.

Keywords: Benya Lagoon; Heavy Metal Pollution; Health Risk; INAA; Good Drinking Water.



This work is licensed under a [Creative Commons Attribution-Non Commercial 4.0 International License](https://creativecommons.org/licenses/by-nc/4.0/).

## 1 Introduction

Over the last two decades, the pollution of aquatic systems by heavy metals due to activities like urbanization [1] has been an issue of major concern. Heavy metals like Arsenic and Copper, are regarded as severe pollutants due to their toxicity resolution, bioaccumulation, and biomagnifications problems [2]. They are not degraded chemically or biologically and so stay for longer periods in the environment [3].

Heavy metals are natural constituents of water bodies like lagoons and lakes but over the period, the rapid expansion of human activities such as the direct industrial discharges into water bodies, input from weathering, and the effect of local activities nearby such as fishing, sewage disposal, has indeed accelerated the rate of environmental pollution [4]. Agricultural runoffs containing pesticides and fertilizers are normally deposited in the bed sediments and aqueous phases of lagoons and are normally the final destinations for both androgenic components produced or derived from the environment. Sediments function as bowls for a range of pollutants such as heavy metals and pesticides, and they perform a portion in the remobilization of pollution in aquatic schemes as well as the interaction of water and sediment [5].

Copper (Cu), and Arsenic (As), adversely affect all living things as they get integrated into the food chain, get accumulate, and may build up to concentrations that may be harmful to living organisms. Within the aquatic environment, heavy metals are considered toxic at high levels, but in trace amounts, play essential biochemical roles in the life processes of all aquatic life. They are consequently considered micronutrients or trace elements [6].

Below 20 mg of organic Arsenic in humans affects expression of gene, helps reproductive health, and digestive issues. Its overdose, however, makes it carcinogenic, gastrointestinal problems, sources anemia, depression, and even death [7], [8]. Copper, on the other hand, aids in iron, protein and

estrogen metabolism, hormone synthesis and is required by women for the correct functioning of their reproductive system as it boosts their fertility and maintains pregnancy. Nonetheless, high intakes above 10 mg/d can cause nervous system disorders, liver and kidney damages [9], [10].

Generally, fish has been widely studied to identify edible and commercial species and those unsafe for human consumption [11]. A study of samples from a freshwater system is considered as one of the most significant means of estimating the level of metal pollution in that system within that system.

The municipality of Komenda Edina Eguafio Abrem (KEEA) surrounds the Benya Lagoon in Ghana's Central Region and it serves as the hub for many commercial activities some of which include salt mining and fishing. Concerning fishing, the lagoon serves as the habitat for a variety of fish, notable among them being the Sarotherodon Melanrotheron (Blackchin Tilapia). Located along the Gulf of Guinea, Benya Lagoon spans a total length of about 10.19 kilometres (Fig. 1).

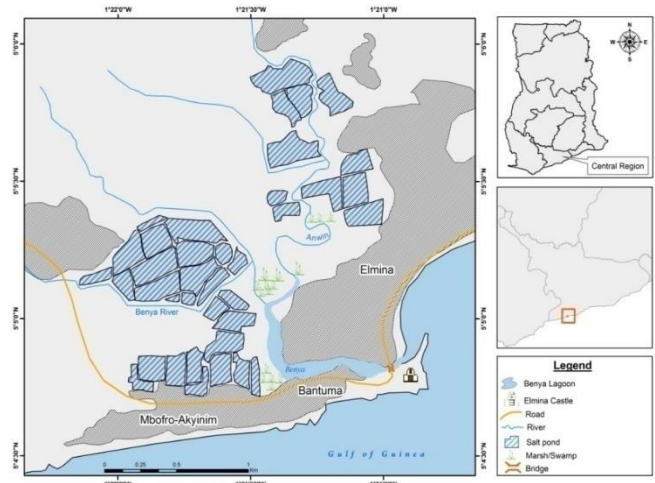


Fig. 1 A map of Benya lagoon [12]

Due to heavy pollution, the lagoon is drying up so the survival of these commercial ventures is however threatened. The Benya lagoon is polluted due to some practices of residents living within the environs of the lagoon. Generally, sanitation within the KEEA municipality is poor, to the extent that liquid and solid wastes disposal facilities are not readily accessible. This has resulted in all manner of wastes being dumped straight into the lagoon without any prior treatment. Some of such wastes include liquid wastes and human excreta from homes being spilled directly into drains and open spaces which in time end up



(a) Dumping of waste around the lagoon



(c) Boats in the Benya Lagoon. Market and shops around the lagoon in the background

in the lagoon and surrounding farms. Others include rubbish generated from domestic activities and commercial ventures like markets, and toxic solid wastes like scrap metals from auto-mechanic shops in the area [12], [13]. Fig. 2 shows the various sources of pollution to the Benya Lagoon.

This study aims at assessing the pollution levels of Arsenic and Copper present in the sediments, water, and fish from the Benya Lagoon using the Ghana Research Reactor-1 located at the Ghana Atomic Energy Commission, which operates on the principles of Instrumental Neutron Activation Analysis (INAA).



(b) Liquid and solid wastes dumped around boat settlement at the background



(d) Refuse and unserviceable/retired boats abandoned along the bank of the lagoon

Fig. 2 Sources of pollution of the Benya lagoon

## 2 Sample Containers and Equipment Preparation

All the sampling apparatus and receptacles used are cleaned before and after use with heavy-metal grade acetone and heavy-metal grade HCl was used as a rinse before putting samples in them. Blank containers are verified first for background contamination, and the results are subtracted from the main data.

### 2.1 Sample Collection

During the sample period, professional fishermen's services were used. Their abilities and boats aided in accessing some of the most difficult-to-reach locations required for the study. Using a sediment coring device, superficial (upper 10cm) random sediment samples were taken in the lagoon. The overlying water was siphoned and into a plastic bowl, the upper 5 cm of sediment from surface-grab was removed with plastic spoon. To make a composite sample, this technique was performed three times within each sampling station and all three sections were placed in the same bowl. They were then mixed using a plastic spoon until a uniform colour and consistency were achieved. To avoid cross-contamination, each composite sediment sample was also placed in a tagged Ziploc plastic bag. They were then put in the fridge at a temperature of  $-10^{\circ}\text{C}$ .

The water samples were obtained by submerging the water sampler beneath the surface of the lagoon. Each water sample was sieved with an inline filter unit, measured into a pre-cleaned 1.5 litre bottle, and coded with indelible ink. 5% suprapur HCl

was added to the filtered water samples for preservation. To avoid cross-contamination, each water sample was also placed in a tagged Ziploc plastic bag. At room temperature, the water sample were stored in the dark before the laboratory analysis.

The fish samples were bought from the fisher mongers around the Benya Lagoon and taken to the laboratory of the Department of Fisheries, University of Cape Coast. The scales of the fish were well removed using a new kitchen stainless steel knife. It was then washed with deionized water, dry-cleaned with blotting paper, and had it separated into its various parts like tissues, bones, and gills. These were then kept in a refrigerator at a temperature of  $-10^{\circ}\text{C}$ . The samples were then transported to the Preparation Laboratory at the Ghana Atomic Energy Commission (GAEC) at Kwabenya, in Accra for analyses. The average concentration of Copper and Arsenic present in the water sample, fish and sediments, were then calculated.

### 2.2 Sample Preparation

The irradiation capsules were cleaned by rinsing them in deionized water after immersing them in an acidic reagent for 24 hours. For another 24 hrs they were soaked in  $\text{HNO}_3$  after which they were thoroughly rinsed with deionized water and air-dried. 1000 ppm single standard reference solution of the elements Arsenic and Copper and were packed the same way as the samples. They were then crammed between the wrapped samples and then all were wrap up together into one polyethylene ampoule for irradiation.

### 2.3 Sample Irradiation and Counting

INAA was used for the determination of the concentration of As and Cu in the water, sediment, and fish samples. Operating at 15 kW, Ghana Research Reactor-1 facility situated at GAEC was used to irradiate the prepared samples, when there is a thermal neutron flow of  $5 \times 10^{11} \text{ ncm}^{-2}\text{s}^{-1}$ . With a pressure of 0.6 MPa, a pneumatic transfer system pushed the samples into the irradiation locations. The half-life of the components of interest was used to classify the irradiation. The induced radioactivity in the samples was counted using PC-based  $\gamma$ -ray spectrometry. A model Modules for electronic devices and a spectroscopic amplifier (model 2020, Canberra Industries Incorporated) were used to connect a computer-based Multichannel Analyzer to a GR2518 n-type high-purity Germanium brand (HPGe) detector. With 1.8 keV energy resolution and  $\gamma$ -ray energy of 1332 keV, the detector has a relative efficiency of 25%. The energy emitted was used to subjectively identify the  $\gamma$ -ray product radionuclides, and the quantitative analysis was completed using the comparator approach to translate the counts to the area beneath the photo peaks. The appropriate amount of chilling time can make all the difference.

### 3 Results

From the investigations carried out, the mean concentration values of Arsenic and Copper obtained for the various samples are shown in Table 1. GHAAR-1 has a detection limit of  $0.00001 \mu\text{g/g}$  for Arsenic and  $0.01 \mu\text{g/g}$  for Copper.

Table 1 Mean concentrations of Arsenic and Copper in the Sediments, Water and Fish from the Benya Lagoon

Element	Sediment (mg/kg)	Water (mg/l)	Fish (mg/kg)
As	$61.9 \pm 29.60$	$0.12 \pm 0.08$	$93.17 \pm 15.44$
Cu	$56.2 \pm 59.50$	$0.08 \pm 0.04$	$123.35 \pm 15.70$

## 4 Analysis and Discussion

### 4.1 Sediment

#### 4.1.1 Heavy Metals Concentration Assessment

The average concentration of As and Cu in the sediments were found to be  $61.9 \pm 29.60 \text{ mg/kg}$  and  $56.2 \pm 59.50 \text{ mg/kg}$ , respectively. The sediment was found to be more concentrated with Arsenic than Copper.

#### 4.1.2 USEPA and CBSOG Assessment

The metals concentrations were matched with sediment conditions proposed by US Environmental Protection Agency (USEPA) [14] and Consensus-Based Sediment Quality Guidelines (CBSOG) [15]. Table 2 shows the limits of the various pollution levels and the mean values obtained from the study.

The USEPA scale has no available data on Arsenic for its levels of pollution. However, using the CBSOG scale, the Benya will be classified as being heavily polluted. For Cu, the lagoon may be considered slightly or heavily polluted concerning the CBSOG and USEPA scale.

Table 2 Comparison of measured concentration values with guidelines for sediments as proposed by USEPA and CBSOG SQG (2003)

Metal	USEPA Pollution Level			CBSOG SQG (2003) Pollution Level			Benya Lagoon Study
	Not	Slightly	Heavily	Not	Slightly	Heavily	Mean
As	----	----	----	< 9.8	9.8 – 21.4	> 21.4	61.9
Cu	<25	25-50	> 50	<25	25-75	>75	56.2

#### 4.1.3 Geo-accumulation Index Assessment

The amount of heavy metal pollution in sediment can be analyzed by determining its geo-accumulation index ( $I_{geo}$ ). This is expressed mathematically in Eq. (1) (reference) as:

$$I_{geo} = \log_2 [C_n/1.5B_n] \tag{1}$$

where  $C_n$  is the concentration of element 'n' and  $B_n$  is the geochemical background value (world surface rock average) [16]. The factor 1.5 is unified to account for likely variants in background data owing to lithogenic influence.

For Cu,  $B_n = 32$  and  $C_n = 56.2$  while for As  $B_n = 13$  and  $C_n = 61.9$ . Substituting these values into equation 1 yields  $I_{geo}$  values of 0.2 and 1.7 for Cu and As respectively.

For its classification, the  $I_{geo}$  scale consists of seven grades (0 – 6) ranging from unpolluted to highly polluted. This is shown in Table 3.

Comparing the calculated  $I_{geo}$  values for Cu and As to the grading system shown in Table 3, it can be deduced that the sediment quality of the Benya lagoon falls within the

'Uncontaminated to moderately contaminated' classification region concerning Cu, while it can be considered 'Moderately contaminated' regarding As.

Table 3  $I_{geo}$  class showing the pollution Grades of Geo-Accumulation Index of Metals class

$I_{geo}$ Class	$I_{geo}$ Value	Sediment Quality
0	$I_{geo} \leq 0$	Uncontaminated
1	$0 < I_{geo} \leq 1$	Uncontaminated to moderately contaminated
2	$1 < I_{geo} \leq 2$	Moderately contaminated
3	$2 < I_{geo} \leq 3$	Moderately to heavily contaminated
4	$3 < I_{geo} \leq 4$	Heavily contaminated
5	$4 < I_{geo} \leq 5$	Heavily to extremely contaminated
6	$5 < I_{geo}$	Extremely contaminated

#### 4.1.4 Assessment According to Contamination Factor, ( $C_F$ )

Another indicator that categorizes the extent of environmental contamination is the  $C_F$ . It is used to assess the

likely anthropogenic contribution of metals in observed sediments [17]. Mathematically, is as expressed in Eq. (2):

$$C_F = \frac{\text{Measured Concentration}}{\text{Background Concentration}} \quad (2)$$

Value of Background Concentration in metal = world surface rock average [16].

Using equation 2:

For Cu,  $C_f = \frac{56.2}{32} = 1.7$

For As,  $C_f = \frac{61.9}{13} = 4.8$

The pollution grades with their corresponding intensities used in evaluating the degree of environmental contamination are provided in Table 4.

Table 4 CF Ranges [16]

$C_F$	Grade	Intensity
$C_F < 1$	I	Low contamination factor
$1 \leq C_F < 3$	II	Moderate contamination factor
$3 \leq C_F < 6$ ,	III	Considerable contamination factor
$C_F \geq 6$	IV	Very high contamination factor

Comparing the calculated CF values for Cu and As to the ranking system shown in Table 4, the following deductions can be made about the sediment quality of the Benya Lagoon. For Cu, the calculated value of 1.7 means a Grade II and an Intensity of a ‘Moderate contamination factor’. For As, the calculated value of 4.8 means a Grade III with an Intensity classification of ‘Considerable contamination factor’.

4.1.5 Potential Ecological Risk, PER Assessment

The PER factor is a diagnostic tool for lake and coastal contamination control. It is a system whose major goal is to suggest contaminating agents and where contamination research should be emphasized [9]. Three basic modules make up PER; degree of contamination ( $C_D$ ), toxic response factor ( $T_R$ ), and potential ecological risk factor ( $E_r$ ). The PER assessment system, as given in Table 5, is dependent on the abundance of the element and numerous preconditions:

- (1) Concentration – will increase with an aggravated metal pollution degree in sediments;
- (2) Species number – the metals in sediment express the additive effect, as a result, the PER is larger with the presence of multiple metals in sediment. The metals As and Cu are the objects that have previously been considered;
- (3) Toxic response – heavy metals with a high biological toxicity have more evidence for RI and magnitude for abundance correction;
- (4) Sensitivity – built on the Biological Production Index (BPI), the sensitivity is different for different water quality systems [18], [19]. The PER is mathematically expressed in Eq. (3) as:

$$E_r^i = T_r^i \times C_F^i \quad (3)$$

where,

$T_r^i$  : The metal toxic response factor for a given substance

[20]. The values for Cu and As are 5 and 10, respectively.  $C_F^i$  :

The ratio of the reference records,  $C_D^i$  and measured concentration values in sediments,  $C_R^i$  (contamination factor)

Table 6 is the PER of a given contaminant. Mathematically, the Risk Index RI, is expressed in Eq. (4) as:

$$RI = \sum E_r^i \quad (4)$$

The PER factor  $E_r$  for Cu and As are calculated as follows:

For Cu:  $E_r = 5 \times 1.7 = 8.5$

For As:  $E_r = 10 \times 4.8 = 48$ .

The calculated RI value for the lagoon sediment will therefore be:

$$RI = 8.5 + 48 = 56.5$$

Table 5 Indices and Grades of PER Factor

Critical Range for $i$ th Heavy Metal	Grade for Ecological Risk Factor
$E_r^i < 40$	Low
$40 \leq E_r^i < 80$	Moderate
$80 \leq E_r^i < 160$	Considerable
$160 \leq E_r^i < 320$	High
$E_r^i \geq 320$	Very high

Table 6 Indices and Grades of PER Index

RI Class	Critical Range for Heavy Metal	Grade for Ecological Risk Index
A	$RI < 110$	Low
B	$110 \leq RI < 220$	Moderate
C	$220 \leq RI < 440$	High
D	$RI \geq 440$	Very high

Regarding Table 5, Cu can be said to be of ‘Low-Grade Ecological risk’ as the calculated PER factor yielded  $E_r < 40$ . As yielding a calculated potential ecological risk factor  $E_r$  of 48 makes it ‘Moderate Grade Ecological factor’. The combined concentration of Copper and Arsenic in the lagoon sediment is calculated as 56.5. Comparing this value with the rankings provided in Table 6, the lagoon was found to have a ‘Low Ecological Risk index’ concerning the presence of Arsenic and Copper.

4.2 FISH (Sarotherodon melanotheron)

4.2.1 Analysis According to Dietary Recommendation

The dietary requirement for a micronutrient is an intake level that meets specified criteria for adequacy, thereby minimizing the risk of nutrient deficit or excess. The Reference Daily Intake or Recommended Daily Intake (RDI) of a nutrient is the daily intake level that is considered sufficient to meet the requirements of 97–98% of healthy individuals in every demography in the United States (where it was developed, but has since been used in other places). The RDI is based on the older Recommended Dietary Allowance (RDA) [21]. Newer RDAs have since been introduced into the Dietary Reference Intake system, but the RDI is still used for nutrition measurements.

Table 7 Cu and As Total Mean daily intake in the *S. melanotheron*

Element	Daily intake (µg/d)	Daily intake (mg/d)
As	5615.73	5.61573
Cu	7434.80	7.43480

Table 8 Recommended Dietary Allowance and Maximum Upper Limit (UL) for the various Life Stage Groups [21]

Life Stage Group	Cu		As	
	RDA (µg/d)	UL (µg/d)	RDA (mg/d)	UL (mg/d)
Infants	200	ND	ND	ND
	220	ND	ND	ND
Children	340	1,000	ND	ND
	440	3,000	ND	ND
Males	700	5,000	ND	ND
	890	8,000	ND	ND
	900	10,000	ND	ND
	900	10,000	ND	ND
	900	10,000	ND	ND
	900	10,000	ND	ND
Females	700	5,000	ND	ND
	890	8,000	ND	ND
	900	10,000	ND	ND
	900	10,000	ND	ND
	900	10,000	ND	ND
	900	10,000	ND	ND
Pregnant Women ≤	1000	8,000	ND	ND
	1000	10,000	ND	ND
	1000	10,000	ND	ND
Lactation Women	1300	8,000	ND	ND
	1300	10,000	ND	ND
	1300	10,000	ND	ND

ND = Due to a paucity of research on detrimental effects in this age group and concerns about the inability to handle excessive quantities, the answer is unknown. To avoid high amounts of intake, the only source of intake should be food. [21].

The Upper limits (ULs) of nutrient intakes have been established for several micronutrients and are defined as the maximum intake from food, water, and supplements that is unlikely to pose the risk of adverse health effects from excess in almost all (97.5%) apparently healthy individuals in an age- and sex-specific population group.

The average intake of fish is 22kg/caput/year, and therefore the average intake of fish per day is calculated as 60.274 g/d [22]. So if an average fish intake per day is represented by M (M = 60.274 g/d) and the concentration of elements in the fish be represented by N µg/g of sample. The concentration of the element in fish per day can then be given by the relation expressed in Eq. (5) as;

$$P = M \times N \tag{5}$$

P is expressed in µg/d.

The daily intake in grams per capita of the investigated elements is therefore calculated as follows:

$$P_{As} = 60.274 \text{ g/d} \times 93.17 \text{ mg/kg} = 5615.73 \text{ µg/d}$$

$$P_{Cu} = 60.274 \text{ g/d} \times 123.35 \text{ mg/kg} = 7434.80 \text{ µg/d}$$

Table 7 are the calculated value.

The calculated daily mean intake for Arsenic was 5615.73µg/d. Although there is no available data on its upper limit there is no justification for taking its supplements or adding them to food. Arsenic is a dangerous element and should not be part of food nutrients. It is poisonous and a source of anemia, gastrointestinal difficulties, despair, and even death [7], [8]. Arsenic is poisonous but up to 20 mg may regulate gene expression, backing procreative health and treating digestive hitches in the body [9].

Table 9 UL of the RDA and the calculated means differences

Life Stage Groups	Cu	As
Infants		
0-6 months	No UL	No UL
7-12 months		
Children		
1-3 y	+6434.8	No UL
4-8 y	+4434.8	
Males		
9-13 y	+2434.8	
14-18 y	-565.2	
19-30 y	-2565.2	No UL
31-50 y	-2565.2	
50-70 y	-2565.2	
>70 y	-2565.2	
Females		
9-13 y	+2434.8	
14-18 y	-565.2	
19-30 y	-2565.2	No UL
31-50 y	-2565.2	
51-70 y	-2565.2	
>70 y	-2565.2	
Pregnant Women		
≤ 18 y	-565.2	
19-30 y	-2565.2	No UL
31-50 y	-2565.2	
Lactation Women		
≤ 18 y	-565.2	
19-30 y	-2565.2	No UL
31-50 y	-2565.2	

+ denotes values above the ULs; - denotes values below the ULs.

The total mean daily intake of copper was found to be 7434.80 µg/d. This exceeds the RDA(AI) for all the various life stages and the UL of infants from 0-13 years. This means that people who consume fish from the Benya lagoon are at risk of experiencing medical conditions such as nervous system disorders and liver and kidney damage, conditions associated with the excess consumption of Copper [9], [10].

#### 4.2.2 Health Risk Estimation

Estimating the overall health effects, the Hazard Index, HI as expressed in Eq. (6), was calculated by comparing the Average

Daily Dose of each element (ED) with its Reference Dose (RfD). The reference dose is an evaluation of a daily intake amount that is unlikely to have adverse effects throughout a lifetime. The HI is determined using the calculation provided in the handbook of the United States Environmental Protection Agency [23]:

$$\text{Hazard index (HI)} = \frac{\text{ED}}{\text{RfD}} \quad (6)$$

Presented in Table 10 is the health risk associated with eating *S. Melanotheron* from the Benya Lagoon. HI < 1 suggests unlikely adverse health effects whereas HI > 1 suggests the probability of adverse health effects [23]. High HI values for the trace element examined that registered values > 1 have been emphasized for the major life stage groupings. From Table 10, except for children between 1-13 years, who recorded a health risk index >1 the rest of the life stage groups recorded a health risk index < 1 suggesting an unlikely adverse health effect for Cu for all the life stage groups. Consequently, children between 1-13 years who consume *S. Melanotheron* from the Benya Lagoon are at risk of developing health problems associated with excessive Cu intake. The health risk index associated with As was not determined as there is no available data on its UL.

Table 10 Estimated Health risk linked with the eating of *S. Melanotheron* from the Benya Lagoon

Life Stage Groups	Hazard Index	
	Cu	As
Infants		
0-6 months	ND	ND
7-12 months	ND	ND
Children		
1-3y	7.4348	ND
4-8y	2.4783	ND
Males		
9-13y	1.4867	ND
14-18y	0.9294	ND
19-30y	0.7435	ND
31-50y	0.7435	ND
50-70y	0.7435	ND
>70y	0.7435	ND
Females		
9-13y	1.48670	ND
14-18y	0.9294	ND
19-30y	0.7435	ND
31-50y	0.7435	ND
51-70y	0.7435	ND
>70y	0.7435	ND
Pregnant Women		
≤ 18y	0.9294	ND
19-30y	0.7435	ND
31-50y	0.7435	ND
Lactation Women		
≤ 18y	0.9294	ND
19-30y	0.7435	ND
31-50y	0.7435	ND

#### 4.3 Water

The Directives/Regulations listed in Table 11. are founded on the 'Environmental Quality Objective' (EQO) methodology, in which 'Environmental Quality Standards (EQSs) are laid

down for various types of water in which contaminants may be found, with concentrations more or less firmly limited. Monitoring under these directives/regulations can be used to regulate the extent to which pollutants are present in a given water sample [24].

The 'Drinking Water Directive' and Quality of Surface Water for Drinking Water Abstraction, the European Communities Regulations were signed in November 1989 and took effect the same year in December. This standard is dependable and can therefore be used to evaluate the quality of water obtained for the Benya Lagoon. The "Surface Water Regulation" is a contradiction. This is because it provides the idea that it covers surface water quality in general, whereas in fact it only covers the quality of surface water utilized as a source of drinking water for humans, as well as the appropriate treatment after abstraction. The directive deals with the so-called "raw water" [24]. The 'Drinking Water Directive' was aimed at protecting public health, and therefore heavy metals were proposed to be in much lower quantities as compared to any other regulation such as the 'Surface Water Regulation'.

Table 11 Comparison with Surface Water Regulations and Drinking Water Directives of the European Union published by the Environmental Protection Agency of the Republic of Ireland.

Element	Cu (mg/l)	As (mg/l)
Mean Concentration of metals obtained after analysis	0.080	0.120
Surface Water Regulations [1989] - I/PV value [24]	0.050	0.005
Drinking Water Directive [98/83/EC] - I/PV value [24]	0.002	0.010

Comparing the concentrations of the two investigated metals in the Benya Lagoon (0.12 mg/l for As and 0.08 mg/l for Cu) with the Surface Water Regulations and Drinking Water Directives of the European Union (shown in Table 11) it will be realized that the measured concentrations of As and Cu exceeded both standards set by the European Union. The mean concentration of Cu exceeded the Surface Water Regulation by 0.03 mg/L and the Drinking Water Directive by 0.078 mg/L while for As, its mean concentration exceeded the Surface Water Regulation by 0.115 mg/L and the Drinking Water Directive by 0.11 mg/L. These findings clearly indicate that water from the Benya lagoon is not suitable for any use; be it domestic use for washing, drinking, or cooking, or commercial purposes like irrigation for farming. It is however disturbing to mention that inhabitants within the environs of the lagoon do use water from the lagoon for all these purposes. Such inhabitants are therefore at risk of developing various health problems due to bioaccumulation of these heavy metals in their body systems over some time.

Fig. 3 and Fig. 4 depict the concentrations of Arsenic and Copper measured in the samples of sediment, water, and fish from the lagoon. It can be deduced that Cu is present in a greater amount bearing in mind the three components of the ecosystem (sediment, water, and fish) in this study and exists in higher concentrations in the fish. Arsenic, on the other hand, Arsenic exists in higher amounts in the sediments. The water sample had almost equal concentrations of Arsenic and Copper.

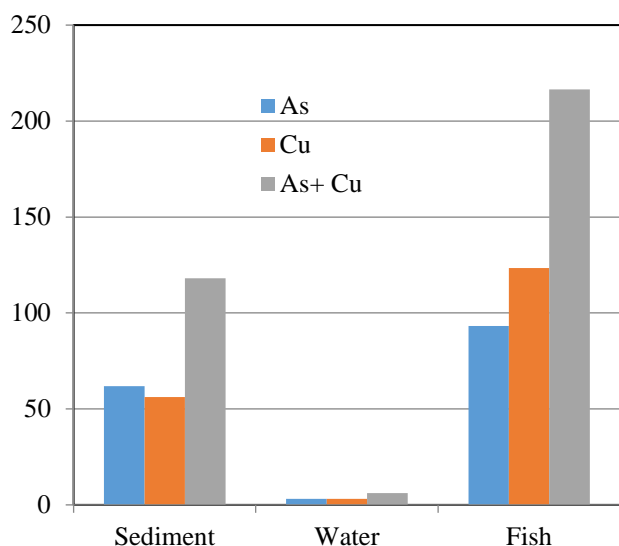


Fig. 3 Concentrations of As and Cu in sediment, water, and fish, respectively

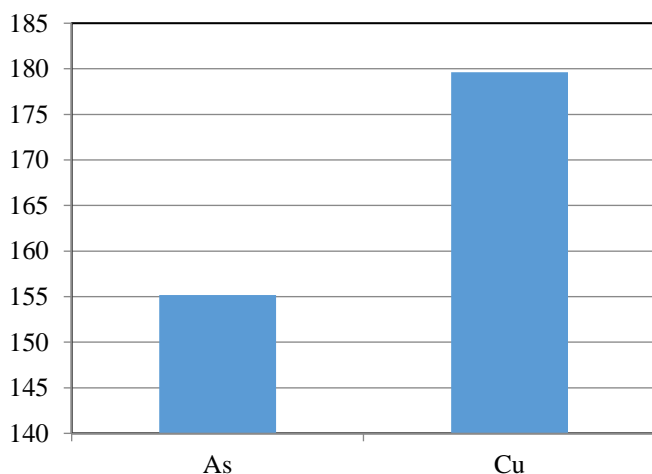


Fig. 4 As and Cu Cumulative concentrations in the three all samples

The sum of the concentrations of As and Cu present in the mediums studied decreased in the order fish > sediment > water. This is because the Benya lagoon takes its source from other water bodies and is located a few metres from the Gulf of Guinea. It is therefore not stagnant as other rivers flow into it. It is also worth mentioning that at high tides there is an influx of water from the Gulf of Guinea into the lagoon and at low tide the vice versa takes place. This process dilutes whatever concentrations there are in the lagoon. On days when there are no tides at all, the metal particles which are heavier than the other particles in the water tend to sink to the base of the lagoon to add up to the sediments, thereby increasing its metal concentration. This explains why the concentration of the heavy metals investigated was lowest in the water as compared to the measured concentrations in the sediments and fish.

In the fish, a phenomenon called bioaccumulation is responsible for the extremely high levels of metal concentrations recorded. By eating and undertaking its respiratory activities, the fish has these metals integrated into its system, with the rate at which these metals are absorbed is greater than the rate at which they are broken down. Most of the time these metals are not

biodegradable, resulting in their bioaccumulation in the fish over time. The average daily intake of Arsenic and Copper in the fish was calculated to be 5615.73  $\mu\text{g/d}$  and 7434.80  $\mu\text{g/d}$  respectively. These are values that exceed the RDA (AI) of all the various life stage groups. This indicates that *Sarotherodon melanotheron*, (Blackchin Tilapia) from the Benya Lagoon is unsafe for human consumption.

## 5 Conclusion

The collective, concentrations of Copper and Arsenic were found to have a low ecological risk index and will therefore have minimal effect on the ecological system in and around the Benya Lagoon. However, the mean concentration of Cu exceeded the Surface Water Regulation and Drinking Water Directives of the European Union by 0.03 mg/L and 0.078 mg/L respectively, while Arsenic exceeded the same standards by 0.115 mg/L and 0.11 mg/L respectively. This makes water from the Benya lagoon unsuitable for any use, be it domestic or commercial.

## 6 Acknowledgements

The writers would like to extend their heartfelt gratitude to the fishermen along the Benya Lagoon's banks. Without their assistance, this work could not have been done. We would also want to express our gratitude to the technicians and employees of the GAEC in Accra for their caring help in the samples investigation.

## References

- [1] Akoto, O., Bruce, T.N. and Darko, D., 2008. Heavy metals pollution profiles in streams serving the Owabi reservoir. *African Journal of Environmental Science and Technology*, 2(11), pp.354-359.
- [2] Reza, R. and Singh, G., 2010. Heavy metal contamination and its indexing approach for river water. *International journal of environmental science & technology*, 7(4), pp.785-792.
- [3] Gadd, G.M., Garbisu, C. and Alkotra, L., 2003. Review basic concepts on heavy metal soil bioremediation. *The European Journal of Mineral Processing and Environmental Protection*, 3, pp.58-66.
- [4] Nouri, J., Mahvi, A.H., Babaei, A. and Ahmadpour, E., 2006. Regional pattern distribution of groundwater fluoride in the Shush aquifer of Khuzestan County, Iran. *Fluoride*, 39(4), pp.321-325.
- [5] Nouri, J., Mahvi, A.H., Jahed, G.R. and Babaei, A.A., 2008. Regional distribution pattern of groundwater heavy metals resulting from agricultural activities. *Environmental Geology*, 55(6), pp.1337-1343.
- [6] Ochieng, E.Z., Lalah, J.O. and Wandiga, S.O., 2007. Analysis of heavy metals in water and surface sediment in five rift valley lakes in Kenya for assessment of recent increase in anthropogenic activities. *Bulletin of environmental contamination and toxicology*, 79(5), pp.570-576.
- [7] Parker T., 2015. Arsenic - An Essential Nutrient For Growth, Reference from <http://www.articlesnatch.com/Article/Arsenic---An-Essential-Nutrient-For-Growth/1948700>, Accessed 04/02/2015.
- [8] Arsenic And Arsenic Compounds, International Agency for Research on Cancer (IARC)- Summaries &

- Evaluations Vol. 23, pg. 39, 1980. <http://www.inchem.org/documents/iarc/vol23/arsenic.html>, Accessed 10/12/2021.
- [9] Wilson L., MD 2011. Copper toxicity syndrome, The Center For Development, Reference from [http://www.drlwilson.com/articles/copper\\_toxicity\\_syndrome.htm](http://www.drlwilson.com/articles/copper_toxicity_syndrome.htm), Accessed 10/12/2021.
- [10] Eck P., and Wilson L., 1989. Toxic Metals in Human Health and Disease, Eck Institute of Applied Nutrition and Bioenergetics, Ltd., Phoenix, AZ.
- [11] Tabari, S., Saravi, S.S.S., Bandany, G.A., Dehghan, A. and Shokrzadeh, M., 2010. Heavy metals (Zn, Pb, Cd and Cr) in fish, water and sediments sampled form Southern Caspian Sea, Iran. *Toxicology and industrial health*, 26(10), pp.649-656.
- [12] Vowotor, M.K., Odumah Hood, C., Sackey, S.S., Owusu, A., Tatchie, E., Nyarko, S., Manu Osei, D., Mireku, K.K., Letsa, C.B. and Atieomo, S.M., 2014. An assessment of heavy metal pollution in sediments of a tropical lagoon: A case study of the Benya Lagoon, Komenda Edina Eguafu Abrem Municipality (KEEA)—Ghana. *Journal of Health Pollution*, 4(6), pp.26-39.
- [13] Armah, F.A., Yawson, D.O., Pappoe, A.N. and Afrifa, E.K., 2010. Participation and sustainable management of coastal lagoon ecosystems: The case of the Fosu lagoon in Ghana. *Sustainability*, 2(1), pp.383-399.
- [14] Jones, D.S., Suter, G.W.II. and Hull, R.N., 1997. Toxicological benchmarks for screening contaminants of potential concern for effects on sediment-associated biota: 1997 revision. Oak Ridge National Lab., TN (United States).
- [15] Contaminated Sediment Standing Team., Consensus-based sediment quality guideline: recommendation for use and application. Washington D.C.: Wisconsin Department of Natural Resources; (2003), Reference from [http://dnr.wi.gov/topic/brownfields/documents/cbsqg\\_interim\\_final.pdf](http://dnr.wi.gov/topic/brownfields/documents/cbsqg_interim_final.pdf), Accessed 05/02/2015.
- [16] Martin, J.M. and Meybeck, M., 1979. Elemental mass-balance of material carried by major world rivers. *Marine chemistry*, 7(3), pp.173-206.
- [17] Duzgoren-Aydin, N.S., 2007. Sources and characteristics of lead pollution in the urban environment of Guangzhou. *Science of the Total Environment*, 385(1-3), pp.182-195.
- [18] Dumčius, A., Paliulis, D. and Kozlovskā-Kędziora, J., 2011. Selection of investigation methods for heavy metal pollution on soil and sediments of water basins and river bottoms: a review. *Ekologija*, 57(1), pp.30-38.
- [19] Liu, J., Li, Y., Zhang, B., Cao, J., Cao, Z. and Domagalski, J., 2009. Ecological risk of heavy metals in sediments of the Luan River source water. *Ecotoxicology*, 18(6), pp.748-758.
- [20] Webster, I. R. 1994. *Marine Pollution Bulletin*, 28(11), pp. 653-661.
- [21] Food and Nutrition Board, 2001. *Intake Applications in Dietary Assessment*, National Academy Press, Washington DC.
- [22] Owusu B. S., Kuwornu L. and Lomo A., (2005). Annex 5: Integrated Irrigation-Aquaculture Development and Research in Ghana. In FAO Report, Reference from <http://www.fao.org/docrep/005/y2807e/y2807e0g.htm>, Accessed 10/12/2021.
- [23] Laar, C., Fianko, J.R., Akiti, T.T., Osaе, S. and Brimah, A.K., 2011. Determination of heavy metals in the black-chin tilapia from the Sakumo Lagoon, Ghana. *Research Journal of Environmental and Earth Sciences*, 3(1), pp.8-13.
- [24] Republic of Ireland Environmental Protection Agency, *Parameters of Water Quality; Interpretation and Standards*, 2001.

# A Review of Methodological Approaches and Modeling Techniques in Service Quality Evaluation of Surface Transportation during the Last Decade

Nayeem Islam\*

Department of Civil Engineering, Bangabandhu Sheikh Mujibur Rahman Science & Technology University, Gopalganj-8100, Bangladesh

Received: October 15, 2021, Revised: December 11, 2021, Accepted: December 13, 2021, Available Online: December 18, 2021

## ABSTRACT

During the duration of the last decade, a growing interest has been noticed among transport practitioners and researchers to better understand the concept of service quality in the field of surface transportation and identify important service quality (SQ) attributes of different transportation services since these results have implications for transport managers. Due to advancements in computer technology and the availability of software packages, researchers are better able to extract meaningful results from passengers' opinions collected through stated preference surveys and communicate their findings to transport managers looking to ameliorate SQ to boost ridership on a limited budget. Since the concept of SQ is itself complex owing to the nature of the service itself compared to a tangible product and characteristics of SQ attribute, different advanced modelling techniques based on multivariate analysis, machine learning, and artificial intelligence paradigms have become popular tools among researchers. This paper aims to summarize the trends of the SQ research in the field of surface transportation during the last decade with a focus on the methodological approaches and modelling techniques and delineate future directions for research in this field.

Keywords: Service Quality, Surface Transportation, Stated Importance, Neural Networks, Decision Trees, SEM.



This work is licensed under a [Creative Commons Attribution-Non Commercial 4.0 International License](https://creativecommons.org/licenses/by-nc/4.0/).

## 1 Introduction

Traditionally, assessment of service quality (SQ) of transportation has been carried out from the point of view of transport operators and managers. Transport operators need to continuously assess the performance of their service to ensure the efficiency, effectiveness, and quality of their service. This enables the transport operators to keep attracting passengers and remain competitive in the industry. Generally, performance evaluation of transportation by transport managers considers the effectiveness and efficiency of the service in terms of cost. The inherent drawbacks of using such performance-based service quality measures are obvious. This then is the area where the interests of different stakeholders (researchers, transport practitioners, and operators) in the domain of public transportation intersect. Researchers develop models of service quality that afford transport operators and practitioners a deeper insight into the SQ paradigm.

Transport operators benefit from knowing about the SQ attributes which influence passengers when they make the holistic evaluation of SQ in several ways. It is often necessary for transport operators to make key investments decisions based on limited funds for improving SQ. It is not feasible for operators to improve different aspects of the service simultaneously. Hence operators must expand their limited funds on SQ attributes perceived by passengers as being the most important for overall transport SQ. Additionally, the ranking of the most important SQ attributes enables transport operators to formulate a plan for the staged development of the transport service.

Transport practitioners are interested in promoting public transportation as a more sustainable alternative to automobiles. The proliferation of automobiles as an affordable private mode of transportation is posing serious problems for urban mobility

by contributing to chronic congestion, air pollution and declining role of more sustainable public transportation.

However, modeling SQ in the domain of transportation is challenging for several reasons. The SQ concept is itself abstract and complex; perception heterogeneity of passengers is often a key determinant of SQ; absence of a unanimous list of SQ attributes for all types of transportation and subjective nature of the data.

Even though assessment of SQ of transportation has become a popular topic among researchers for a substantial period [1],[2], it was only during the duration of the last decade researchers employed data mining and other sophisticated mathematical models have been employed for analysing SQ of transportation due to the development and availability of different software packages. These advanced modeling approaches offer certain advantages over traditional modeling approaches. Moreover, the last decade has seen a large volume of work related to SQ assessment of surface transportation particularly the public transit industry using stated preference (SP) surveys whereas previous studies mainly focused on the aviation industry.

This then is the premise where present work is based. Therefore, the objective of this research will be to provide a concise review of the state-of-the-art procedural approaches and mathematical modeling techniques which researchers have incorporated in the realm of SQ assessment of surface transportation during the last decade. To achieve this objective, studies which have used different mathematical modeling and data mining techniques in the domain of transportation SQ were analysed based on their data collection procedure, methodological approaches, modeling procedures, presentation of results, and important inferences. An additional objective of this work is to delineate future research directions for this topic. This paper will be structured in five sections: Section 2 discusses

the concept of service quality, Section 3 furnishes some issues associated with research in this domain with respect to survey methodology, Section 4 provides a critique of the modeling techniques used by different researchers, Section 5 draws conclusions from this review and discusses future directions in this domain of research.

## 2 Concept of Service Quality

According to some researchers, the SQ concept is complex [3],[4]. This explains the application of a wide variety of methodological approaches and modeling techniques in this domain. This complexity is primarily attributed to the distinct properties of a service as compared to a product. Firstly, the output of a service cannot be measured easily like that of a product. Secondly, how an individual perceives a service is primarily a function of his/her socio-economic status, tastes, and preferences as well as expectations. Lastly, a service is first advertised, sold, and then produced and consumed simultaneously unlike a product that is produced at first, then advertised and sold before its eventual consumption.

Moreover, the following characteristics of the SQ attributes make assessments of SQ of transportation a challenging proposition for researchers:

- Number of Attributes: There is no consensus among researchers whether an exhaustive list of SQ attributes exists for the domain of transportation despite the claims of Berry of a generic list of attributes [5].
- Type of Attributes: Researchers have agreed that all SQ attributes do not have the same impact on overall SQ and therefore can be categorized into groups. According to UNE-EN 13186 standard SQ attributes can be grouped into three categories: basic, proportional, and attractive [6]. The Transit Capacity and Quality of Service Manual and Eboli & Mazzulla divide SQ attributes into two groups: ones which are basic and ones which are not basic [7],[8]. In all cases, the first category of attributes (basic) are expected by passengers as prerequisites of the service. The extent of evaluation of the latter category or categories of attributes by passengers depends on whether they are satisfied by the 'basic' attributes or not.
- Nature of SQ Attributes: Previous studies have used both qualitative [9] and quantitative attributes [10] or a mixture of both [2],[11].
- Specificity of Attributes: Researchers have concluded that attributes should be selected with regard to the context of the study. Pilot surveys focused group discussions, literature reviews, counsel with experts, academicians are utilized for drawing a list of attributes specific to the geographical location, passengers' socio-economic backgrounds, type of service, mode of transport, and mode choices available to passengers. The solution to the heterogeneity of passengers and service has been addressed by interactions between socioeconomic factors and service aspects [12] market segmentation [13]-[16], service segmentation [12] and clustering [17].
- Perspective of Assessment: As mentioned previously, most researchers agree that SQ should be measured from the point of view of passengers since a considerable difference exists between passenger perceptions and the judgment of experts [10],[18]. However, according to Thomas et al. [19] as cited by Nathanail [2] about some service aspects like safety, perception, and preference of passengers cannot be relied upon.

## 3 Survey Methodology

Different approaches may be employed to estimate the relative importance a customer attaches to each of the attributes which are related to service quality. In the stated importance methods, passengers are asked to rate each attribute on an importance scale. On the other hand, derived importance methods statistically analyse the relationship of individual attributes with overall satisfaction to derive the importance of each attribute. The stated importance method is simpler and more intuitive of the two methods but is not without some drawbacks. Often the length of stated importance surveys can limit the response rate and many passengers are unable to discriminate between the importance of different attributes which impact overall service quality. Thus, researchers using data mining techniques have often preferred derived importance methods based on stated preference surveys since data mining techniques are able to generate a ranking of the most important explanatory variables for each developed model.

Therefore, the most widely used method for measuring service quality of transportation involves asking the users to rate different aspects of the used service in a questionnaire survey called customer satisfaction surveys (CSS). In different studies, users of the transport service were provided with questionnaires where passengers generally expressed their perceptions of performance on a Likert scale, identified or rated the most important SQ attributes among the SQ attributes given in the survey, and were often asked to rate overall transportation SQ on a Likert scale. Different numeric Likert scales (0-10; 1-10; 1-5; 1-6, 1-7, 1-9, -2 to +2) are found in the literature which is often complemented by linguistic/qualitative scales for ease of understanding by passengers and there is no consensus among researchers with regard to the format of the numeric or semantic Likert scale which would make the survey more effective and inclusive. Machado-León et al. used different numeric Likert scales for different sections of the same questionnaire, so passengers are able to better differentiate between attribute scores [20]. For example, de Oña et al. used a three-point semantic scale (poor, fair, and good) for obtaining passengers' perception of performance and used a numeric 10 point scale for collecting information about the importance of SQ attributes [21]. Other studies asked passengers to select the attributes they considered as important sparing them from the tedious routine of having to rate all the SQ attributes individually [16],[22]-[26]. Moreover, researchers using decision trees reduced the dependent and explanatory variables in a semantic scale (POOR, FAIR, and GOOD) for ease of modeling [13],[15].

### 3.1 Sample Size

Sample size used in previous studies varied widely from one study to another. Pakdil & Kurtulmuşoğlu [27], Kurtulmuşoğlu et al. [28] used the sampling approach recommended by De Vaus [29] to compute sample size. Deb & Ahmed [9] computed the minimum sample size based on the equation proposed by Johnson & Wichern [30]. In order to ensure the results of the sample population can be used to draw conclusions about public transit users, Mahmoud & Hine [31] used the guidelines of Bartlett et al. [32]. Jomnonkwao & Ratanavaraha [33] used the guidelines of Stevens [34] who set the minimum number of samples to be at least 15 times the number of observed variables if maximum likelihood estimation is used. Some studies [14],[35] sampled 3-4% of the population. The sample size used in different studies are recorded in Table 1.

Table 1 Summary of Research in Surface Transportation during Last Decade

References	Industry	Country	Region	Valid Surveys	Scale Used	Type of Scale	Modeling
Bordagaray et al. [12]	Bus Transit	Spain	Santander	266	1-5	Likert Scale	Ordered probit models
Cheng et al. [41]	Bus Transit	China	Xianbei	291	1-5	Likert Scale	SEM
Deb & Ahmed [9]	Bus Transit	India	Agartala	400	1-9	Likert Scale	SEM
Pakdil & Kurtulmuşoğlu [27]	Intercity Bus	Europe	Not mentioned	500	1-5	Likert Scale	QFD
Kurtulmuşoğlu et al. [28]	Intercity Bus	Not mentioned	Not mentioned	285	5 Layer	Triangular Fuzzy Number	Fuzzy QFD
Jen et al. [43]	Intercity Bus	Taiwan	Taipei	747	1-5	Likert Scale	SEM
Jomnonkwao and Ratanavaraha [33]	Sight seeing bus	Thailand	N.A.	3387	1-7	Likert Scale	SEM
Mahmoud & Hine [31]	Bus Transit	UK	Belfast	512	1-10	Likert Scale	Binary logistic regression
Rojo et al. [46]	Intercity Bus	Spain	N.A.	1011	1-5	Likert Scale	Ordered Logit and probit model
Rojo et al. [48]	Intercity Bus	Spain	Castilla y León	375	N.A.	SP Experiment	Multinomial, hierarchial and mixed logit models
Chou et al. [38]	High Speed Rail	Taiwan	N.A.	1235	1-7	Likert Scale	SEM
de Oña et al. [21]	Bus transit	Spain	Granada	858	Not mentioned	Not mentioned	Decision Tree
de Oña & de Oña [15]	Bus transit	Spain	Granada	3182	0-10	Likert Scale	Decision Tree
de Oña & de Oña [26]	Bus transit	Spain	Granada	3664	0-10	Likert Scale	Decision Tree
de Oña et al. [35]	Rail Transit	Italy	Milan	16647	1-10	Likert Scale	Decision Tree
de Oña et al. [14]	Rail transit	Italy	Milan	7333	1-10	Likert Scale	Decision Tree
de Oña et al. [17]	Bus transit	Spain	Granada	3664	0-10, 1-5	Likert Scale	Decision Tree
Machado-León et al. [20]	Rail Transit	Algiers	Algeria	1454	0-10, 1-5	Likert Scale	Importance-Performance Analysis and Decision Tree
de Oña et al. [36]	Bus transit	Spain	Granada	858	0-10	Likert Scale	Decision Tree and ANN
Garrido et al. [37]	Bus transit	Spain	Granada	858	0-10	Likert Scale	ANN
Hadiuzzaman et al. [16]	Intercity train	Bangladesh	N.A.	1037	1-5	Likert Scale	SEM
Hadiuzzaman et al. [22]	Intercity train	Bangladesh	N.A.	1590	1-5	Likert Scale	ANFIS
Hadiuzzaman et al. [23]	Bus transit	Bangladesh	Dhaka	655	1-5	Likert Scale	SEM
Islam et al. [24]	Bus transit	Bangladesh	Dhaka	655	1-5	Likert Scale	PNN and ANFIS
Islam et al. [25]	Bus transit	Bangladesh	Dhaka	655	1-5	Likert Scale	GRNN, PNN and PRNN
Machado-León et al. [40]	Light Rail Transit	Spain	Seville	3211	0-10, 1-5	Likert Scale	SEM
Yilmaz & Ari [39]	Inter-city high speed rail	Turkey	N.A.	352	1-5	Likert Scale	SEM
Joewono et al. [44]	Road based public transport	Indonesia	Different cities	1482	1-5	Likert Scale	SEM
Nwachukwu [45]	Bus transit	Nigeria	Abuja	300	1-5	Likert Scale	Principal Component Analysis
Hu et al. [42]	Bus transit	China	Nanjing	958	1-5	Likert Scale	SEM and multinomial logit model

Note. N.A. : Not Applicable

## 4 Modeling Techniques

de Oña & de Oña classified methodological approaches in measuring SQ into two categories: (i) disaggregated models and (ii) aggregated models [13]. In the disaggregated model the SQ attributes are analyzed individually but in aggregated models, SQ attributes are combined to obtain a service quality index. While aggregated models offer the advantage that it can be used to compare different transportation services, aggregated models shortlist the significant SQ attributes for the transport manager on a limited budget to improve upon. Consequently, disaggregated models have been preferred by researchers in the last decade, the time period of interest in this review paper. Among the different statistical and machine learning techniques the following have been mostly used by researchers: decision trees (DT), neural networks, structured equation modeling (SEM) and factor analysis, and different types of logit models. Quality Function Deployment (QFD) and Fuzzy QFD have only been introduced by Pakdil & Kurtulmusoglu and Kurtulmuşoğlu et al. respectively [27]-[28].

### 4.1 Decision Trees

Before being applied in the domain of SQ studies, decision trees were applied to both regression and classification problems in traffic engineering. Decision trees divide the predictor space into a number of simple regions. Prediction for a new observation is made by taking into account the mean or mode of the training observations in the region where the new observation belongs. A classification tree is utilized when the value of the target variable is discrete whereas a regression tree is utilized when the value of the target variable is continuous. The main benefit offered by decision trees is that there are no underlying assumptions between independent and dependent variables. The visualization of a decision tree model is also easy to understand and interpret. This is an important feature of decision trees since transport managers are generally non-technical people and can understand the models easily. Moreover, useful decision rules can be extracted from the models. A decision rule is created by following a path from the root node to the terminal node of a decision tree model. Decision trees can handle many both numerical and categorical variables as well as a large number of explanatory variables without normalization. The standardized importance of attributes can also be extracted from decision trees.

However, decision tree models are not typically robust, have lower accuracy rates, do not offer backtracking techniques, or provide statistical significance of variables [36]. Moreover, studies using decision trees have not specifically mentioned the algorithms used [13],[21].

### 4.2 Neural Networks

Neural networks are models which process information closely mimicking the process in the human brain. It is capable of supervised learning even when noise is present. The neural network is composed of neurons which are primary information processing units. These neurons are organized into several layers and connected to each other through synaptic weights which represent the strength of interaction between each pair of neurons. Activation functions calculate the potential of each neuron. Different types of neural networks exist: Artificial Neural Networks (ANN), Generalized Regression Neural Network (GRNN), Probabilistic Neural Network (PNN), and Pattern Recognition Neural Network (PRNN), Adaptive Neuro Fuzzy Inference System (ANFIS).

A number of advantages of using neural networks have been reported by researchers higher precision, more stability for determining attribute importance, capability for handling multicollinearity [36]-[37]. The main drawback of using neural networks reported is mainly related to the time necessary to train and the cumbersome routine needed to determine variable importance.

The different types of neural networks employed in SQ studies and often compared to each other or other techniques include ANN [37], comparison between ANN and DT [36] comparison between ANFIS and PNN [24], comparison between PNN, PRNN, and GRNN [25] and ANFIS [22].

### 4.3 SEM and Factor Analysis

SEM is an integration of measurement theory, factor analysis, multiple regression, simultaneous equations, and path analysis. It has gained prominence among researchers in the domain of SQ studies primarily because it is able to identify which observed variables are good indicators of the latent variables. SEM consists of measurement and structural models. The task of the measurement model also called confirmatory factor analysis is to determine the correlation between observed variables and latent variables. The structural model is used to determine the strength and direction of relations between latent variables.

SEM has been applied to different transportation services: high-speed rail [38]-[39], light rail transit [40], train service in developing countries [24], bus transit [9],[41]-[42], intercity bus [43] and combination of different types of urban public transport [44].

In addition factor analysis which is normally used as a preparatory step for SEM was applied separately as a modeling technique for different SQ studies in sightseeing bus service [33] and city bus service [45].

### 4.4 Logit Models

Discrete choice models explain how passengers choose between different alternatives. However, to fit within the model framework, the choice set needs to demonstrate three characteristics:

- only one alternative can be chosen by passengers.
- list of alternatives in the choice set needs to be exhaustive.
- there needs to be a finite number of alternatives available to passengers.

Generally stated preference surveys in the field of SQ assessment of transportation provide passengers with choices which are ordered: 'very satisfied' is better than 'satisfied' and the choices are not necessarily independent of one another. Hence ordered logit and probit models are therefore more suited to stated preference experiment data of this type and have been applied in SQ studies in inter-city bus service [46]-[47], bus transit [12]. Other forms of logit model that have been used are multinomial logit models for city bus service [48] and multinomial, hierarchical and mixed logit models for inter-city bus service [48]. These models have been used for determining the weight of different service aspects.

### 4.5 QFD and Fuzzy QFD

QFD is a process which attempts to capture the needs of the customers and respond to those needs through specific plans for improving the product or service in question. The customer requirements are translated to measurable design targets using

QFD. A unique feature of the QFD process is that it also utilizes transport operators' technical knowledge besides passengers' perceptions [27]. QFD process flows through six distinct phases which are interconnected within a House of Quality (HOQ) diagram: (1) customer needs and expectations, (2) planning matrix, (3) technical requirements, (4) relationship matrix, (5) technical correlation matrix, and (6) customer evaluations. However, since QFD was originally adapted to manufacturing industries, and SQ by nature is abstract and fuzzy, fuzzy set theory was employed by Kurtulmuşoğlu et al. to improve the planning matrix, relationship matrix, and technical correlation matrix [28].

## 5 Discussion and Future Research Directions

Despite the large volume of work already accomplished in the last decade, there is considerable work to be done in the domain of SQ of surface transportation services. For example, a careful view of Table 1 reveals that very few studies have focused on inter-city transportation services. Moreover, very few studies actually compare the efficacy of different modeling techniques in order to find the optimum model in the domain of SQ studies [24]-[25],[36]. Also, it is noticeable that despite the use of machine learning models like decision trees in different SQ studies, researchers are yet to use any ensemble models like Random Forests or more fine-tuned applications of decision trees like gradient boosted decision tree models. The different attempts by researchers in developing countries to evaluate the service quality of public transportation are commendable but still, the volume of research coming from developing countries is considerably low. Also, researchers need to find out how they can collect greater volumes of data using online surveys making research results more meaningful.

In this paper, an attempt has been made to capture the contemporary thinking and modeling techniques used by researchers to evaluate the service quality of surface transportation services in the last decade. This paper also tried to focus on the algorithms that have gained popularity among researchers due to the advancement made in computer technology and the widespread availability of several powerful software packages. Finally, it is expected that the insight provided by this paper will be useful to all stakeholders in the domain of transportation services and researchers will contemplate the future directions proposed in this paper.

## 6 Conclusions

The preceding discussion shows that a plethora of attempts and modeling methodologies have been used by researchers to better understand the SQ paradigm convey useful information for transport managers to work on. The variety of attempts point towards the complexity of the SQ concept and the wealth of modeling techniques that are available to the researchers.

However, some trends have become evident in the last decade in SQ studies. Firstly, researchers have preferred the stated preference surveys to collect satisfaction/ perception and importance rating of different SQ attributes from passengers using numerical Likert scales. Secondly, researchers are increasingly using multivariate analysis techniques like SEM, machine learning, and artificial intelligence-based paradigms like neural networks and decision trees and ordered choice models. These models are enabling researchers, transport managers deeper insight into the SQ paradigm than simpler regression models. It is also possible to deduce the importance of independent variables from these models since it has been shown

that asking passengers to rate the importance of SQ attributes often produces unrealistic results [35],[50]. Thirdly, researchers are taking into account the perception heterogeneity of the SQ data and introducing different innovative techniques like clustering which can help transport managers to introduce personalized market in surface transportation services like in the aviation industry.

## References

- [1] Cavana, R. Y., Corbett, L. M., & Lo, Y. G., 2007. Developing zones of tolerance for managing passenger rail service quality. *International Journal of Quality & Reliability Management*, 24(1), pp.7-31.
- [2] Nathanail, E., 2008. Measuring the quality of service for passengers on the Hellenic railways. *Transportation Research Part A: Policy and Practice*, 42(1), pp.48-66.
- [3] Carman, J.M., 1990. Consumer perceptions of service quality: an assessment of T. *Journal of Retailing*, 66(1), p.33.
- [4] Parasuraman, A., Zeithaml, V.A. and Berry, L.L., 1985. A conceptual model of service quality and its implications for future research. *Journal of Marketing*, 49(4), pp.41-50.
- [5] Parasuraman, A., Zeithaml, V.A. and Berry, L., 1988. SERVQUAL: A multiple-item scale for measuring consumer perceptions of service quality. *Journal of Retailing*, 64(1), pp.12-40.
- [6] UNE-EN 13816, 2003. Transportation. Logistics and Services. Public Passenger Transport. Service Quality Definition, Targeting and Measurement, AENOR, Madrid.
- [7] Kittelson & Associates, United States. Federal Transit Administration, Transit Cooperative Research Program and Transit Development Corporation, 2003. *Transit capacity and quality of service manual* (Vol. 42). Transportation Research Board.
- [8] Eboli, L. and Mazzulla, G., 2008. Willingness-to-pay of public transport users for improvement in service quality. *European Transport \ Trasporti Europei*, 38, pp.107-118.
- [9] Deb, S. and Ahmed, M.A., 2018. Determining the service quality of the city bus service based on users' perceptions and expectations. *Travel Behaviour and Society*, 12, pp.1-10.
- [10] Das, S. and Pandit, D., 2015. Determination of level-of-service scale values for quantitative bus transit service attributes based on user perception. *Transportmetrica A: Transport Science*, 11(1), pp.1-21.
- [11] Basu, D. and Hunt, J.D., 2012. Valuing of attributes influencing the attractiveness of suburban train service in Mumbai city: A stated preference approach. *Transportation Research Part A: Policy and Practice*, 46(9), pp.1465-1476.
- [12] Bordagaray, M., dell'Olio, L., Ibeas, A. and Cecín, P., 2014. Modelling user perception of bus transit quality considering user and service heterogeneity. *Transportmetrica A: Transport Science*, 10(8), pp.705-721.
- [13] de Oña, R. and de Oña, J., 2015. Analysis of transit quality of service through segmentation and classification tree techniques. *Transportmetrica A: Transport Science*, 11(5), pp.365-387.
- [14] De Oña, J., de Oña, R., Eboli, L. and Mazzulla, G., 2015. Heterogeneity in perceptions of service quality among groups of railway passengers. *International Journal of Sustainable Transportation*, 9(8), pp.612-626.
- [15] De Oña, R. and De Oña, J., 2013. Analyzing transit service quality evolution using decision trees and gender segmentation. *WIT transactions on the built environment*, 130, pp.611-621.
- [16] Hadiuzzaman, M., Farazi, N.P., Hossain, S. and Malik, D.G., 2019. An exploratory analysis of observed and latent variables affecting intercity train service quality in developing countries. *Transportation*, 46(4), pp.1447-1466.
- [17] de Oña, J., de Oña, R. and López, G., 2016. Transit service quality analysis using cluster analysis and decision trees: a step

- forward to personalized marketing in public transportation. *Transportation*, 43(5), pp.725-747.
- [18] Das, S. and Pandit, D., 2012. Methodology to identify the gaps in the level of service provided for urban bus transit: Case study Kolkata. *Spandrel*, 4(Spring), pp.59-71.
- [19] Thomas, L.J., Rhind, D.J. and Robinson, K.J., 2006. Rail passenger perceptions of risk and safety and priorities for improvement. *Cognition, Technology & Work*, 8(1), pp.67-75.
- [20] Machado-León, J.L., de Oña, R., Baouni, T. and de Oña, J., 2017. Railway transit services in Algiers: priority improvement actions based on users perceptions. *Transport Policy*, 53, pp.175-185.
- [21] De Oña, J., De Oña, R. and Calvo, F.J., 2012. A classification tree approach to identify key factors of transit service quality. *Expert Systems with Applications*, 39(12), pp.11164-11171.
- [22] Hadiuzzaman, M., Malik, D.G., Barua, S., Qiu, T.Z. and Kim, A., 2019. Modeling passengers' perceptions of intercity train service quality for regular and special days. *Public Transport*, 11(3), pp.549-576.
- [23] Hadiuzzaman, M., Das, T., Hasnat, M.M., Hossain, S. and Rafee Musabbir, S., 2017. Structural equation modeling of user satisfaction of bus transit service quality based on stated preferences and latent variables. *Transportation Planning and Technology*, 40(3), pp.257-277.
- [24] Islam, R., Musabbir, S.R., Ahmed, I.U., Hadiuzzaman, M., Hasnat, M. and Hossain, S., 2016. Bus service quality prediction and attribute ranking using probabilistic neural network and adaptive neuro fuzzy inference system. *Canadian Journal of Civil Engineering*, 43(9), pp.822-829.
- [25] Islam, M.R., Hadiuzzaman, M., Banik, R., Hasnat, M.M., Musabbir, S.R. and Hossain, S., 2016. Bus service quality prediction and attribute ranking: a neural network approach. *Public transport*, 8(2), pp.295-313.
- [26] De Oña, J. and De Oña, R., 2015. Quality of service in public transport based on customer satisfaction surveys: A review and assessment of methodological approaches. *Transportation Science*, 49(3), pp.605-622.
- [27] Pakdil, F. and Kurtulmusoglu, F.B., 2014. Improving service quality in highway passenger transportation: a case study using quality function deployment. *EJTIR*, 14(4), pp.375-393.
- [28] Kurtulmuşoğlu, F.B., Pakdil, F. and Atalay, K.D., 2016. Quality improvement strategies of highway bus service based on a fuzzy quality function deployment approach. *Transportmetrica A: Transport Science*, 12(2), pp.175-202.
- [29] De Vaus, D., & de Vaus, D. (2013). *Surveys In Social Research* (6th ed.). Routledge.
- [30] Johnson, R.A. and Wichern, D.W., 2014. *Applied multivariate statistical analysis* (Vol. 6). London, UK:: Pearson.
- [31] Mahmoud, M. and Hine, J., 2016. Measuring the influence of bus service quality on the perception of users. *Transportation Planning and Technology*, 39(3), pp.284-299.
- [32] Kotrlík, J.W.K.J.W. and Higgins, C.C.H.C.C., 2001. Organizational research: Determining appropriate sample size in survey research appropriate sample size in survey research. *Information Technology, Learning, and Performance Journal*, 19(1), p.43-50.
- [33] Jomnonkwo, S. and Ratanavaraha, V., 2016. Measurement modelling of the perceived service quality of a sightseeing bus service: An application of hierarchical confirmatory factor analysis. *Transport Policy*, 45, pp.240-252.
- [34] Stevens, J., 1966. *Applied Multivariate Statistics for the Social Sciences*. Lawrence Erlbaum Associates, NJ.
- [35] De Oña, R., Eboli, L. and Mazzulla, G., 2014. Key factors affecting rail service quality in the Northern Italy: a decision tree approach. *Transport*, 29(1), pp.75-83.
- [36] de Oña, J., de Oña, R. and Garrido, C., 2017. Extraction of attribute importance from satisfaction surveys with data mining techniques: a comparison between neural networks and decision trees. *Transportation Letters*, 9(1), pp.39-48.
- [37] Garrido, C., De Oña, R. and De Oña, J., 2014. Neural networks for analyzing service quality in public transportation. *Expert Systems with Applications*, 41(15), pp.6830-6838.
- [38] Chou, P.F., Lu, C.S. and Chang, Y.H., 2014. Effects of service quality and customer satisfaction on customer loyalty in high-speed rail services in Taiwan. *Transportmetrica A: Transport Science*, 10(10), pp.917-945.
- [39] Yilmaz, V. and Ari, E., 2017. The effects of service quality, image, and customer satisfaction on customer complaints and loyalty in high-speed rail service in Turkey: a proposal of the structural equation model. *Transportmetrica A: Transport Science*, 13(1), pp.67-90.
- [40] Machado-León, J.L., de Oña, R. and de Oña, J., 2016. The role of involvement in regards to public transit riders' perceptions of the service. *Transport Policy*, 48, pp.34-44.
- [41] Cheng, X., Cao, Y., Huang, K. and Wang, Y., 2018. Modeling the satisfaction of bus traffic transfer service quality at a high-speed railway station. *Journal of Advanced Transportation*, 2018.
- [42] Hu, X., Zhao, L. and Wang, W., 2015. Impact of perceptions of service performance on mode choice preference. *Advances in Mechanical Engineering*, 7(3), p.1687814015573826.
- [43] Jen, W., Tu, R. and Lu, T., 2011. Managing passenger behavioral intention: an integrated framework for service quality, satisfaction, perceived value, and switching barriers. *Transportation*, 38(2), pp.321-342.
- [44] Joewono, T.B., Tarigan, A.K. and Susilo, Y.O., 2016. Road-based public transportation in urban areas of Indonesia: what policies do users expect to improve the service quality?. *Transport policy*, 49, pp.114-124.
- [45] Nwachukwu, A.A., 2014. Assessment of passenger satisfaction with intra-city public bus transport services in Abuja, Nigeria. *Journal of Public Transportation*, 17(1), pp.99-119.
- [46] Rojo, M., Gonzalo-Orden, H., dell'Olio, L. and Ibeas, A., 2011, February. Modelling gender perception of quality in interurban bus services. In *Proceedings of the Institution of Civil Engineers-Transport* (Vol. 164, No. 1, pp. 43-53). Thomas Telford Ltd.
- [47] Rojo, M., dell'Olio, L., Gonzalo-Orden, H. and Ibeas, Á., 2013. Interurban bus service quality from the users' viewpoint. *Transportation Planning and Technology*, 36(7), pp.599-616.
- [48] Dell'Olio, L., Ibeas, A. and Cecin, P., 2011. The quality of service desired by public transport users. *Transport Policy*, 18(1), pp.217-227.
- [49] Rojo, M., Gonzalo-Orden, H., dell'Olio, L. and Ibeas, Á., 2012. Relationship between service quality and demand for inter-urban buses. *Transportation Research Part A: Policy and Practice*, 46(10), pp.1716-1729.
- [50] Weinstein, A., 2000. Customer satisfaction among transit riders: How customers rank the relative importance of various service attributes. *Transportation Research Record*, 1735(1), pp.123-132.

# The Periodicity of the Accuracy of Numerical Integration Methods for the Solution of Different Engineering Problems

Toukir Ahmed Chowdhury, Towhedul Islam, Ahmad Abdullah Mujahid, and Md. Bayazid Ahmed

Department of Mechanical Engineering, Chittagong University of Engineering & Technology, Chattogram-4349, Bangladesh

Received: October 05, 2021, Revised: November 30, 2021, Accepted: November 30, 2021, Available Online: December 23, 2021

## ABSTRACT

Newton-Cotes integration formulae have been researched for a long time, but the topic is still of interest since the correctness of the techniques has not yet been explicitly defined in a sequence for diverse engineering situations. The purpose of this paper is to give the readers an overview of the four numerical integration methods derived from Newton-Cotes formula, namely the Trapezoidal rule, Simpson's 1/3rd rule, Simpson's 3/8th rule, and Weddle's rule, as well as to demonstrate the periodicity of the most accurate methods for solving each engineering integral equation by varying the number of sub-divisions. The exact expressions by solving the numerical integral equations have been determined by Maple program and comparisons have been done using Python version 3.8.

Keywords: Numerical Integration Accuracy, Trapezoidal Rule, Simpson's 1/3 Rule, Simpson's 3/8 Rule, Weddle's Rule.



This work is licensed under a [Creative Commons Attribution-Non Commercial 4.0 International License](https://creativecommons.org/licenses/by-nc/4.0/).

## 1 Introduction

Throughout the entire history of mathematical research, integration is undoubtedly one of the most important mathematical concepts ever conceived. An integral is a mathematical term that defines displacement, area, volume, and other ideas that result from the combination of infinitesimal data. The process of determining integrals is known as integration.

Numerical integration is the process of estimating the value of a definite integral from the estimated numerical values of the integrand. If the numerical integration is performed on a single variable, it is called Quadrature, while for multiple variables, it is called Cubature. Scientists and engineers mostly utilize numerical integration to get an approximate solution for definite integrals that cannot be solved analytically. The reasons for which numerical integration is preferred over analytical are:

- Although there is a closed form solution, calculating the answer numerically can be difficult.
- The integrand  $f(x)$  may only be known at a few locations, as determined through sampling.
- Many integrals are not analytically evaluable or have no closed form solution. e.g.  $\int_0^t e^{-2x^3} dx$
- Although the integrand  $f(x)$  is not explicitly known, a collection of data points for this integrand is provided.

The term 'Numerical Integration' was first coined in 1915 in the booklet named *A Course in Interpolation and Numeric Integration for the Mathematical Laboratory* by David Gibb.

Many academic areas, including applied mathematics, geometry, finance, statistics, economics, and engineering, use numerical integration methods. The available numerical integration methods include Quadrature methods, Gaussian integration, Monte-Carlo integration, Adaptive Quadrature, and the Euler-Maclaurin formula, which are used to compute complex functions. The Newton-Cotes formulas are also acknowledged as the Newton-Cotes quadrature standards or truly Newton-Cotes laws. These are the numerical integration implementation techniques (also regarded as quadrature),

especially focused on measuring the integrand at equally spaced numerical analysis factors. The methods are named after Isaac Newton and Roger Cotes. There are two forms of the method for Newton-Cotes; Open Newton-Cotes and Closed Newton-Cotes. Trapezoidal rule, Simpson 1/3 rule, Simpson 3/8 rule, Weddle's rule and Boole's rule originate from the closed Newton-Cotes formula. On the other hand, Midpoint law, Trapezoid process, Milne's rule is derived from the formula of open Newton-Cotes.

The different numerical integration equations are covered in works by S.S. Sastry [1]-[2], R.L. Burden [3]-[4], J.H. Mathews [5]-[6], and others. M. Concepcion Austin [4] was helpful in evaluating different numerical integration producers and addressing more sophisticated numerical integration techniques. Gordon K. Smith [5] made contributions to this discipline through his analytic study of numerical integration and a collection of 33 papers and books on the subject. Rajesh Kumar Sinha [6] attempted to evaluate an integrable polynomial without using the Taylor Series. Gerry Sozio [7] examined a comprehensive overview of different numerical integration methods. J.Oliver [8] explored the multiple evaluation procedures of definite integrals using higher-order formulas. A. Nataranjan and N. Mohankumar [9] compared several quadrature methods for approximating Cauchy principal value integrals. D.J. Liu, J.M. Wu, and D.H. Yu [10] explored the super convergence of the Newton-Cotes rule for Cauchy principal value integrals. Romesh Kumar Muthumalai [11] attempted to calculate the inaccuracy of numerical integration and differentiation, and he also developed several formulas for numerical differentiation by divided difference. Md. Mamun-Ur-Rashid Khan [12] devised a novel technique to numerical integration strategies for uneven data space.

In the realm of applied mathematics, numerical integration has a wide range of applications, particularly in mathematical physics and computational chemistry [13]. It is also employed in population estimation [14], medical picture reconstruction [15], and physics [16]. Chapra SC showed in Applied Numerical Methods with MATLAB [17] the application of numerical methods to solve problems in engineering and science.

Previously, many mathematical softwares like Mathcad [18], Matlab [19], Fortran, C, C++ [20]-[21], and Mathematica [22] have been used to solve integrals numerically. Caligaris et.al [22] had designed a tool which performs numerical integration in Mathematica by four methods namely Trapezoidal, Simpson’s 1/3, Simpson’s 3/8, and Gauss Quadrature with various points. In this paper, the use of numerical integration in different engineering applications has been focused on. Instead of using the other previously used languages, we used Python 3.8 to solve different integral equations. From the graphs and the values of individual problems, it is seen that with the change of interval, the most accurate method changes and there is an interesting pattern of accuracy that is followed in each engineering problem.

**2 Mathematical Model**

**2.1 Newton-Cotes formula**

Newton’s forward difference formula for equally spaced intervals is given by

$$y(x) = y_0 + u \Delta y_0 + \frac{u(u-1)}{2!} \Delta^2 y_0 + \frac{u(u-1)(u-2)}{3!} \Delta^3 y_0 + \dots$$

Here,  $u = \frac{x-x_0}{h}$ ,  $x = x_0 + uh$ ,  $dx = hdu$

$$\int_{x_0}^{x_n} y dx = \int_{x_0}^{x_0+nh} f(x) dx = \int_0^n (y_0 + u \Delta y_0 + \frac{u(u-1)}{2!} \Delta^2 y_0 + \frac{u(u-1)(u-2)}{3!} \Delta^3 y_0 + \dots) hdu = h \int_0^n (y_0 + u \Delta y_0 + \frac{u(u-1)}{2!} \Delta^2 y_0 + \frac{u(u-1)(u-2)}{3!} \Delta^3 y_0 + \dots) du = h [ ny_0 + \frac{n^2}{2} \Delta y_0 + \frac{1}{2} (\frac{n^3}{3} - \frac{n^2}{2}) \Delta^2 y_0 + \dots ]$$

This is the required Newton-Cotes Quadrature formula.

By putting n = 1 in the Quadrature formula, we get the Trapezoidal rule,

$$\int_{x_0}^{x_n} y dx = \frac{h}{2} [(y_0 + y_n) + 2 (y_1 + y_2 + y_3 + \dots + y_{n-1})]$$

By putting n = 2 in the Quadrature formula, we get the Simpson’s  $\frac{1}{3}$  rule,

$$\int_{x_0}^{x_n} y dx = \frac{h}{3} [(y_0 + y_n) + 2 (y_2 + y_4 + \dots + y_{2n}) + 4 (y_1 + y_3 + \dots)]$$

By putting n = 3 in the Quadrature formula, we get the Simpson’s  $\frac{3}{8}$  rule,

$$\int_{x_0}^{x_n} y dx = \frac{3h}{8} [(y_0 + y_n) + 3 (y_1 + y_2 + y_4 + y_5 + \dots) + 2 (y_3 + y_6 + \dots)]$$

By putting n = 6 in the Quadrature formula, we get the Weddle’s rule,

$$\int_{x_0}^{x_n} y dx = \frac{3h}{10} [(y_0 + y_n) + 5 (y_1 + y_7 + y_{13} + \dots) + (y_2 + y_8 + y_{14} + \dots) + 6 (y_3 + y_9 + y_{15} + \dots) + (y_4 + y_{10} + y_{16} + \dots) + 5 (y_5 + y_{11} + y_{17} + \dots)]$$

**3 Different Engineering Problems & Their Applications**

**3.1 Spring**

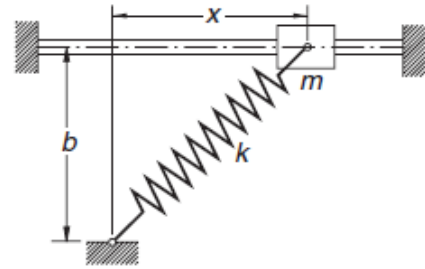


Fig. 1 Spring [23].

“The mass  $m$  is attached to a spring (see ) of free length  $b$  and stiffness  $k$ . The coefficient of friction between the mass and the horizontal rod is  $\mu$ . The acceleration of the mass can be shown to be  $a = -f(x)$ , where

$$f(x) = \mu g + \frac{k}{m} (\mu b + x) (1 - \frac{b}{\sqrt{b^2+x^2}})$$

If the mass is released from rest at  $x = b$ , its speed at  $x = 0$  is given by

$$v_0 = \sqrt{2 \int_0^b f(x) dx}$$

Compute  $v_0$  by using the data  $m = 0.8$  kg,  $b = 0.4$  m,  $\mu = 0.3$ ,  $k = 80$  N/m and  $g = 9.81$  m/s<sup>2</sup> [23].”

**3.1.1 Actual Solution**

When  $x = 0$ , the speed of the mass  $m$  will be

$$v_0 = \sqrt{2 \int_0^{0.4} f(x) dx} = \sqrt{2 \int_0^{0.4} (\mu g + \frac{k}{m} (\mu b + x) (1 - \frac{b}{\sqrt{b^2+x^2}}) dx} = \sqrt{2 \left[ \frac{x(50000x+14943)-4800 \ln|\sqrt{25x^2+4} + 5x|}{1000} + 8\sqrt{25x^2+4} \right]_0^{0.4}} = 2.49767483245384 \text{ m/s}$$

**3.1.2 Engineering Application**

The described problem and its solution can be used for controlling forces and movement in brakes and clutch systems, for minimizing shocks and vibrations in the suspension system of a car, energy conservation in the case of toys and watches, etc.

**3.2 Capacitor**

“A capacitor in an electrical circuit is initially at zero charge. At time  $t$  of 1 s, a switch is closed, and a time-dependent electric current  $I(t)$  charges up the capacitor. The current is given as

$$I(t) = 4 (1 - e^{-0.5}) e^{-0.5(t-1)} (1 - e^{-t}).$$

Compute the charge  $Q$  as function of time up to  $t = 20$  s [24].”

3.2.1 Actual Solution

$$Q(t) = \int_1^{20} I(t) dt$$

$$= \int_1^{20} 4(1 - e^{-0.5t}) e^{-0.5(t-1)} (1 - e^{-t}) dt$$

$$= \left[ -\frac{8(\sqrt{e}-1)e^{-1.5t}(3e^t-1)}{3} \right]_1^{20}$$

$$= 2.76152102437006 \text{ coulomb}$$

3.2.2 Engineering Application

The above capacitor equation and its solutions can be used in both AC and DC capacitors, to reduce ripple voltage in filter circuits, in a single phase motor, for filtering and tuning circuits, as a storage in digital equipment and long-time constant circuits, for frequency selection in tuning circuits, energy storage in a video flash circuits, suppresses radio frequency interference as used in a snubber circuit etc.

3.3 Volume Flow Rate of Turbulent Flow

“The velocity profile in the turbulent flow of a fluid in a smooth circular pipe may be represented by the empirical power-law equation

$$U(x) = 5 \left(1 - \frac{x}{R}\right)^{1/7}$$

Where  $U(x)$  is the axial velocity in the pipe, in m/s,  $x$  is the radial distance from the axis, in meters, and  $R$  is the radius of the pipe. The total volume flow rate in the pipe is then given by the integral  $\int_0^R U(x) 2\pi x dx$ . Compute the total volume flow rate if  $R = 0.5\text{m}$  [24].”

3.3.1 Actual Solution

The total volume flow rate,

$$\dot{V} = \int_0^{0.5} U(x) 2\pi x dx$$

$$= \int_0^{0.5} 5 \left(1 - \frac{x}{0.5}\right)^{1/7} 2\pi x dx$$

$$= \left[ -10\pi \left(\frac{7}{32} (1 - 2x)^{8/7} - \frac{7}{60} (1 - 2x)^{15/7}\right) \right]_0^{0.5}$$

$$= 3.20704250053958 \text{ m}^3/\text{s}$$

3.3.2 Engineering Application

The equation of volume flow rate of turbulent flow is used for the external flow of air and water over all vehicles types, including automobiles, helicopters, bridges, and submarines, dimples in the golf ball, flow near an airplane, in many manufacturing devices, and machinery like tanks, ducts, precipitators, gas scrubbers, complex scraped surface heat exchangers, etc.

3.4 Wind Force

The pressure  $p$  on a 10 m high structure due to the wind is given by the expression

$$p(x) = \frac{150x}{1 + e^x}$$

where  $x$  is measured in meters from the bottom of the structure and the pressure is in  $\text{N/m}^2$ . If the structure is 2 m wide, the total force due to wind is given by the integral

$$\int_0^{10} 2 p(x) dx.$$

Compute the total force due to wind. [24]

3.4.1 Actual Solution

The total force on the structure due to wind  $F$  is given by the equation

$$F = \int_0^{10} 2 \left(\frac{150x}{1 + e^x}\right) dx$$

$$= [-300x \ln(e^x + 1) - 300Li_2(-e^x) + 150x^2]_0^{10}$$

$$= 246.590293505238 \text{ N}$$

3.4.2 Engineering Application

The equation of wind force can be used in the field of electricity generation by the windmills, sailing vessels, sailboard, grain milling for sports like windsurfing, land surfing, kite surfing, etc.

3.5 Total Momentum Flow

“The velocity profile in the turbulent flow of a fluid in a smooth circular pipe may be represented by the empirical power-law equation

$$U(x) = 5 \left(1 - \frac{x}{R}\right)^{1/7}$$

where  $U(x)$  is the axial velocity in the pipe, in m/s,  $x$  is the radial distance from the axis, in meters, and  $R$  is the radius of the pipe. The momentum flow is given by the integral  $\int_0^R 2\pi x \rho [U(x)]^2 dx$ , where  $\rho$  is the fluid density, given as  $1 \text{ kg/m}^3$  for the fluid considered. Compute the total momentum flow if  $R = 0.5 \text{ m}$  [24].”

3.5.1 Actual Solution

Total momentum flow  $M$  is given by the equation

$$M = \int_0^{0.5} 2\pi x \rho [U(x)]^2 dx$$

$$= \int_0^{0.5} 2\pi x (1) \left[5 \left(1 - \frac{x}{0.5}\right)^{1/7}\right]^2 dx$$

$$= \left[ -\frac{175\pi(18x + 7)(1-2x)^{9/7}}{288} \right]_0^{0.5}$$

$$= 13.3626770855815 \text{ kg.m/s}$$

3.5.2 Engineering Application

The momentum flow equation is generally used for non-uniform flow through a suddenly enlarged pipe, jet propulsion, propellers, hydraulic jump in an open channel, etc.

3.6 Water Force on a Vertical Plate

The force  $F(x)$  exerted per centimeter on a vertical plate immersed in flowing water is given by the expression

$$F(x) = 1.5x^3 e^{-x}$$

where  $x$  is measured from the top of the plate and  $F(x)$  is in  $\text{N/cm}$ . If the plate is 10 cm high, compute the total force  $F_T$ , in Newtons, on the plate is given by [24]

$$F_T = \int_0^{10} F(x) dx$$

3.6.1 Actual Solution

The total force on the plate is given by the equation

$$\begin{aligned}
 F_T &= \int_0^{10} F(x) dx \\
 &= \int_0^{10} 1.5x^3 e^{-x} dx \\
 &= [-1.5e^{-x}(x^3 + 3x^2 + 6x + 6)]_0^{10} \\
 &= 8.90697554391667 \text{ N}
 \end{aligned}$$

3.6.2 Engineering Application

The equation of water force on a vertical plate is used in dam constructions, syringe construction, water tank construction, submarine construction, safety equipment for sea drivers, etc.

3.7 Surface Tension

“The meniscus of a liquid film supported by surface tension can often be represented as

$$h(x) = Ae^{-a^2 x^2}$$

where  $h(x)$  is the height as a function of horizontal distance  $x$  and  $A$  and  $a$  are constants. The total volume of liquid supported by surface tension is then given by the integral  $W = \int_0^L h(x) dx$ , where  $W$  is the width of the meniscus and  $L$  is its length. If  $W$ ,  $L$ ,  $h$ , and  $x$  are all in centimeters, compute this volume for  $A = 0.8$ ,  $a = 2.0$ ,  $W = 1$  cm and  $L = 1$  cm.” [24].

3.7.1 Actual Solution

The total volume of liquid supported by surface tension is

$$\begin{aligned}
 W &= \int_0^L h(x) dx = \int_0^1 Ae^{-a^2 x^2} dx = \int_0^1 0.8e^{-2^2 x^2} dx \\
 &= \left[ \frac{\sqrt{\pi}}{5} \operatorname{erf}(2x) \right]_0^1 \\
 &= 0.35283255630497 \text{ cm}^3
 \end{aligned}$$

3.7.2 Engineering Application

The above equation of surface tension is used to remove pollutants from water and air, inkjet printer, scientific understanding of capillarity, wetting or beading a liquid on a surface, etc.

3.8 Force on Sailboat Mast

“The force on a sailboat mast can be represented by the following function:

$$F = \int_0^H 200 \left( \frac{z}{5+z} \right) e^{-2z/H} dz$$

where  $z$  = the elevation above the deck and  $H$  = the height of the mast. Compute  $F$  for the case where  $H = 30$ .” [25]

3.8.1 Actual Solution

Force on the sailboat mast is given by the equation

$$\begin{aligned}
 F &= \int_0^{30} 200 \left( \frac{z}{5+z} \right) e^{-2z/30} dz \\
 &= \left[ -3000e^{-\frac{x}{15}} + 1000e^{\frac{1}{3}} Ei_1 \left( \frac{x+5}{15} \right) \right]_0^{30} \\
 &= 1480.5684800859 \text{ N}
 \end{aligned}$$

3.8.2 Engineering Application

The equation of force on a sailboat mast is used for iceboats, sail-powered land vehicles, sailing ships, windsurfers, windmill sails, wind turbines, etc.

3.9 Mass Flow Rate

“The amount of mass transported via a pipe over a period of time can be computed as

$$M = \int_{t_1}^{t_2} Q(t)c(t) dt$$

where  $M$  = mass (mg),  $t_1$  = the initial time (min),  $t_2$  = the final time (min),  $Q(t)$  = flow rate ( $m^3/\text{min}$ ), and  $c(t)$  = concentration ( $\text{mg}/m^3$ ). The following functional representations define the temporal variations in flow and concentration:

$$Q(t) = 9 + 5 \cos^2(0.4t); c(t) = 5e^{-0.5t} + 2e^{0.15t},$$

determine the mass transported between  $t_1 = 2$  min and  $t_2 = 8$  min [25].”

3.9.1 Actual Solution

The amount of mass transported via pipe between 2 min and 8 min is

$$\begin{aligned}
 M &= \int_2^8 Q(t)c(t) dt = \int_2^8 (9 + 5 \cos^2(0.4t))(5e^{-0.5t} + 2e^{0.15t}) dt \\
 &= \left[ \frac{e^{-t/2}}{14151} \left( e^{13t/20} \left( 85440 \sin \frac{4t}{5} + 16020 \cos \frac{4t}{5} + 2169820 \right) + 159000 \sin \frac{4t}{5} - 99375 \cos \frac{4t}{5} - 1627365 \right) \right]_2^8 \\
 &= 335.962530061625 \text{ kg}
 \end{aligned}$$

3.9.2 Engineering Application

The mass flow rate equation is used in an industrial cooling tower, chemical component separation in distillation columns, liquid-liquid extraction, as an absorber such as active carbon beds, scrubbers or stripping, etc.

3.10 Rocket Height

“The upward velocity of a rocket can be computed by the following formula:

$$v = u \ln \left( \frac{m_0}{m_0 - qt} \right) - gt$$

where  $v$  = upward velocity,  $u$  = velocity at which fuel is expelled relative to the rocket,  $m_0$  = initial mass of the rocket at time  $t = 0$ ,  $q$  = fuel consumption rate, and  $g$  = downward acceleration of gravity (assumed constant =  $9.81 \text{ m/s}^2$ ). If  $u = 1850 \text{ m/s}$ ,  $m_0 = 160,000 \text{ kg}$ , and  $q = 2500 \text{ kg/s}$ , determine how high the rocket will fly in 30 s [25].”

3.10.1 Actual Solution

In 30 s, the height of the rocket from the ground will be

$$\begin{aligned}
 H &= \int_0^{30} v dt = \int_0^{30} \left( 1850 \ln \left( \frac{160000}{160000 - 2500t} \right) - 9.81t \right) dt \\
 &= \left[ -4.905t^2 + 1850(t - 64) \ln \left( \frac{-64}{t-64} \right) + 1850t - 118400 \right]_0^{30} = 11299.8310550331 \text{ m}
 \end{aligned}$$

### 3.10.2 Engineering Application

The described problem and its solution is used for measuring the rocket height from the surface. Although the rocket ejects fuel to provide thrust, it is an example of conservation of momentum where the system's mass is not constant. The rocket equation calculates the difference of velocity obtained by a rocket after burning an abundance of fuel that reduces the rocket's overall mass.

### 3.11 Paratroopers

“An armed paratrooper with ammunition weighing 322 pounds jumps from a plane with zero initial velocity. The troopers encounter negligible side wind in their descent. However, they encounter air resistance whose magnitude is 15 times the square of the descent velocity  $v(t)$ ; that is,  $15[v(t)]^2$ . Assume that the mass of the parachute is negligible. Estimate the distance paratrooper will travel after 15 s [26].”

#### 3.11.1 Actual Solution

The total mass of the falling body  $m = 322/32.2 = 10$  slugs, and the air resistance  $R(t) = 15[v(t)]^2$  as given. The instantaneous descending velocity  $v(t)$  can be obtained by using

$$\frac{dv(t)}{dt} + \frac{R(t)}{m} = g$$

$$\gg \frac{dv(t)}{dt} + \frac{15[v(t)]^2}{10} = 32.2$$

Consequently, one may express the solution of the above equation with  $v = v(t)$  as

$$v(t) = \frac{4.634(e^{13.9t} - 1)}{e^{13.9t} + 1}$$

So, the distance paratroopers will travel is given by the equation,

$$X = \int_0^{15} \frac{4.634(e^{13.9t} - 1)}{e^{13.9t} + 1} dt$$

$$= \left[ \frac{2317 \ln(e^{13.9t} + 1)}{3475} + \frac{2317t}{500} \right]_0^{15}$$

$$= 69.0478353906885 \text{ ft}$$

#### 3.11.2 Engineering Application

The stated equation and its solution are employed in military force distribution and transportation are frequently utilized in surprise attacks to take important targets such as airfields or bridges, to build an airhead for landing further units, like in the Battle of Crete, and so on.

### 3.12 Horizontal Deflection

“The part shown is formed from a  $\frac{1}{8}$  in diameter steel wire, with  $R = 5$  in and  $l = 4$  in. A force is applied with  $P = 1$  lbf. Use Castigliano’s method to estimate the horizontal deflection at point A [27].”

#### 3.12.1 Actual Solution

For the straight portion,

$$\text{Momentum, } M_{AB} = Px ; \quad \frac{\partial M_{AB}}{\partial P} = x$$

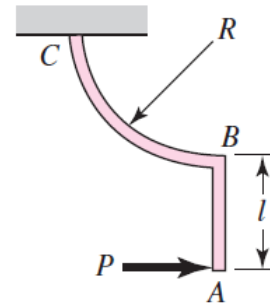


Fig. 2 Beam [27].

For the curved portion,

$$\text{Momentum, } M_{BC} = P[R(1 - \cos \theta) + l] ;$$

$$\frac{\partial M_{BC}}{\partial P} = [R(1 - \cos \theta) + l]$$

The horizontal deflection at point A can be written as

$$\delta = \int_0^l \frac{1}{El} \left( M_{AB} \frac{\partial M_{AB}}{\partial P} \right) dx + \int_0^{\pi/2} \frac{1}{El} \left( M_{BC} \frac{\partial M_{BC}}{\partial P} \right) R d\theta$$

$$= \frac{Pl^3}{3El} + \frac{PR}{El} \int_0^{\pi/2} [R^2(1 - 2 \cos \theta + \cos^2 \theta) + 2Rl(1 - \cos \theta) + l^2] d\theta$$

$$= \frac{(1)(4^3)}{3(30)(10^6)\pi(0.125^4)/64} + \frac{(1)(5)}{(30)(10^6)\pi(0.125^4)/64} \int_0^{\pi/2} [5^2(1 - 2 \cos \theta + \cos^2 \theta) + 2(5)(4)(1 - \cos \theta) + 4^2] d\theta$$

$$= \frac{(1)(4^3)}{3(30)(10^6)\pi(0.125^4)/64} + \frac{(1)(5)}{(30)(10^6)\pi(0.125^4)/64} \left[ \frac{25 \sin(2\theta) - 360 \sin \theta + 374\theta}{4} \right]_0^{\pi/2}$$

$$= 0.85023052811512 \text{ in}$$

#### 3.12.2 Engineering Application

The horizontal deflection equation can be used in various places, including houses and bridges, lifting beams, gantry cranes, to prevent differential settlement and distribute lateral forces caused by earthquakes, strength calculations, etc.

### 3.13 Block-Type Hand Brake (Moment of Frictional Forces)

“The block-type hand brake shown in the Fig. 3 has a face width of 1.25 in and a mean coefficient of friction of 0.25. For a maximum pressure on the shoe of 27.4 psi, find the moment of frictional forces [27].”

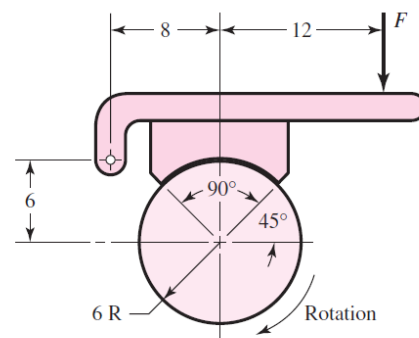


Fig. 3 Block type hand brake [27].

3.13.1 Actual Solution

Given, face width  $b = 1.25$  in, mean coefficient of friction  $f = 0.25$ , radius  $r = 6$  in, maximum pressure on the shoe  $P_a = 27.4$  psi.

Here,  $\theta_1 = 45^\circ - \tan^{-1}(6/8) = 8.13^\circ$ ,  $\theta_2 = 98.13^\circ$ ,  $\theta_a = 90^\circ$ ,  $a = (6^2 + 8^2)^{0.5} = 10$  in

So the moment of friction forces can be written as

$$M_f = \frac{f P_a b r}{\sin \theta_a} \int_{\theta_1}^{\theta_2} \sin \theta (r - a \cos \theta) d\theta$$

$$= \frac{(0.25)(27.4)(1.25)(6)}{1} \int_{8.13^\circ}^{98.13^\circ} \sin \theta (6 - 10 \cos \theta) d\theta$$

$$= \frac{(0.25)(27.4)(1.25)(6)}{1} [\cos \theta (5 \cos \theta - 6)]_{8.13^\circ}^{98.13^\circ}$$

$$= 102.144340253044 \text{ lbf.in}$$

3.14 Block-Type Hand Brake (Moment of Normal Forces)

“The block-type hand brake shown in Fig. 4 has a face width of 1.25 in and a mean coefficient of friction of 0.25. For a maximum pressure on the shoe of 27.4 psi, find the moment of normal forces [27].”

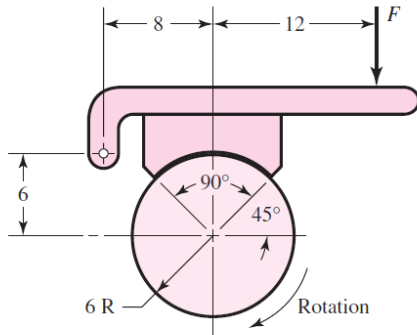


Fig. 4 Block type hand brake [27].

3.14.1 Actual Solution

Given, face width  $b = 1.25$  in, mean coefficient of friction  $f = 0.25$ , radius  $r = 6$  in, maximum pressure on the shoe  $P_a = 27.4$  psi.

Here,  $\theta_1 = 45^\circ - \tan^{-1}(6/8) = 8.13^\circ$ ,  $\theta_2 = 98.13^\circ$ ,  $\theta_a = 90^\circ$ ,  $a = (6^2 + 8^2)^{0.5} = 10$  in

So the moment of friction forces can be written as

$$M_N = \frac{a P_a b r}{\sin \theta_a} \int_{\theta_1}^{\theta_2} \sin^2 \theta d\theta = \frac{(10)(27.4)(1.25)(6)}{1} \int_{8.13^\circ}^{98.13^\circ} \sin^2 \theta d\theta$$

$$= \frac{(10)(27.4)(1.25)(6)}{1} \left[ \frac{2\theta - \sin(2\theta)}{4} \right]_{8.13^\circ}^{98.13^\circ}$$

$$= 1901.68970153642 \text{ lbf.in}$$

3.14.2 Engineering Application

The above equation of hand brake is used in the automobile. Hand brakes are sometimes referred to as parking brakes, and emergency brakes are used to hold the vehicle steady. It can operate in various places, including racing cars.

3.15 Speed of Block

“The block of mass  $M = 2$  kg is subjected to a force having a constant direction and a magnitude  $F = k/(a+bx)$  where,  $k = 300$  N,  $a = 1$ ,  $b = 1 \text{ m}^{-1}$ . When  $x = x_1 = 4$  m, the block is moving

to the left with a speed  $v_1 = 8 \text{ m/s}$ . Determine its speed when  $x = x_2 = 12$  m. The coefficient of kinetic friction between the block and the ground is  $\mu_k = 0.25$  [28].”

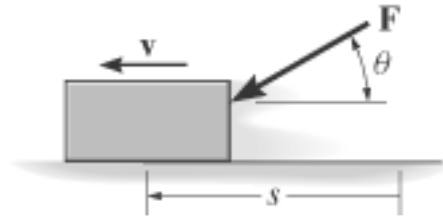


Fig. 5 Block [28].

3.15.1 Actual Solution

Considering  $\theta = 30^\circ$  and  $g = 9.81 \text{ ms}^{-2}$ , the speed of the block when  $x = x_2 = 12$  m will be written as

$$v = \sqrt{v_1^2 + \frac{2 \left( \int_{x_1}^{x_2} \frac{k \cos \theta}{a+bx} dx - \mu_k \int_{x_1}^{x_2} Mg + \frac{k \sin \theta}{a+bx} dx \right)}{M}}$$

$$= \sqrt{8^2 + \frac{2 \left( 300 \int_4^{12} \frac{\cos 30^\circ}{1+x} dx - 0.25 \int_4^{12} 2(9.8) + \frac{300 \sin 30^\circ}{1+x} dx \right)}{2}}$$

$$= 15.4005674022625 \text{ m/s}$$

3.15.2 Engineering Application

The problem mentioned can be utilized to measure the speed when friction is used. We can walk due to friction; friction is used to hold together other items, heat switching through matches, and transportation system also requires acceleration friction, braking, etc.

3.16 Rocket Velocity

“A rocket has an empty weight  $W_1 = 500$  lb and carries fuel of weight  $W_2 = 300$  lb. If the fuel is burned at the rate  $c = 15 \text{ lb/s}$  and ejected with a relative velocity  $v_{DR} = 4400 \text{ ft/s}$  determine the maximum speed attained by the rocket starting from rest. Neglect the effect of gravitation on the rocket. (Gravitational acceleration  $g = 32.2 \text{ ft/s}$ ) [28].”

3.16.1 Actual Solution

$$\text{Initial mass of the rocket } m_0 = \frac{W_1 + W_2}{g} = \frac{800}{32.2} \text{ lb}$$

The maximum speed occurs when all the fuel is consumed, that is, where time  $t = \frac{W_2}{c} = \frac{300}{15} = 20$  s

The maximum speed of the rocket,

$$v_{max} = \int_0^t \frac{c v_{DR}}{m_0 - \frac{c}{g} t} dt = \int_0^{20} \frac{\frac{15}{32.2}(4400)}{\frac{800}{32.2} - \frac{15}{32.2} t} dt$$

$$= [-4400 \ln|3t - 160|]_0^{20}$$

$$= 2068.01596868123 \text{ ft/s}$$

3.16.2 Engineering Application

Rockets are used to launch artificial satellites, human spaceflight, and space exploration, as well as for pyrotechnics, weapons, and ejection seats. Chemical rockets are the most frequent type of high-powered rocket, and they typically generate a high-speed exhaust by mixing fuel and an oxidizer.

3.17 Gear Box

“Morse Industrial manufactures the speed reducer shown. If a motor drives the gear shaft *S* with an angular acceleration  $\alpha = ke^{bt}$ , where  $k = 0.4 \text{ rad/s}^2$ ,  $b = 1 \text{ s}^{-1}$ . Determine the angular velocity of shaft *E* at time  $t = 2 \text{ s}$  after starting from rest. The radii of gear A, B, C, and D are 20 mm, 80 mm, 30 mm, and 120 mm respectively. Note that gears *B* and *C* are fixed connected to the same shaft [28].”



Fig. 6 Speed reducer [28].

3.17.1 Actual Solution

Angular velocity,

$$\omega = \int_0^t ke^{bt} dt = \int_0^t 0.4e^t dt = [0.4e^t]_0^2$$

$$= 0.15972640247327 \text{ rad/s}$$

3.17.2 Engineering Application

The problem described and its solution are utilized in a variety of industries and machines. Factory automation, packaging machines, industrial machines, food processing machines, car production machines, machine tool industry, material handling, printing machines, automatic cutting/welding machines, machines for medical/cosmetic fields, construction machines, wood/glass processing machines, agricultural machinery, material processing machines, and so on are among the required application fields.

4 Results and Discussion

The engineering integral equations were solved and the actual values were determined using Maple program. For determining the most accurate method, we followed some definite steps. First, we found the numerical integration solutions of the four methods by using Python 3.8. We considered the intervals from 6 to 500. The detail of the comparison of various methods for the periodicity and accuracy is summarized in Table 1. The data for the graphs were constructed using Pandas. Two graphs were exhibited- one containing a maximum number of values and the other containing values from the selected zone. The graphs were constructed using Matplotlib.

Table 1 Comparison of various methods for the periodicity and accuracy.

Problem Name	Number of intervals to start forming the most accurate method	Number of intervals for the most accurate method (when n = 1, 2, 3, ...)			
		Weddle's method	Simpson's 1/3 method	Simpson's 3/8 method	Trapezoidal method
Spring	6	6n	6n+2 or 6n+4	6n+3	6n+1 or 6n+5
Capacitor	204	6n	6n+2 or 6n+4	6n+1 or 6n+3 or 6n+5	No interval
Volume flow rate of turbulent flow	24	6n or 6n+2 or 6n+4	No interval	6n+3	6n+1 or 6n+5
Wind force	30	6n	6n+2 or 6n+4	6n+1 or 6n+3 or 6n+5	No interval
Total momentum flow	18	6n or 6n+2 or 6n+4	No interval	6n+3	6n+1 or 6n+5
Water force on a vertical plate	54	6n	6n+2 or 6n+4	6n+3	6n+1 or 6n+5
Surface tension	6	6n	6n+2 or 6n+4	6n+3	6n+1 or 6n+5
Force on a sailboat mast	18	6n	6n+2 or 6n+4	6n+3	6n+1 or 6n+5
Mass flow rate	6	6n	6n+2 or 6n+4	6n+3	6n+1 or 6n+5
Rocket height	6	6n	6n+2 or 6n+4	6n+3	6n+1 or 6n+5
Paratroopers	42	6n	6n+2 or 6n+4	6n+3	6n+1 or 6n+5
Horizontal deflection	6	6n	6n+2 or 6n+4	6n+3	6n+1 or 6n+5
Block-type hand brake (moment of frictional forces)	6	6n	6n+2 or 6n+4	6n+3	6n+1 or 6n+5
Block-type hand brake (moment of normal forces)	6	6n	6n+2 or 6n+4	6n+3	6n+1 or 6n+5
Speed of block	6	6n	6n+2 or 6n+4	6n+3	6n+1 or 6n+5
Rocket velocity	6	6n	6n+2 or 6n+4	6n+3	6n+1 or 6n+5
Gear box	6	6n	6n+2 or 6n+4	6n+3	6n+1 or 6n+5

In the spring problem, the sequence of the most accurate numerical integration method has started forming when the number of intervals was 6. When the number of intervals was  $6n$  (where  $n = 1, 2, 3, 4, \dots$ ), Weddle's method was found to be the most accurate. But when the number of intervals changed to  $6n + 2$  or  $6n + 4$ , the most accurate method was Simpson's  $1/3$ . Simpson's  $3/8$  method was found to be the most accurate when the number of intervals was  $6n + 3$ . For a number of intervals equal to  $6n + 1$  or  $6n + 5$ , Trapezoidal method became the most accurate. The visual proof of the aforementioned sentences is shown in Fig. 7.

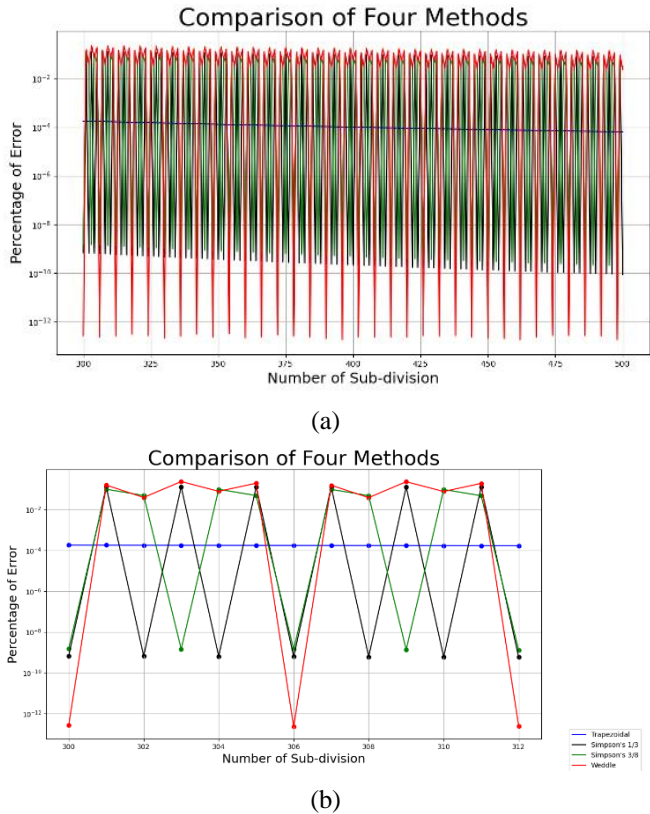


Fig. 7 Graph of Percentage of error vs. Number of Sub-division for spring problem (a) Whole (b) Magnified

In the capacitor problem, the sequence of the most accurate numerical integration method has started forming when the number of intervals was 204. When the number of intervals was  $6n$  (where  $n = 34, 35, 36, 37, \dots$ ), Weddle's method was found to be the most accurate. But when the number of intervals changed to  $6n + 2$  or  $6n + 4$ , Simpson's  $1/3$  method was found to be the most accurate. Simpson's  $3/8$  method was found to be the most accurate when the number of intervals was  $6n + 1$  or  $6n + 3$  or  $6n + 5$ . There is no number of intervals for which Trapezoidal method was found to be the most accurate. The visual proof of the aforementioned sentences is shown in Fig. 8.

In the volume flow rate of the turbulent flow problem, the sequence of the most accurate numerical integration method has started forming when the number of intervals was 24. When the number of intervals was  $6n$  or  $6n + 2$  or  $6n + 4$  (where  $n = 4, 5, 6, 7, \dots$ ), Weddle's method was found to be the most accurate. There is no number of intervals for which Simpson's  $1/3$  method was found to be the most accurate. But when the number of intervals changed to  $6n + 3$ , Simpson's  $3/8$  method was found to be the most accurate. The trapezoidal method was found to be the most accurate when a number of intervals switched to  $6n + 1$

or  $6n + 5$ . The visual proof of the aforementioned sentences is shown in Fig. 9.

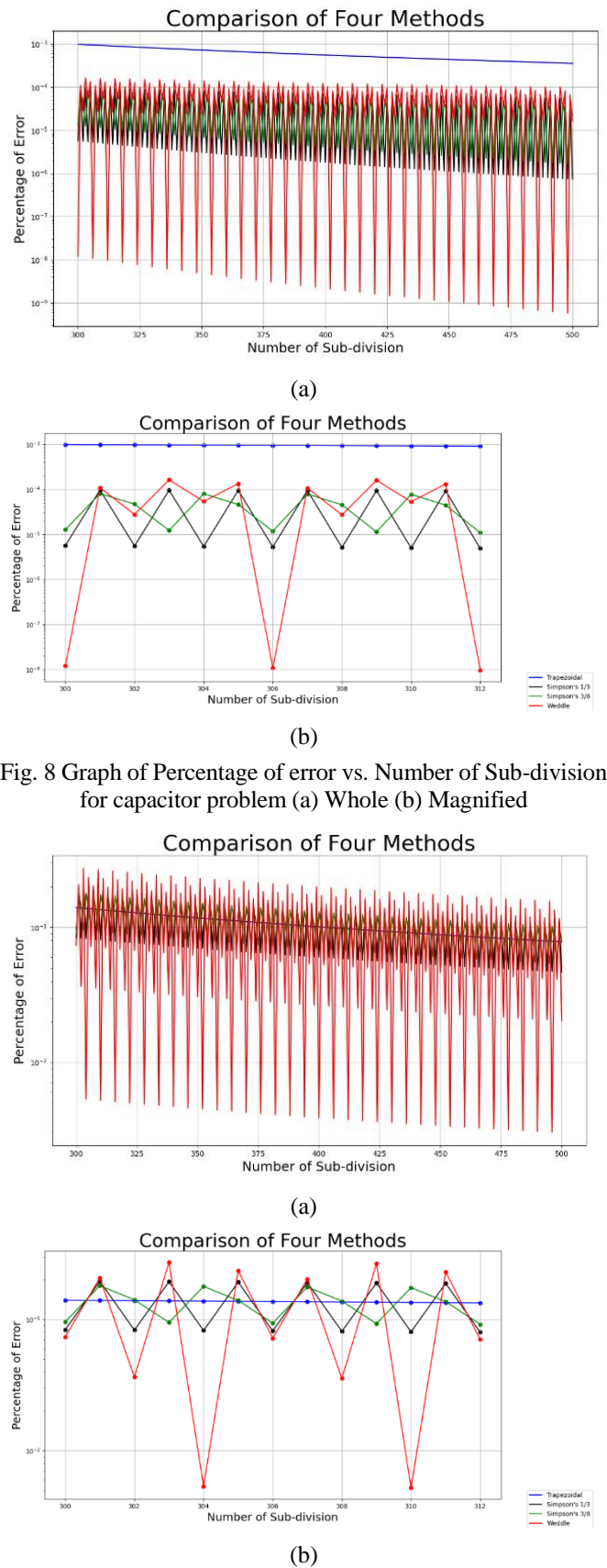


Fig. 8 Graph of Percentage of error vs. Number of Sub-division for capacitor problem (a) Whole (b) Magnified

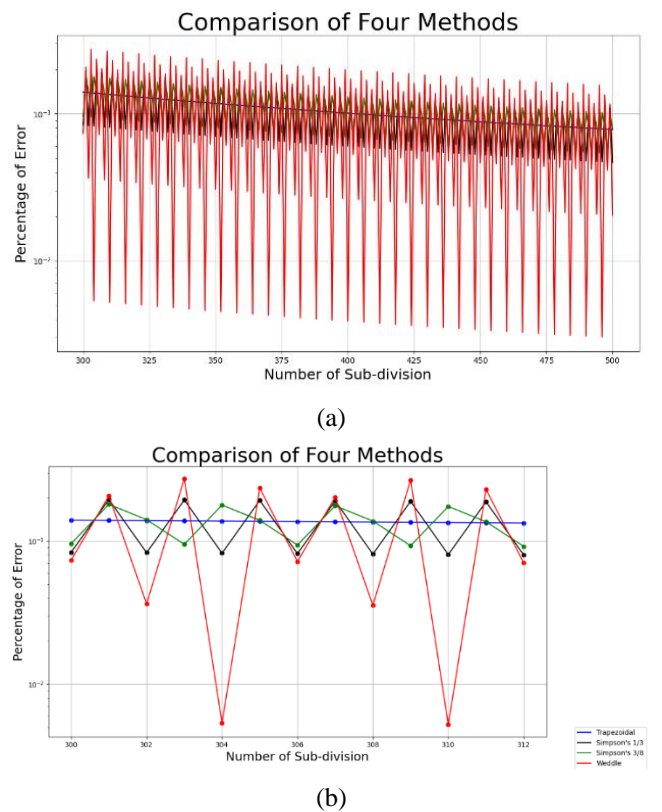


Fig. 9 Graph of Percentage of error vs. Number of Sub-division for volume flow rate of turbulent flow problem (a) Whole (b) Magnified

In the wind force problem, the sequence of the most accurate numerical integration method has started forming when the number of intervals was 30. When the number of intervals was  $6n$  (where  $n = 5, 6, 7, 8, \dots$ ), Weddle's method was found to be the most accurate. But when the number of intervals changed to  $6n + 2$  or  $6n + 4$ , Simpson's  $1/3$  method was found to be the most accurate. Simpson's  $3/8$  method was found to be the most accurate when the number of intervals was  $6n + 1$  or  $6n + 3$  or  $6n + 5$ . There is no number of intervals for which the Trapezoidal method was found to be the most accurate. The visual proof of the aforementioned sentences is shown in Fig. 10.

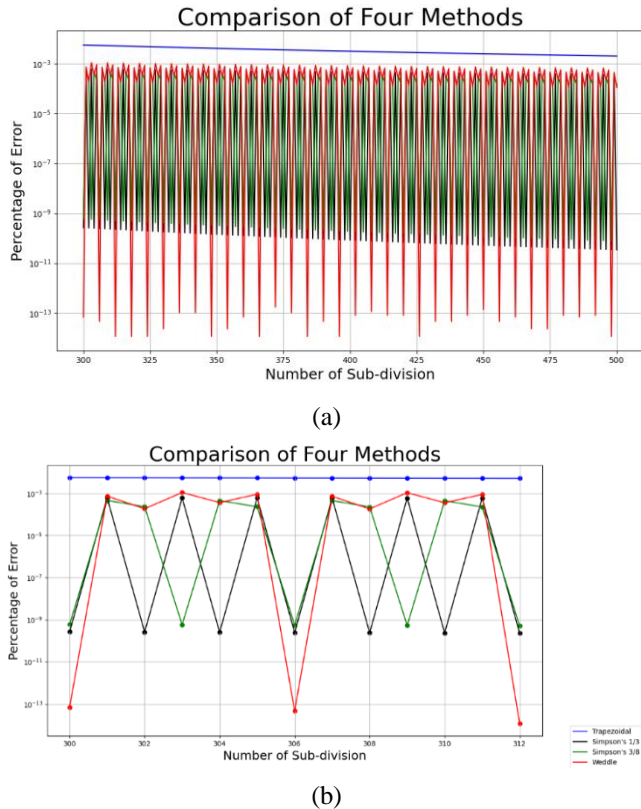


Fig. 10 Graph of Percentage of error vs. Number of Sub-division for wind force problem (a) Whole (b) Magnified

In the total momentum flow problem, the sequence of the most accurate numerical integration method has started forming when the number of intervals was 18. When the number of intervals was  $6n$  or  $6n + 2$  or  $6n + 4$  (where  $n = 3, 4, 5, 6, \dots$ ), Weddle's method was found to be the most accurate. There is no number of intervals for which Simpson's  $1/3$  method was found to be the most accurate. But when the number of intervals changed to  $6n + 3$ , Simpson's  $3/8$  method was found to be the most accurate. The trapezoidal method was found to be the most accurate when a number of intervals switched to  $6n + 1$  or  $6n + 5$ . The visual proof of the aforementioned sentences is shown in Fig. 11.

In the water force on a vertical plate problem, the sequence of the most accurate numerical integration method has started forming when the number of intervals was 54. When the number of intervals was  $6n$  (where  $n = 9, 10, 11, 12, \dots$ ), Weddle's method was found to be the most accurate. But when the number of intervals changed to  $6n + 2$  or  $6n + 4$ , Simpson's  $1/3$  method was found to be the most accurate. Simpson's  $3/8$  method was found to be the most accurate when the number of intervals was  $6n + 3$ . The trapezoidal method was found to be the most accurate

when a number of intervals switched to  $6n + 1$  or  $6n + 5$ . The visual proof of the aforementioned sentences is shown in Fig. 12.

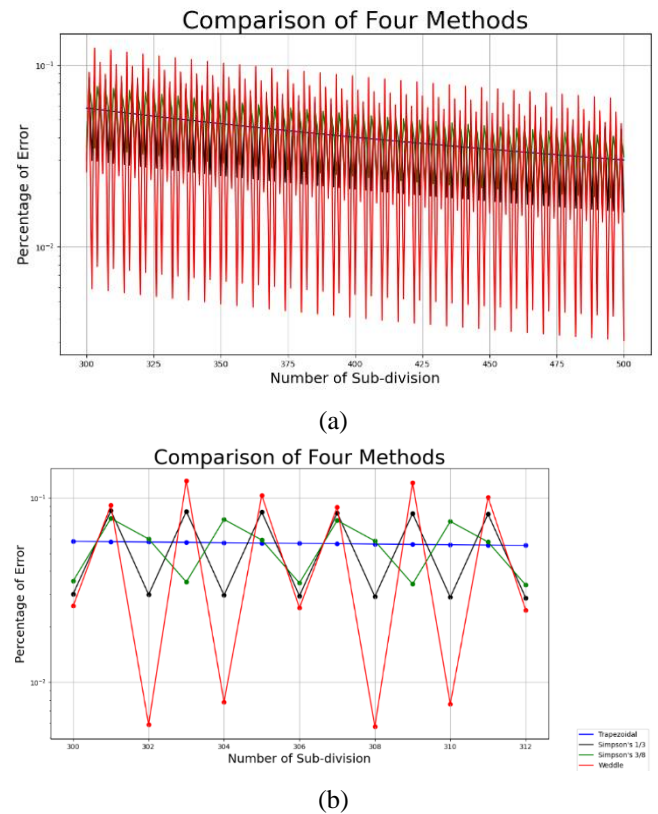


Fig. 11 Graph of Percentage of error vs. Number of Sub-division for total momentum flow problem (a) Whole (b) Magnified

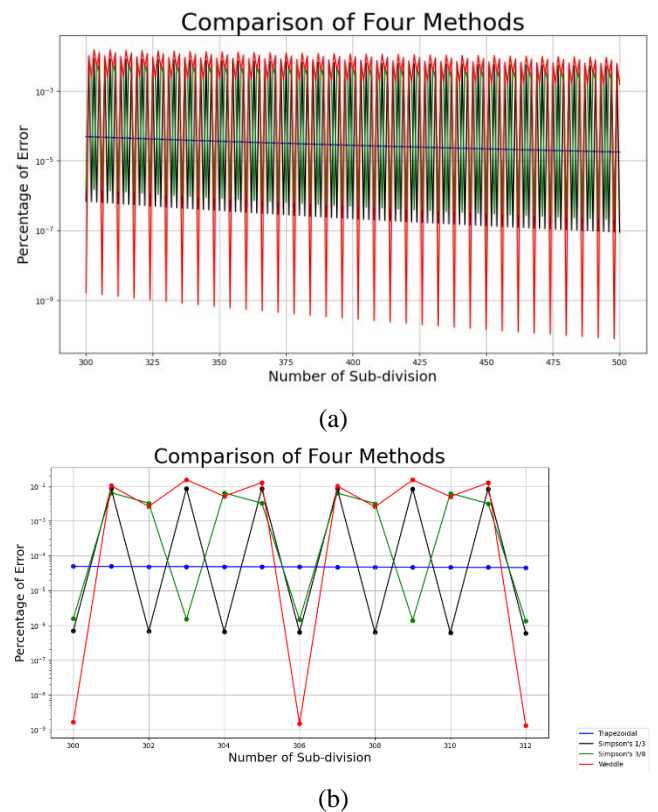


Fig. 12 Graph of Percentage of error vs. Number of Sub-division for water force on a vertical plate problem (a) Whole (b) Magnified

In the surface tension problem, the sequence of the most accurate numerical integration method has started forming when the number of intervals was 6. When the number of intervals was  $6n$  (where  $n = 1, 2, 3, 4, \dots$ ), Weddle's method was found to be the most accurate. But when the number of intervals changed to  $6n + 2$  or  $6n + 4$ , Simpson's 1/3 method was found to be the most accurate. Simpson's 3/8 method was found to be the most accurate when the number of intervals was  $6n + 3$ . The trapezoidal method was found to be the most accurate when a number of intervals switched to  $6n + 1$  or  $6n + 5$ . The visual proof of the aforementioned sentences is shown in Fig. 13.

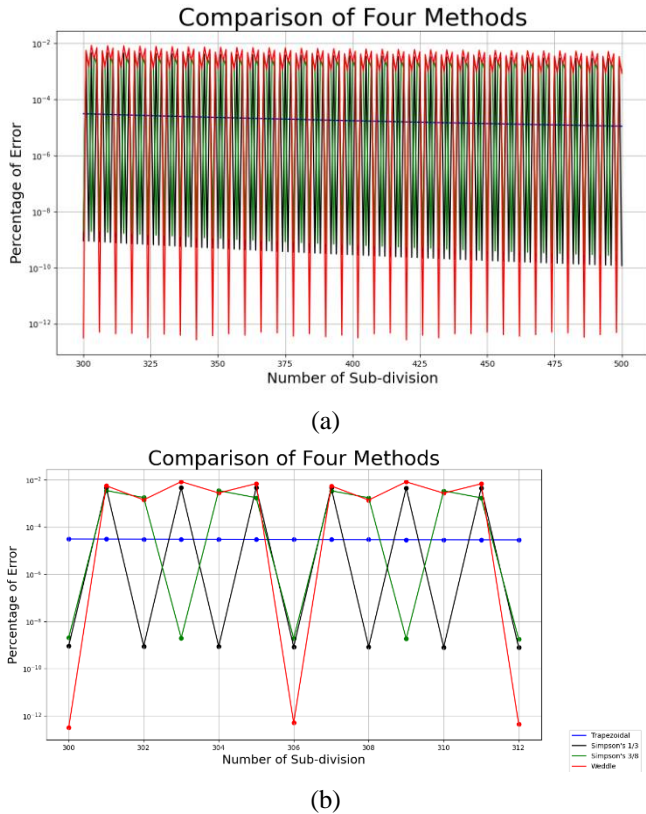


Fig. 13 Graph of Percentage of error vs. Number of Sub-division for surface tension problem (a) Whole (b) Magnified

In the force on a sailboat mast problem, the sequence of the most accurate numerical integration method has started forming when the number of intervals was 18. When the number of intervals was  $6n$  (where  $n = 3, 4, 5, 6, \dots$ ), Weddle's method was found to be the most accurate. But when the number of intervals changed to  $6n + 2$  or  $6n + 4$ , Simpson's 1/3 method was found to be the most accurate. Simpson's 3/8 method was found to be the most accurate when the number of intervals was  $6n + 3$ . The trapezoidal method was found to be the most accurate when a number of intervals switched to  $6n + 1$  or  $6n + 5$ . The visual proof of the aforementioned sentences is shown in Fig. 14.

In the mass flow rate problem, the sequence of the most accurate numerical integration method has started forming when the number of intervals was 6. When the number of intervals was  $6n$  (where  $n = 1, 2, 3, 4, \dots$ ), Weddle's method was found to be the most accurate. But when the number of intervals changed to  $6n + 2$  or  $6n + 4$ , Simpson's 1/3 method was found to be the most accurate. Simpson's 3/8 method was found to be the most accurate when the number of intervals was  $6n + 3$ . The trapezoidal method was found to be the most accurate when a number of intervals switched to  $6n + 1$  or  $6n + 5$ . The visual proof of the aforementioned sentences is shown in Fig. 15.

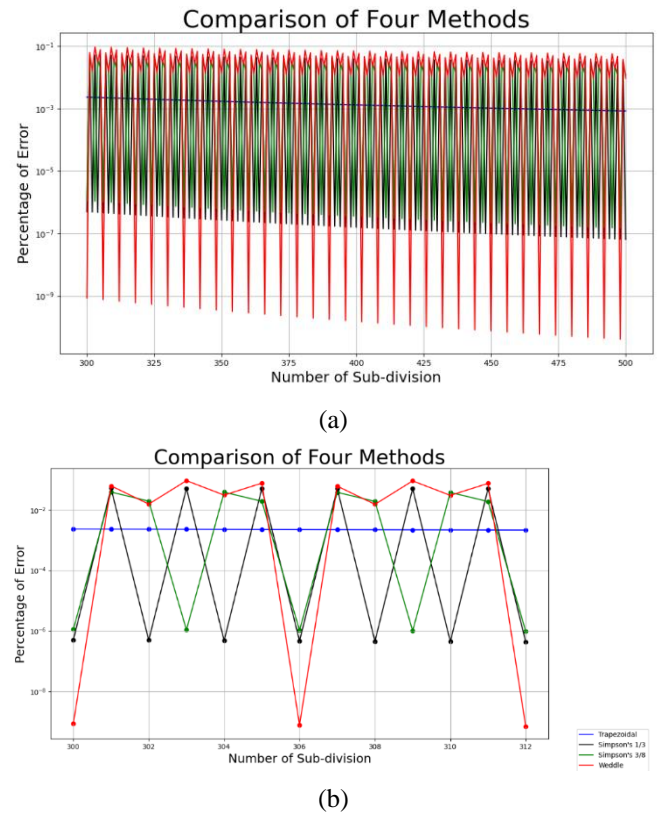


Fig. 14 Graph of Percentage of error vs. Number of Sub-division for force on a sailboat mast problem (a) Whole (b) Magnified

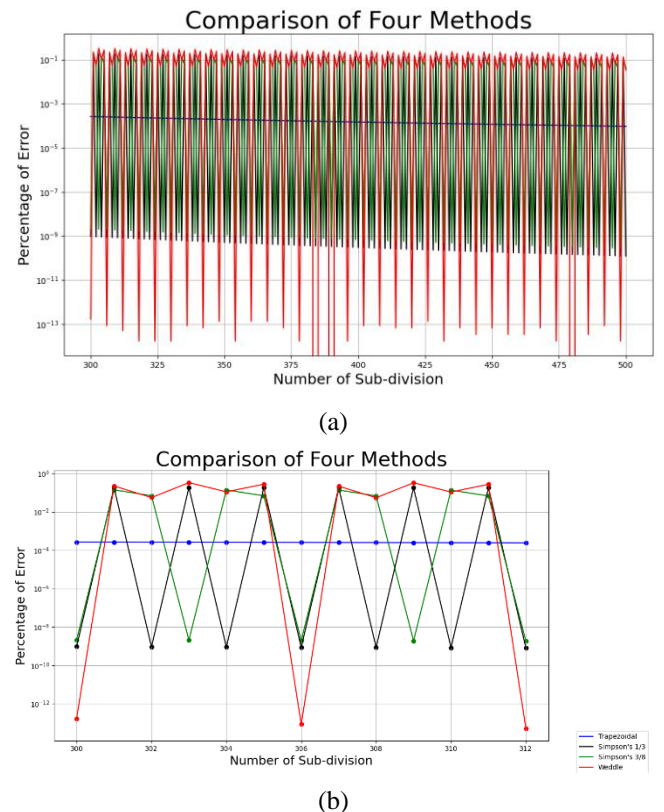


Fig. 15 Graph of Percentage of error vs. Number of Sub-division for mass flow rate problem (a) Whole (b) Magnified

In the rocket height problem, the sequence of the most accurate numerical integration method has started forming when

the number of intervals was 6. When the number of intervals was  $6n$  (where  $n = 1, 2, 3, 4, \dots$ ), Weddle's method was found to be the most accurate. But when the number of intervals changed to  $6n + 2$  or  $6n + 4$ , Simpson's 1/3 method was found to be the most accurate. Simpson's 3/8 method was found to be the most accurate when the number of intervals was  $6n + 3$ . The trapezoidal method was found to be the most accurate when a number of intervals switched to  $6n + 1$  or  $6n + 5$ . The visual proof of the aforementioned sentences is shown in Fig. 16.

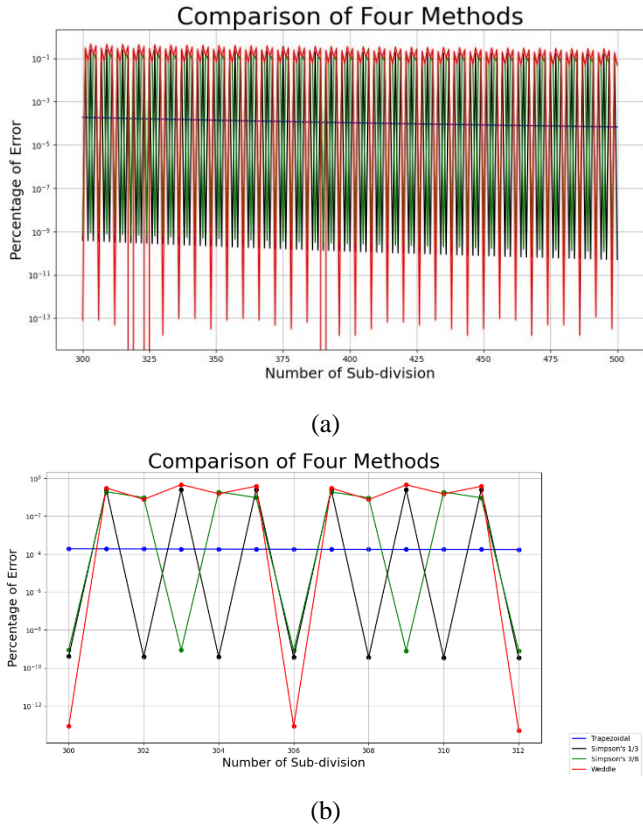


Fig. 16 Graph of Percentage of error vs. Number of Sub-division for rocket height problem (a) Whole (b) Magnified

In the paratroopers problem, the sequence of the most accurate numerical integration method has started forming when the number of intervals was 42. When the number of intervals was  $6n$  (where  $n = 7, 8, 9, 10, \dots$ ), Weddle's method was found to be the most accurate. But when the number of intervals changed to  $6n + 2$  or  $6n + 4$ , Simpson's 1/3 method was found to be the most accurate. Simpson's 3/8 method was found to be the most accurate when the number of intervals was  $6n + 3$ . The trapezoidal method was found to be the most accurate when a number of intervals switched to  $6n + 1$  or  $6n + 5$ . The visual proof of the aforementioned sentences is shown in Fig. 17.

In the horizontal deflection problem, the sequence of the most accurate numerical integration method has started forming when the number of intervals was 6. When the number of intervals was  $6n$  (where  $n = 1, 2, 3, 4, \dots$ ), Weddle's method was found to be the most accurate. But when the number of intervals changed to  $6n + 2$  or  $6n + 4$ , Simpson's 1/3 method was found to be the most accurate. Simpson's 3/8 method was found to be the most accurate when the number of intervals was  $6n + 3$ . The trapezoidal method was found to be the most accurate when a number of intervals switched to  $6n + 1$  or  $6n + 5$ . The visual proof of the aforementioned sentences is shown in Fig. 18.

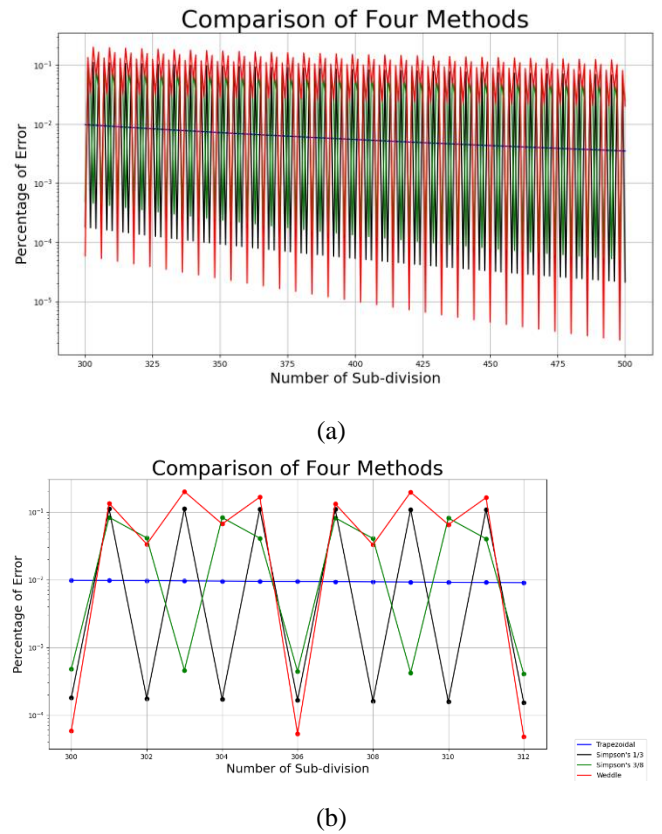


Fig. 17 Graph of Percentage of error vs. Number of Sub-division for paratroopers problem (a) Whole (b) Magnified

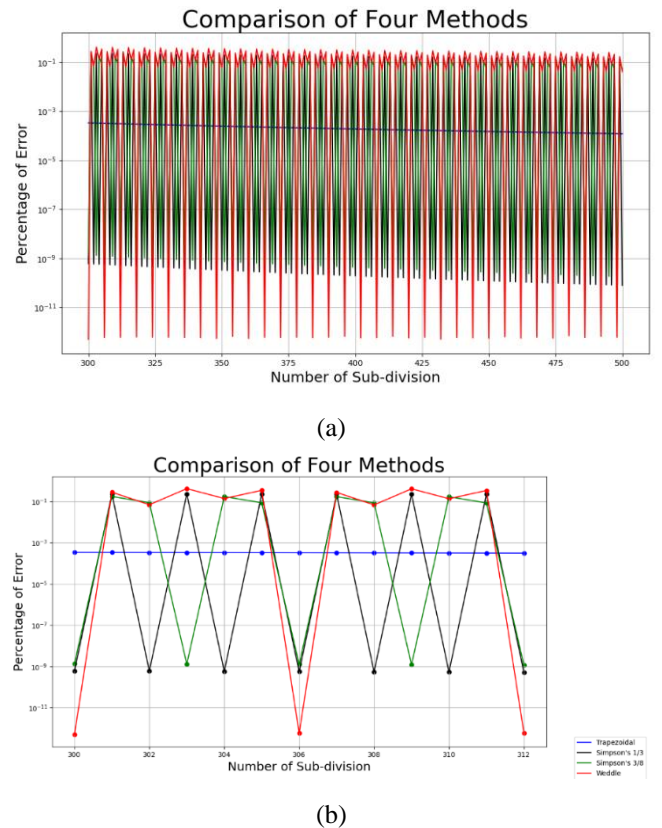


Fig. 18 Graph of Percentage of error vs. Number of Sub-division for horizontal deflection problem (a) Whole (b) Magnified

In the block-type hand brake (moment of frictional forces) problem, the sequence of the most accurate numerical integration method has started forming when the number of intervals was 6. When the number of intervals was  $6n$  (where  $n = 1, 2, 3, 4, \dots$ ), Weddle's method was found to be the most accurate. But when the number of intervals changed to  $6n + 2$  or  $6n + 4$ , Simpson's  $1/3$  method was found to be the most accurate. Simpson's  $3/8$  method was found to be the most accurate when the number of intervals was  $6n + 3$ . The trapezoidal method was found to be the most accurate when a number of intervals switched to  $6n + 1$  or  $6n + 5$ . The visual proof of the aforementioned sentences is shown in Fig. 19.

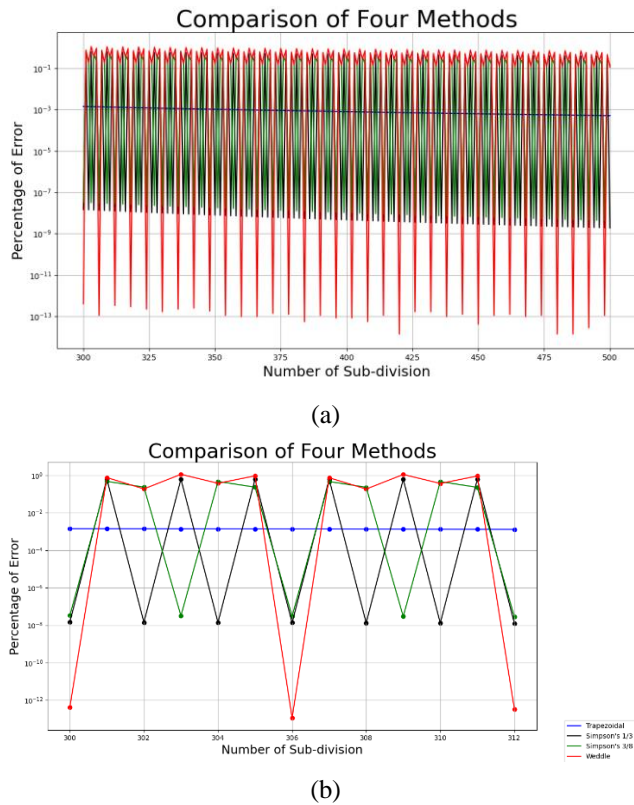


Fig. 19 Graph of Percentage of error vs. Number of Sub-division for block-type hand brake (moment of frictional forces) problem (a) Whole (b) Magnified

In the block-type hand brake (moment of normal forces) problem, the sequence of the most accurate numerical integration method has started forming when the number of intervals was 6. When the number of intervals was  $6n$  (where  $n = 1, 2, 3, 4, \dots$ ), Weddle's method was found to be the most accurate. But when the number of intervals changed to  $6n + 2$  or  $6n + 4$ , Simpson's  $1/3$  method was found to be the most accurate. Simpson's  $3/8$  method was found to be the most accurate when the number of intervals was  $6n + 3$ . The trapezoidal method was found to be the most accurate when a number of intervals switched to  $6n + 1$  or  $6n + 5$ . The visual proof of the aforementioned sentences is shown in Fig. 20.

In the speed of block problem, the sequence of the most accurate numerical integration method has started forming when the number of intervals was 6. When the number of intervals was  $6n$  (where  $n = 1, 2, 3, 4, \dots$ ), Weddle's method was found to be the most accurate. But when the number of intervals changed to  $6n + 2$  or  $6n + 4$ , Simpson's  $1/3$  method was found to be the most accurate. Simpson's  $3/8$  method was found to be the most accurate when the number of intervals was  $6n + 3$ . The

trapezoidal method was found to be the most accurate when a number of intervals switched to  $6n + 1$  or  $6n + 5$ . The visual proof of the aforementioned sentences is shown in Fig. 21.

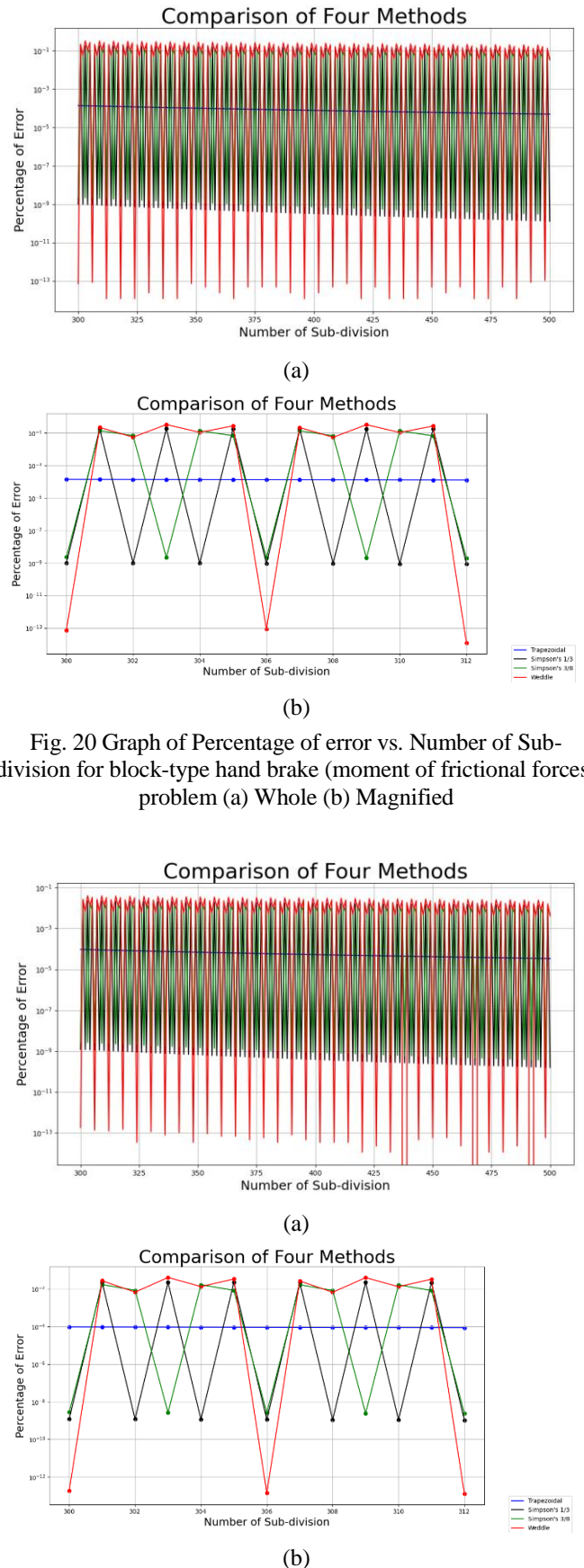


Fig. 21 Graph of Percentage of error vs. Number of Sub-division for speed of block problem (a) Whole (b) Magnified

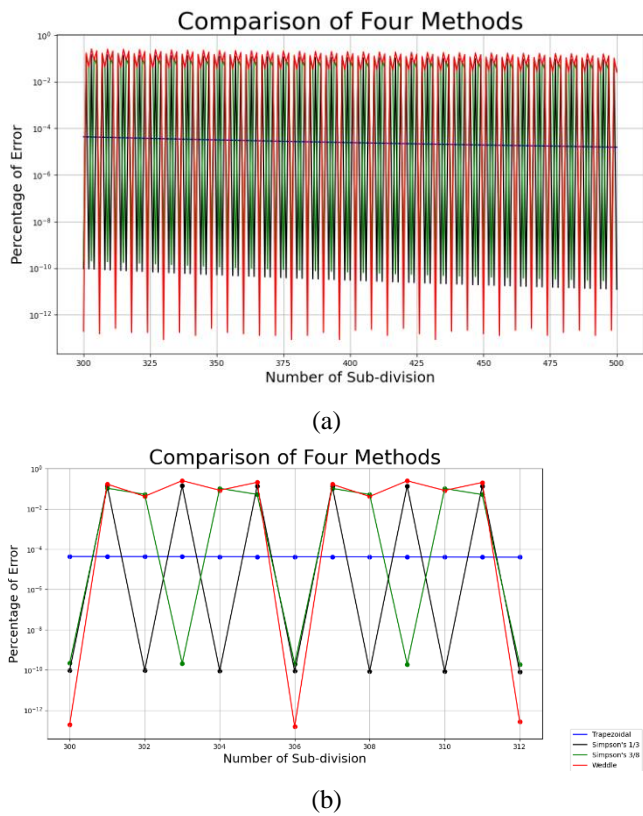


Fig. 22 Graph of Percentage of error vs. Number of Sub-division for rocket velocity problem (a) Whole (b) Magnified

In the rocket velocity problem, the sequence of the most accurate numerical integration method has started forming when the number of intervals was 6. When the number of intervals was  $6n$  (where  $n = 1, 2, 3, 4, \dots$ ), Weddle's method was found to be the most accurate. But when the number of intervals changed to  $6n + 2$  or  $6n + 4$ , Simpson's 1/3 method was found to be the most accurate. Simpson's 3/8 method was found to be the most accurate when the number of intervals was  $6n + 3$ . The trapezoidal method was found to be the most accurate when a number of intervals switched to  $6n + 1$  or  $6n + 5$ . The visual proof of the aforementioned sentences is shown in Fig. 22.

In the gear box problem, the sequence of the most accurate numerical integration method has started forming when the number of intervals was 6. When the number of intervals was  $6n$  (where  $n = 1, 2, 3, 4, \dots$ ), Weddle's method was found to be the most accurate. But when the number of intervals changed to  $6n + 2$  or  $6n + 4$ , Simpson's 1/3 method was found to be the most accurate. Simpson's 3/8 method was found to be the most accurate when the number of intervals was  $6n + 3$ . The trapezoidal method was found to be the most accurate when a number of intervals switched to  $6n + 1$  or  $6n + 5$ . The visual proof of the aforementioned sentences is shown in Fig. 23.

### 5 Discussion

The solved problems along with their sequences of accurate methods are shown below with a Sunburst Chart as shown in Fig. 24. In the chart, 'W'=Weddle's Rule, 'T'=Trapezoidal Rule, 'S1/3'=Simpson's 1/3 Rule, and 'S3/8'=Simpson's 3/8 Rule.

From Fig. 24, it is clearly visible that most of the selected engineering problems follow a common sequence of 'W-T-S1/3-S3/8-S1/3-T-W'. In total, 13 out of 17 problems exhibit this periodic sequence of accuracy. Also, 2 out of 17 demonstrate a sequence of 'W-S3/8-S1/3-S3/8-S1/3-S3/8-W'. Interestingly, trapezoidal method is never the most accurate one for these two problems. Finally, 2 out of 17 problems show a sequence of 'W-T-W-T-W-S3/8-W'. Simpson's 1/3 is never the most accurate method for these two problems.

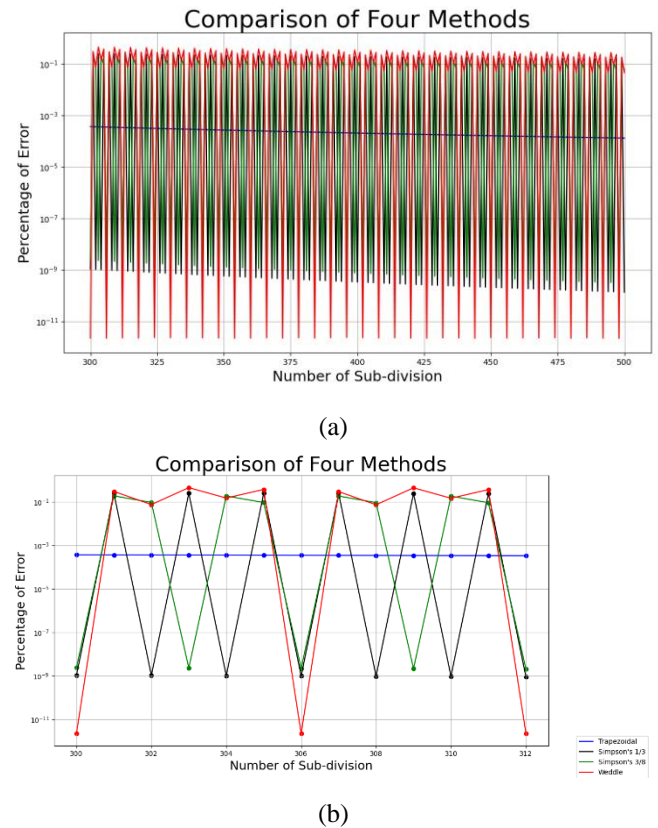


Fig. 23 Graph of Percentage of error vs. Number of Sub-division for gear box problem (a) Whole (b) Magnified

### 6 Conclusion

In our paper, some integration problems were brought together and solved by using Python 3.8. The graphs and the data for individual problems were found using Matplotlib and Pandas respectively. The problems were chosen meticulously according to their application in the different engineering fields. By analyzing the problems, it was found that there was no single numerical integration method among the Newton-Cotes methods whose accuracy was constantly maintained throughout the interval. Rather, it is seen that with the change of interval, the most accurate method changes and there is an interesting pattern of accuracy that is followed in each engineering problem. This will give insights to the scientists and engineers working in the field, on what methods they can use according to their necessary accuracy demand of their industries. This can further be extended to the other engineering applications as well so that the most accurate value within a particular interval can be known.



# Volume Charge Density in Geometric Product Lorentz Transformation

Md. Ashrafal Alam<sup>\*1</sup> and Atikur Rahman Baizid<sup>2</sup>

<sup>1</sup>Department of Mechanical Engineering, University of Creative Technology, Chittagong, Chattogram-4212, Bangladesh

<sup>2</sup>Department of Related Subjects, Barisal Engineering College, Barishal-8200, Bangladesh

Received: October 03, 2021, Revised: December 21, 2021, Accepted: December 23, 2021, Available Online: December 26, 2021

## ABSTRACT

Lorentz Transformation is the relationship between two different coordinate frames time and space when one inertial reference frame is relative to another inertial reference frame with traveling at relative speed. In this paper, we have derived the transformation formula for the volume charge density in Geometric Product Lorentz Transformation. The changes of volume charge density of moving frame in terms of that rest frame in Geometric Product Lorentz Transformation at various velocities and angles were studied as well.

Keywords: Lorentz Transformation (LT), Special Lorentz Transformation (SLT), Geometric Product Lorentz Transformation (GPLT), Volume Charge Density (VCD).



This work is licensed under a [Creative Commons Attribution-Non Commercial 4.0 International License](https://creativecommons.org/licenses/by-nc/4.0/).

## 1 Introduction

In most practice on special relativity [1], a straight line motion is along with x-axis. In this case (y, z) coordinate system are remained unchangeable under the Lorentz Transformations. However, in different cases line motion does not occur simultaneously with any of the coordinate axes. Volume charge density means amount of electric charge is existing in a certain volume [2]. Bhuiyan and Baizid [3] studied equation of transformation for surface charge density in different types of Lorentz Transformations. A static cube is been used to figure out the volume of charge density in Geometric Product Lorentz Transformation. Length is contracted in Lorentz Transformations. So, volume charge density will be different in different types of Lorentz Transformations. The objective of this article is to derive the transformation equations and volume charge density of a moving frame with reference to a static frame in Geometric Product Lorentz Transformation for various velocities and angles.

### 1.1 Special Lorentz Transformation (SLT)

Let  $S$  and  $S'$  be two inertial frame of references, here frame  $S$  is at rest and frame  $S'$  is moving through the velocity  $\vec{v}$  along x-axis with reference to the  $S$  frame. The time and space coordinates of  $S'$  and  $S$  are  $(x', y', z', t')$  and  $(x, y, z, t)$  respectively. SLT [1]-[9] which is said to be the relation between  $S$  and  $S'$ , can be obtained as follows

$$x' = \gamma(x - \vec{v}t) \tag{1}$$

$$y' = y \tag{2}$$

$$z' = z \tag{3}$$

$$t' = \gamma(t - \vec{v}x) \tag{4}$$

wherein to  $\gamma = (1 - \frac{v^2}{c^2})^{-\frac{1}{2}}$  and  $c = 1$ .

In addition to the inverse of SLT [1]-[9] can be obtained as

$$x = \gamma(x' + \vec{v}t') \tag{5}$$

$$y = y' \tag{6}$$

$$z = z' \tag{7}$$

$$t = \gamma(t' + \vec{v}x') \tag{8}$$

Wherein to  $\gamma = (1 - \frac{v^2}{c^2})^{-\frac{1}{2}}$  and  $c = 1$ .

### 1.2 Most General Lorentz Transformation (MGLT)

As the velocity  $\vec{v}$  of  $S'$  with reference to  $S$  is not aligned with x-axis, in such a situation velocity  $\vec{V}$  has three components  $V_x, V_y, V_z$  then MGLT [2-9], which is the relation between the coordinates of  $S'$  and  $S$ , can be obtained as follows

$$\vec{x}' = \vec{x} + \vec{V} \left[ \left\{ \frac{\vec{x} \cdot \vec{V}}{V^2} \right\} (\gamma - 1) - t\gamma \right] \tag{9}$$

$$t' = \gamma(t - \vec{x} \cdot \vec{V}). \tag{10}$$

Also the inverse of MGLT [2]-[9] can be obtained as

$$\vec{x} = \vec{x}' + \vec{V} \left[ \left\{ \frac{\vec{x}' \cdot \vec{V}}{V'^2} \right\} (\gamma - 1) + t'\gamma \right] \tag{11}$$

$$t = \gamma(t' + \vec{x}' \cdot \vec{V}) \tag{12}$$

wherein to  $\gamma = \frac{1}{\sqrt{1 - \frac{V^2}{c^2}}}$  and  $c = 1$ .

### 1.3 Geometric Product Lorentz Transformation (GPLT)

Let us consider the velocity  $\vec{v}$  of  $S'$  frame with reference to  $S$  frame. So the velocity  $\vec{v}$  has three components  $v_x, v_y, v_z$  as the MGLT. Let  $\vec{z}$  and  $\vec{z}'$  be the space part in  $S$  and  $S'$  frame respectively. According to the two vectors geometric product [3],[9]-[11], can be written as  $\vec{A}\vec{B} = \vec{A} \cdot \vec{B} + \vec{A} \times \vec{B}$  here  $\vec{A}$  and  $\vec{B}$  are two vectors and symbol  $\times$  is used as a replacement for the symbol  $\wedge$ .

The GPLT [3],[9]-[11] can be obtained as

$$\vec{z}' = \gamma\{\vec{z} - t\vec{v} - (\vec{z} \times \vec{v})\} \tag{13}$$

\*Corresponding Author Email Address: [ashrafal.mat5@gmail.com](mailto:ashrafal.mat5@gmail.com)

$$t' = \gamma(t - \vec{z} \cdot \vec{v}). \quad (14)$$

Also the inverse of GPLT [3],[9]-[11] can be obtained as

$$\vec{z} = \gamma\{\vec{z}' + t'\vec{v} + (\vec{z}' \times \vec{v})\} \quad (15)$$

$$t = \gamma(t' + \vec{z}' \cdot \vec{v}) \quad (16)$$

where about  $z'_x = x'$ ,  $z'_y = y'$ ,  $z'_z = z'$ ,  $z_x = x$ ,  $z_y = y$ ,  $z_z = z$ . Since  $\vec{v}$  has three components  $v_x$ ,  $v_y$ , and  $v_z$ . Hence the above transformations can also be obtained as

$$x' = \gamma\{x - tv_x - (yv_z - zv_y)\} \quad (17)$$

$$y' = \gamma\{y - tv_y - (zv_x - xv_z)\} \quad (18)$$

$$z' = \gamma\{z - tv_z - (xv_y - yv_x)\} \quad (19)$$

$$t' = \gamma\{t - xv_x - yv_y - zv_z\} \quad (20)$$

and

$$x = \gamma\{x' + t'v_x + (y'v_z - z'v_y)\} \quad (21)$$

$$y = \gamma\{y' + t'v_y + (z'v_x - x'v_z)\} \quad (22)$$

$$z = \gamma\{z' + t'v_z + (x'v_y - y'v_x)\} \quad (23)$$

$$t = \gamma\{t' + x'v_x + y'v_y + z'v_z\}. \quad (24)$$

## 2 Methods

We describe SLT and MGLT in section 1.1 and 1.2 respectively. Section 1.3 represents the space and time for moving frame and rest frame of Geometric Product Lorentz Transformation. We use volume charge density of section 3 to obtain transformation equation for VCD of moving frame in terms of that of rest frame in Geometric Product Lorentz Transformation in section 4.

## 3 Volume Charge Density (VCD)

The total amount of electric charge in one unit volume is said to be VCD which is designated by  $\sigma$ , where  $\sigma = \frac{q}{V}$ . It is calculated as coulombs per cubic meter ( $\frac{C}{m^3}$ ). VCD can take on negative values. Elementary charge  $e (=1.6 \times 10^{-19} \text{ coul})$  is formed in the minimum charge of proton or electron. It may decide that the electric charge is relativistically unchangeable because overall elementary charge is independent on the condition of the motion towards the viewer. On the basis of this discussion we can derive equation of transformation for VCD  $\sigma$  [3],[8].

## 4 Transformation of Geometric Product Lorentz Transformations

Let's consider two inertial frame  $S$  and  $S'$  where  $S'$  is moving through uniform velocity  $\vec{v}$  respect to the frame  $S$  along any arbitrary direction which is shown in Fig. 1. Therefore the velocity  $\vec{v}$  has three components  $v_x$ ,  $v_y$ , and  $v_z$ . Let's examine a uniform static cube having charge density  $+\sigma \text{ coul}/m^3$  at steady in frame  $S$  which one side is parallel to x-axis. Let's choose the cube edge length is  $R_0$ . The spectator in  $S'$  will detect that the cube is passing X-Y plane in opposed direction having velocity  $\vec{v}$  towards any random direction.

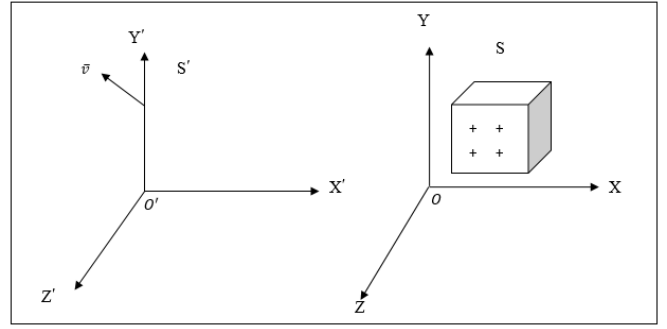


Fig. 1 X-Y plane having velocity  $\vec{v}$  in the  $S'$  frame with respect to the  $S$  frame.

If  $R_0$  is in  $S$  frame, then length of contraction for the GPLT in  $S'$  frame can be written as [12]

$$\vec{R}_0 = \gamma\{\vec{R} - (\vec{R} \times \vec{v})\}.$$

$$\text{Or, } R_0^2 = [\gamma\{\vec{R} - (\vec{R} \times \vec{v})\}]^2.$$

$$\begin{aligned} \text{Or, } R_0^2 &= \gamma^2\{R^2 - (\vec{R} \times \vec{v})^2 - \vec{R}(\vec{R} \times \vec{v}) - (\vec{R} \times \vec{v}) \cdot \vec{R} + (\vec{R} \times \vec{v}) \times (\vec{R} \times \vec{v})\} \\ &= \gamma^2\{R^2 + (Rv\sin\theta)^2\}. \end{aligned}$$

$$\text{Or, } R_0^2 = \gamma^2\{R^2 + R^2v^2(1 - \cos^2\theta)\}.$$

Considering  $R$  has three components  $R_x$ ,  $R_y$ , and  $R_z$ .

$$\text{Or, } R^2 = \frac{R_0^2}{\gamma^2\{1+v^2(1-\cos^2\theta)\}}.$$

$$\text{Or, } R_x^2 + R_y^2 + R_z^2 = \frac{R_{0x}^2 + R_{0y}^2 + R_{0z}^2}{\gamma^2\{1+v^2(1-\cos^2\theta)\}}.$$

$$R_x^2 = \frac{R_{0x}^2}{\gamma^2\{1+v^2(1-\cos^2\theta)\}}.$$

$$R_y^2 = \frac{R_{0y}^2}{\gamma^2\{1+v^2(1-\cos^2\theta)\}}.$$

$$R_z^2 = \frac{R_{0z}^2}{\gamma^2\{1+v^2(1-\cos^2\theta)\}}.$$

Therefore total charge detected by a spectator in the  $S'$  frame is

$$Q' = R_x R_y R_z \sigma'.$$

$$\text{Or, } Q' = \left(\frac{R_{0x}^2}{\gamma^2\{1+v^2(1-\cos^2\theta)\}}\right)^{\frac{1}{2}} \times$$

$$\left(\frac{R_{0y}^2}{\gamma^2\{1+v^2(1-\cos^2\theta)\}}\right)^{\frac{1}{2}} \times \left(\frac{R_{0z}^2}{\gamma^2\{1+v^2(1-\cos^2\theta)\}}\right)^{\frac{1}{2}} \sigma'.$$

$$\text{Or, } Q' = \frac{R_0^3}{[\gamma^2\{1+v^2(1-\cos^2\theta)\}]^{\frac{3}{2}}} \sigma'.$$

Following the law of conservation of charge  $Q' = Q_0$

$$\text{Or, } \frac{R_0^3}{[\gamma^2\{1+v^2(1-\cos^2\theta)\}]^{\frac{3}{2}}} \sigma' = R_0^3 \sigma.$$

$$\text{Or, } \sigma' = \sigma[\gamma^2\{1 + v^2(1 - \cos^2\theta)\}]^{\frac{3}{2}}.$$

This is the equation of transformation for volume charge density in Geometric Product Lorentz Transformations.

**5 Results and Discussion**

Table 1 Space, time, and transformation equation for volume charge density in Geometric Product Lorentz Transformations.

Length of Contraction	$\vec{R}_0 = \gamma\{\vec{R} - (\vec{R} \times \vec{v})\}$
Volume Charge Density	$\sigma' = \sigma[\gamma^2\{1 + v^2(1 - \cos^2\theta)\}]^{\frac{3}{2}}$
Space	$x' = \gamma\{x - tv_x - (yv_z - zv_y)\}$ $y' = \gamma\{y - tv_y - (zv_x - xv_z)\}$ $z' = \gamma\{z - tv_z - (xv_y - yv_x)\}$
Time	$t = \gamma\{t' + x'v_x + y'v_y + z'v_z\}$

**5.1 Graphical Depiction of VCD in GPLT**

Volume charge density in moving frame in terms of rest frame indicates black color, red color, and blue color straight line for respective volume 0.2 c, 0.4 c, and 0.6 c in Fig. 2-Fig. 5 where speed of light, c = 300,000 km/sec.

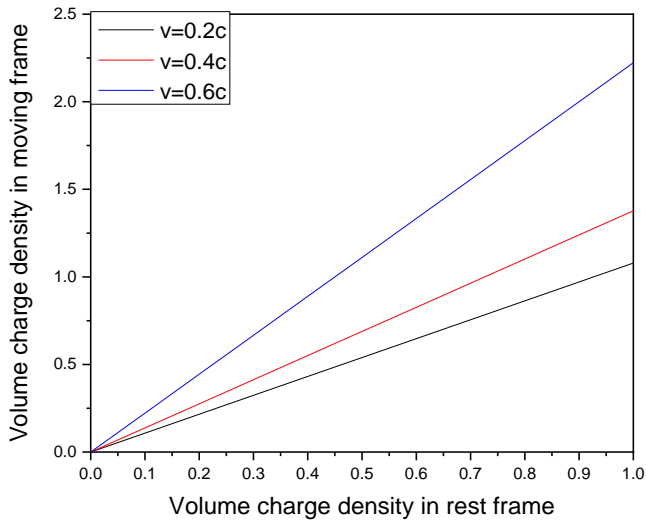


Fig. 2 VCD in GPLT at 30 degree angle

In Fig. 2, VCD in moving frame increases with volume rising for same 30 degree angle. It is clear that black color straight line below than all other straight line and blue color straight line upwarded among all. Moreover, we can see that only black color straight line is observing strictly at 30 degree angle.

In Fig. 3, VCD in moving frame rises with volume increasing for same 45 degree angle. It is notable that black color straight line under than all other straight line and blue line color straight line upstairs among all. Furthermore, we can realize that only blue color straight line is observing firmly at 45 degree angle.

In Fig. 4, VCD in moving frame at 60 degree angle performs as like as for 45 degree angle. Additionally, we can observe that only blue color straight line is observing conclusively at 60 degree angle.

In Fig. 5, VCD in moving frame at 75 degree angle acts as like as for 30 degree angle. Additionally, we can notice that no color straight line is observing decisively at 75 degree angle.

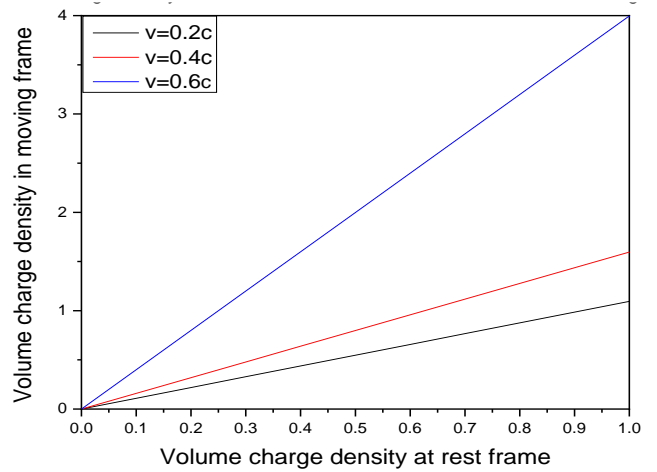


Fig. 3 VCD in GPLT at 45 degree angle

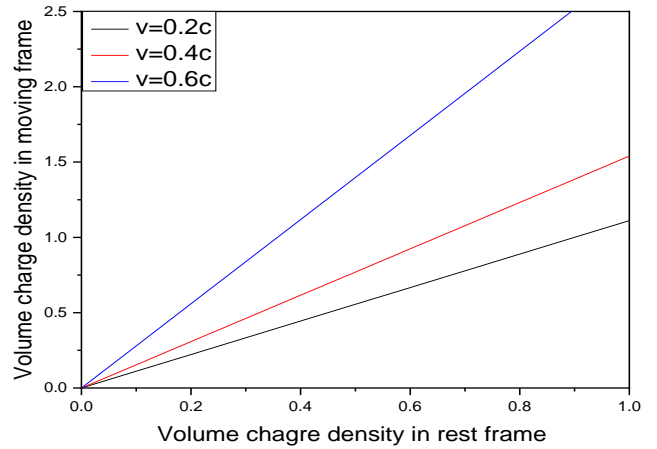


Fig. 4 VCD in GPLT at 60 degree angle

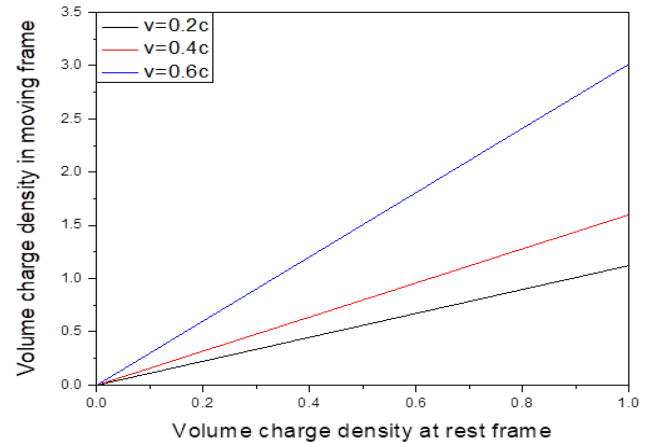


Fig. 5 VCD in GPLT at 75 degree angle

**6 Conclusion**

In special relativity, space-time is mainly four dimensional and time cannot be disconnected from three dimensional spaces. The space-time and transformation equation for volume charge density in Geometric Product Lorentz Transformation is displayed in Table 1. Volume charge density based numerical values of Geometric Product Lorentz Transformation for a moving frame with reference to a static frame have been carried out and graphically it is observed that for same angles the value of the VCD for a moving frame increases with the rise of velocity of the moving frame itself.

## References

- [1] Resnick, R., 1994. *Introduction to Special Relativity*. John Wiley & Sons, USA, ISBN: 978-0-471-71725-6.
- [2] Bhuiyan, S.A. and Baizid, A.R., 2016. Volume Charge Density in Most General Lorentz Transformation. *Journal of Scientific Research*, 8(3), pp.259-265.
- [3] Bhuiyan, S.A. and Baizid, A.R., 2015. Surface Charge Density in Different Types of Lorentz Transformations. *Applied Mathematics*, 5(3), pp.57-67.
- [4] Bhuiyan, S.A., 2019. Volume Charge Density in Mixed Number Lorentz Transformation. *Journal of Scientific Research*, 11(2), pp.209-214.
- [5] Moller, C., 1972. *The Theory of Relativity*. Oxford University Press, London, UK.
- [6] Prakash, S., 1993-1994. *Relativistic Mechanics*. Pragati Prakashan.
- [7] Baizid, A.R. and Alam, M.S., 2012. Applications of different Types of Lorentz Transformations. *American Journal of Mathematics and Statistics*, 2(5), pp.153-163.
- [8] Rafiq, S.B. and Alam, M.S., 2012. Transformation of Surface Charge Density in Mixed Number Lorentz Transformation. *Sri Lankan Journal of Physics*, 13(1), pp.17-25.
- [9] Baizid, A. and Alam, M., 2014. Reciprocal Property of Different Types of Lorentz Transformations. *International Journal of Reciprocal Symmetry and Theoretical Physics*, 1(1), pp.19-35.
- [10] Datta, B.K., De Sabbata, V. and Ronchetti, L., 1998. Quantization of gravity in real space-time. *Nuovo Cimento. B*, 113(6), pp.711-732.
- [11] Datta, B.K., Datta, R. and De Sabbata, V., 1998. Einstein field equations in spinor formalism: a clifford-algebra approach. *Foundations of Physics letters*, 11(1), pp.83-93.
- [12] Alam, M.S., Begum, K., 2009. Different Types of Lorentz Transformations, *Jahangirnagar Phy. Stud.* 15.

# Predicting Retinal Diseases using Efficient Image Processing and Convolutional Neural Network (CNN)

Asif Mohammad, Mahruf Zaman Utso, Shifat Bin Habib, Amit Kumar Das\*

Department of Computer Science and Engineering, East West University, Dhaka, Bangladesh

Received: October 20, 2021, Revised: December 21, 2021, Accepted: December 22, 2021, Available Online: December 27, 2021

## ABSTRACT

Neural networks in image processing are becoming a more crucial and integral part of machine learning as computational technology and hardware systems are advanced. Deep learning is also getting attention from the medical sector as it is a prominent process for classifying diseases. There is a lot of research to predict retinal diseases using deep learning algorithms like Convolutional Neural Network (CNN). Still, there are not many researches for predicting diseases like CNV which stands for choroidal neovascularization, DME, which stands for Diabetic Macular Edema; and DRUSEN. In our research paper, the CNN (Convolutional Neural Networks) algorithm labeled the dataset of OCT retinal images into four types: CNV, DME, DRUSEN, and Natural Retina. We have also done several preprocessing on the images before passing these to the neural network. We have implemented different models for our algorithm where individual models have different hidden layers. At the end of our following research, we have found that our algorithm CNN generates 93% accuracy.

Keywords: Retinal Disease, Deep Learning, Image Processing, Neural Network, Convolutional Neural Network.



This work is licensed under a [Creative Commons Attribution-Non Commercial 4.0 International License](https://creativecommons.org/licenses/by-nc/4.0/).

## 1 Introduction

Drum Scanner is the first scanner which is developed for use with a computer [1]. Since then the technology has advanced day by day, and lots of technology for scanning and loading pictures on a computer are available. With the availability of these technologies, researchers started to build and develop systems to analyze these images. The advancement of the image processing system is still going on in the present time, and it progressed from a ruled-formed method to a machine learning procedure. Even now, Machine learning methods take part in a prominent role [2]. Experts mostly write the features in hand used in machine learning algorithms, which is one of the significant drawbacks of machine learning approaches. For image processing, the algorithm needs to be created, which will be able to extract features and complete calculations. This is where a deep learning method is applied in image processing. For the availability of vast amounts of imagery data, ANN and CNN deep learning algorithms play a prominent role [3]-[6].

Because of advanced technology, medical researchers can take more precise images of x-ray and inner organs than before. That is why vast amounts of image data are generated in x-ray and other image reports. Deep learning techniques are critical for dealing with such massive amounts of data. Deep learning algorithms are used in numerous branches of medical study that are related to retinal sickness prognosis [7], Cancer prognosis [8], abdominal and musculoskeletal prognosis [9].

The deep learning technique is a machine learning approach in which various neural networks are implied for prognosis and categorization. Deep learning is used over massive imagery datasets for prediction and classification. Critical neural networks used in large imagery datasets are the ANN, CNN, RNN, and LSTM [10]-[12]. Some basic concepts of neural networks will be talked about below. Neurons are considered the modeling chunks of a neural network that looks like organic neurons in the interior of our brain. There are three distinct layers

(input layer, hidden layer, and output layer). Input layer's each neuron extracts a sole attribute from the dataset and gives it to the hidden layer. Hidden layer's every neuron is attached to a former layer and preceding layer along with weights. When the hidden layer neuron gets the former layer's signal, each neuron is multiplied by the correlated weights. Then the multiplications of each neuron are added and then given to the activation function to find if the hidden layer neuron will roll the signal to the next layer or not. The architecture of neural networks is shown in Fig. 1.

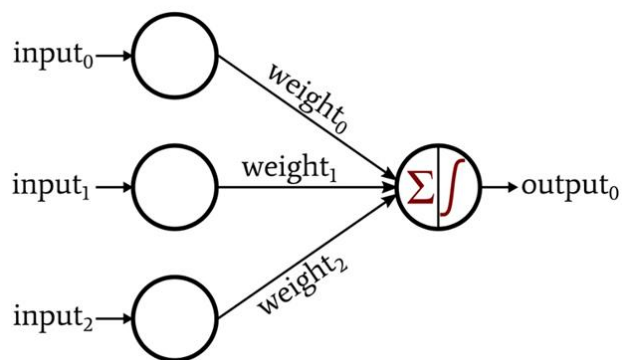


Fig. 1 The simple architecture of neural networks [13].

The weights of the neurons are assigned randomly at the beginning. Then during the training of the datasets, the value of the weight gets updated. In this way, neural networks learn to differentiate one object from another. The number of hidden layers used in neural networks plays a vital role in classification and regression. Various hidden layers are used in a model, and the optimal result is selected. The backpropagation technique is popular in neural networks for supervised learning, making deep learning more popular nowadays. This technique helps a machine learn distinct features from the datasets without the intervention of humans.

Retinal disease is one of the common diseases in the present time. With the advancement of medical technology and computational science, many learning techniques are being invented for predicting and classifying disease accurately. As a substantial medical image database is available, deep learning techniques are becoming more suitable for classification and prediction [14]. Among deep learning approaches, CNN was used for our research paper to process the retinal images and categorize those different images into different disease classes.

Our research paper aims to develop and implement a deep learning model called CNN (Convolutional Neural Networks) to predict and label retinal illness by perceiving retinal pictures with higher reliability.

In medical research, retinal disease is one of the crucial sectors. The medical hardware is advancing day by day. With its advancement, a massive amount of imagery medical datasets are available in which doctors can take more explicit retinal images and other organ images. Deep learning technology is becoming popular for classification and prediction for the enormous medical imagery dataset. There are many pieces of research in which deep learning techniques were introduced to predict and classify retinal diseases. More and more research is also developing in which deep learning approaches are used to improve prediction and classification accuracy.

## 2 Literature Review

Several research papers include image datasets and deep learning algorithm techniques. In one research paper [15], the author examined RNFL (Retinal Nerve Fiber Layer) width and VF (Visual Field) and fetched some candidate attributes for the glaucoma prediction model. After that, the paper's author developed synthesized features and selected the most pleasing attributes for categorization (diagnosis) by implying feature evaluation. Then, the paper implemented machine learning approaches that are C5.0, Random Forest, SVM, and KNN. The dataset includes 100 cases of data for testing and 399 cases of data for training. Being a small dataset causes drawbacks as deep learning techniques need a vast dataset to predict precision.

The research paper [16] implied CNN deep learning approach to perceive Glaucomatous Optic Neuropathy by observing color fundus pictures. The size of the dataset of that particular paper is 48,000 images. The paper's author labeled the data with the help of experts and then applied CNN deep learning to categorize the pictures. This paper was one of the inspirational papers for our research as we processed a much larger dataset and used convolutional neural networks (CNN) after processing.

CNN is applied to perceive diabetic retinopathy by observing fundus images of the retina in another research paper [17]. The dataset size is 127125 images of the retina, which 54 licensed ophthalmologists grade. Nevertheless, they focused on only one sickness and used the fundus picture dataset, unlike our research's OCT image datasets.

Multiple classifications of retinal diseases are discussed in another note-worthy paper [18]. These diseases include AMRD, diabetic eye diseases, etc. To classify images into different image category the author of the paper used deep CNN and SVM classifiers. In the end, the author discussed the difficulties of the classification for the likelihood of the disease.

OCT images were used to categorize pictures into a distinct class of diseases in Ref. [19]. Here CNN is also implied, and the outcome is compared with the human ophthalmology experts categorizing these sicknesses. In another study [20], a deep learning technique was used to predict Age-related macular

degeneration (AMD). The dataset size for this paper color fundus pictures of 120,656 pictures in which 13 categories were represented for prediction. The research paper's authors have tried various combinations of convolutional neural networks among different deep learning algorithms. Nonetheless, images are classified into only one sickness, and fundus pictures were used for this research's dataset.

A convolutional neural network (CNN) was used in another research paper [21] to detect eye glaucoma eye disease on retinal fundus imaging. The dataset size of that paper was 1200 retinal images. In this research paper, an unsupervised convolutional neural network (CNN) was used to draw out the features from raw images. Then the author of the research paper applied the DBN technique to the extracted attributes by CNN to detect the optimal finest feature for the implementation in this research. And lastly, the softmax linear classifier was used to differentiate between two classes, glaucoma and not glaucoma. Like the previous paper, fundus images were used as datasets, and the images were classified into only one disease.

Deep Learning was also used by the researchers [22] to assess cardiovascular risk factors from retinal fundus photographs. The research paper's authors have trained 284,335 patients on a dataset and validated their findings into two separate datasets. The size of the one separate dataset contains the data of 12,026 patients, and another separate dataset contains the data of 999 patients. Besides their excellent results, we think it would be better to use a larger dataset for more accurate validation findings. In a review paper [23] researchers discussed different deep learning approaches that can cause prognosis diabetic retinopathy in a person's retina. Other authors' papers discuss how deep learning algorithms are used to generate better prediction values. This paper is not that type of research paper where the authors launch a new model and attempt to attest their claim, but it can be helpful for further deep learning algorithm research. In Ref. [24] the authors applied deep learning approaches to predict diabetic retinopathy in the retina. The dataset for this research is collected from 1612 diabetic patients, which contains 1796 retinal fundus pictures. Nevertheless, we think that dataset size is small-scaled as deep learning algorithms need a larger dataset for more accurate results.

In another paper [25], deep learning was used on OCT images for Macular fluid's fully automated method for detecting and quantifying. The author's method based on a deep learning algorithm automatically detects IRC (Intraretinal cystoid) fluid and SRF (Subretinal) fluid. The dataset size for this research paper is 1200 volumes of OCT images.

In Ref. [26] we can see the discussion about the detection of diabetic retinopathy of different ethnicities of diabetic patients. The author used various deep learning algorithms for this detection and used a vast dataset of 494661 retinal images. They classified the image data into different ethnicities as people from different corners of the world have different food habits, and food habit is the primary concern on maintaining diabetes. This paper is different from other papers because it focuses on different ethnicities, which draws a different aspect.

In Ref. [27] the researchers applied CNN and ANN in 84,494 image datasets to predict retinal diseases and compared each algorithm predicting accuracy. This paper is such an inspiration to us. However, we applied only convolutional neural networks (CNN) to the same dataset. Still, we have better-predicting accuracy for different image processing approaches and other convolutional neural networks (CNN) algorithm implementation systems.

### 3 Methodology

To classify the diseases, we have used a Convolutional Neural Network (CNN), an artificial neural network that is very popular for organizing dataset images [28]-[29]. Our dataset contains a total of 84,484 images. These images are in Optical Coherence Tomography (OCT) form. We have divided our dataset into three categories: 80% for training, 15% for validation, and 5% for test. In the following steps, we have explained our research procedure in detail. Then we have also explained in a flowchart.

#### 3.1 Input Data

First, we have imported our dataset into the model. In our dataset, images are organized into four different categories. Three represent a particular disease, and the remaining one category represents normal no-disease.

#### 3.2 Preprocessing

##### 3.2.1 Removing Duplicate Images

Our dataset had a total of 7676 identical images. We have removed those images from the dataset to make our prediction and algorithm learning unbiased. Repeating the same image may affect the learning of our algorithm.

##### 3.2.2 Filling Up Blank Spaces

Some images had empty spaces by the border areas. We have filled up those empty spaces with the same background color, which happens to be black in our images. Filling up blank spaces of the images helps to make the images of our dataset consistent.

##### 3.2.3 Image Resizing

Image resizing is an essential process in deep learning models. Models train faster if they are fed smaller images. Smaller images have more computational advantages compared to larger images. Also, many deep learning models require the image to be the same size. In our case, we have resized the images into 200x200 sizes. Resizing them any smaller can lead us to information loss. On the other hand, larger images might also negatively affect our model regarding power drain and production time.

##### 3.2.4 Image Blurring

Image blurring is often used in image classifications before inserting the image model to reduce unnecessary noises in the data. When we work with image datasets, we see pictures with various attributes. Some images will have too much noise. Image blurring is applied to collect data from these noisy images. Blurring will help to remove noises from those images. We have used total variation filtering, a noise removal process, to denoise the dataset. But we have to maintain it carefully because if we blur the image too much, we will lose necessary information from the images. Here in Fig. 2, the demonstration of the Image Blurring process is shown.

##### 3.2.5 Image Standardization

Standardization is an important technique used as a preprocessing step. When it comes to pictures, the input data set features significant differences between their ranges. These differences in the ranges of elements can cause trouble for many

machine learning models. We have used standardization techniques to scale the pixel values of the images.

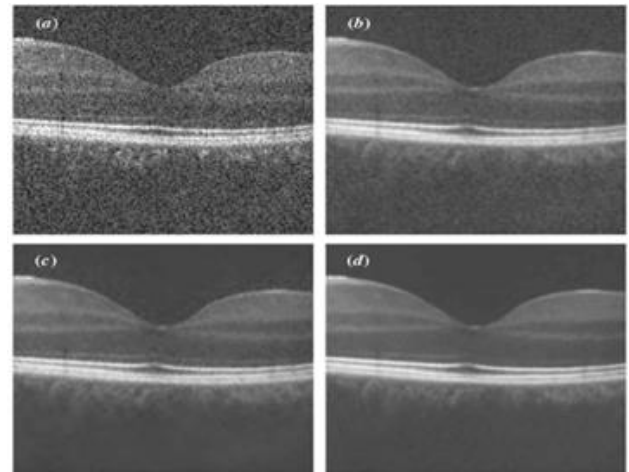


Fig. 2 Image Blurring process [30].

### 3.3 Image Recognition

#### 3.3.1 Architecture of the Proposed Model

Deep Learning is becoming the primary tool for problems that try to understand images, human voice, and robots. With our dataset, our main target is the implementation of CNN for recognizing images.

The primary purpose of our proposed model is to have a proper grasp of CNN and customize the algorithm for recognizing images for the dataset.

CNN uses filters to bring out the feature maps from 2D pictures. It considers mapping image pixels with the neighborhood space instead of fully connected neuron layers. CNN has become an innovative and vastly acclaimed algorithm for processing images. It is also gaining attention in recognizing handwriting, object classifications, and computer vision. It is becoming a better option than others.

When someone begins to gather ideas about deep learning and neural networks, the Convolutional Neural Network (CNN) is one of the most used deep learning techniques.

The primary purpose of designing CNN is to find visual patterns straight from pictures with as low preprocessing as possible. Most CNNs try to apply convolutional layers to the input. By raising the feature map's quantity, CNN also down-samples the spatial dimensions called max pooling.

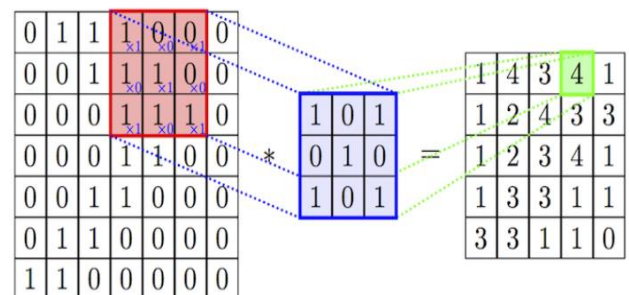


Fig. 3 Convolution Operation [31].

However, convolutional, pooling, and fully connected layers are the most significant among all the operations of CNN. Therefore, we would like to present these layers before introducing our proposed model.

The first layer extracts features from the images, the Convolutional layer. The convolution preserves the connection among different parts of a picture. It happens because one single pixel is only connected to the adjacent and closest pixel. Also, convolution filters the picture with a smaller pixel filter to bring down the picture size so that it does not lose the relationship between pixels. For example, if convolution is applied to a 7x7 image and if we use a filter of size 3x3, which has a 1x1 stride, it will be a 5x5 output. Convolution Operation Demonstrated in Fig. 3.

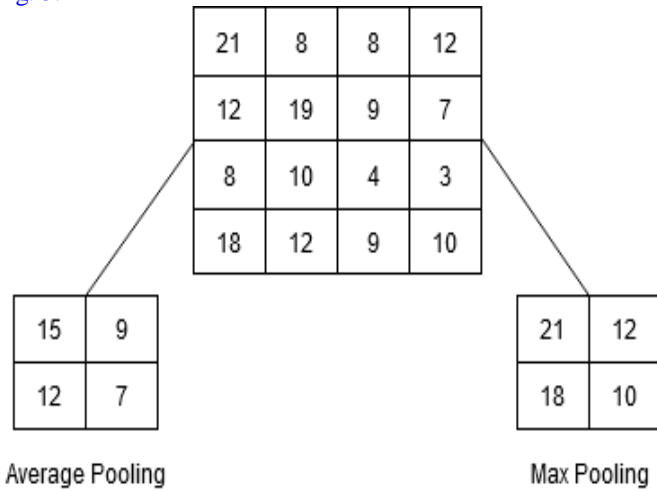


Fig. 4 Max pooling and Average pooling operation.

Inserting pooling layers after every convolution layer is a common practice. We do this while constructing CNN to

decrease the size of the actual representation. This layer reduces the counts of the parameter. By doing that, also helps to reduce the computational complexity. Moreover, when it comes to overfitting problems, pooling layers try to solve them. We try to find the maximum, average, or sum values inside the pixels. To reduce the parameters count. We also select a pooling size. Max pooling and Average pooling operation Demonstration shown in Fig. 4.

If every neuron in one layer connects to every neuron in the next layer in an artificial neural network, it can be identified as a fully connected neural network.

We can decrease time-space complexity by a significant margin if we use pooling and convolutional layers. After doing all this, a fully connected network can be built to classify the images.

3.3.2 Explanation of the models

Fig. 5 shows the structures of our proposed CNN models. The first layer of each model gets the preprocessed image as the input of size 200\*200. Each conv2D layer has filter size 3\*3 with stride 1, padding='same', and activation function 'ReLU' (Rectified Linear Unit). The number of filters is mentioned in Fig. 5.

We have used (2\*2) max-pooling layers with a string of 2. The dropout rate is set to 0.2.

Because our dataset is unbalanced, we have utilized class weight. This dictionary maps class indices to a weight value that may be used to urge the model to "pay more attention" to samples from an under-represented class. Equation (1) shows the used formula to determine the weights of the corresponding classes.

$$Weight\ of\ a\ class = \frac{number\ of\ samples}{num\ of\ unique\ class * number\ of\ samples\ in\ corresponding\ class} \tag{1}$$

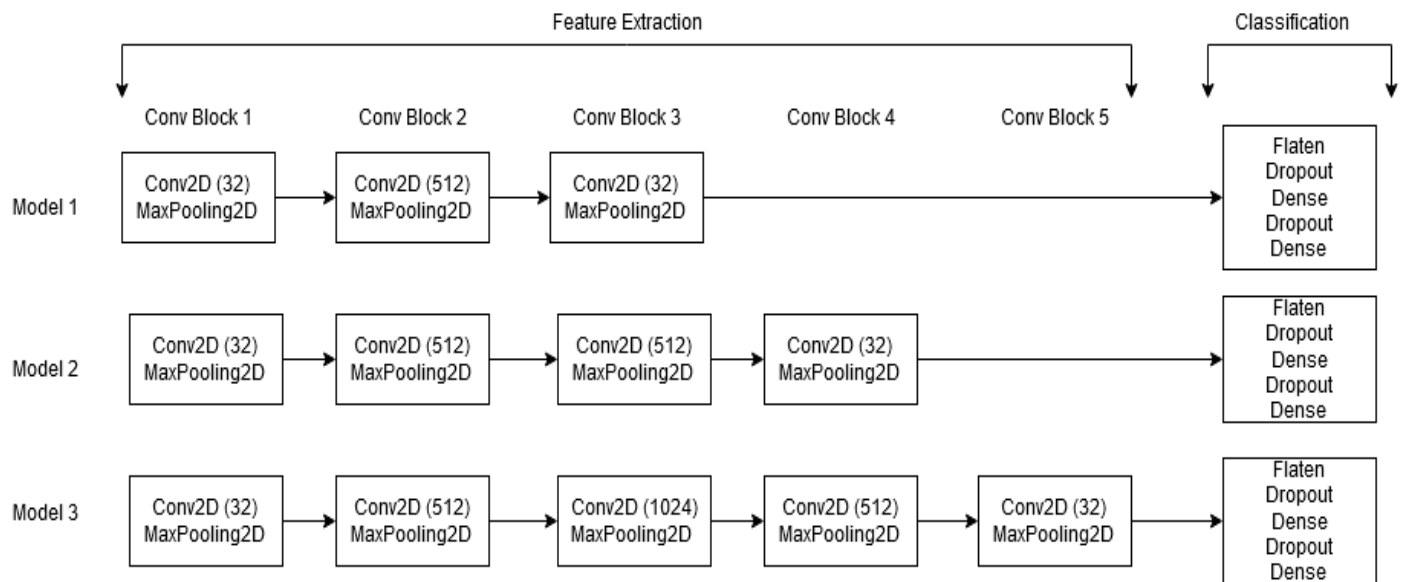


Fig. 5 CNN Model Structures.

## 4 Results and Discussion

### 4.1 Dataset Description

The dataset of our research paper [32] consisted of 84,495 numbers of OCT (Optical Coherence Tomography) pictures of the retina. Four categories separate these pictures. They are CNV, DME, DRUSEN, and normal retinal pictures.

The images of this dataset were taken from five institutes. The institutes are

1. Beijing Tongren Eye Center, Beijing.
2. The Shanghai First People's Hospital, Shanghai
3. MCOA,
4. CRRF, California, USA
5. Shiley Eye Institute, San Diego, USA

There are three disease categories and one normal category in five categories in the dataset. The disease categories are shortly discussed below:

**CNV:** CNV stands for choroidal neovascularization disease, which arises on the retina. This disease causes the massive growth of new vessels which carry blood in the choroid, a layer under the retina. Unlike normal vessels and occasionally red blood cells, new vessels let fluids from the blood.

**DME:** DME stands for Diabetic Macular Edema retinal disease, which transpires due to fluid leaking in the Macular's retina part. This disease generally arises in diabetic patients. It can damage blood vessels in the retina. This disease has to be treated within a certain time; otherwise, the eye can be damaged.

**DRUSEN:** the white or yellow-colored spots that transpire in the Bruch's membrane named retinal layer can be identified as DRUSEN. There can be several causes of this disease, and one of the common causes is gathering waste products from rods and cones. If this disease is not treated within a particular time, it can cause permanent blindness.

Our research studied different layers to discover the optimal CNN algorithm model. Here, features of this particular algorithm were selected by the algorithm's built-in nature.

The prediction quality was measured into four rates: accuracy, sensitivity, specificity, and precision by using 3, 4, 5, vgg16, and vgg19 layer models. Here Eqs. (2) - (5) are used to calculate accuracy, precision, sensitivity and specificity [33]-[37].

$$Accuracy = \frac{Predicted\ correctly}{Number\ of\ total\ images} \quad (2)$$

$$Sensitivity = \frac{True\ Positive}{True\ Positive + False\ Negative} \quad (3)$$

$$Specificity = \frac{True\ Negative}{True\ Negative + False\ Negative} \quad (4)$$

$$Precision = \frac{True\ Positive}{True\ Positive + False\ Positive} \quad (5)$$

In Table 1, we can see that all 3, 4, 5, vgg16, and vgg19 layers are almost close in forms of accuracy, sensitivity, specificity, and precision in percentage. When we observe precisely, we can see that the five hidden layer model gives the highest accuracy (93.26%), sensitivity (93%), specificity (97%), and precision (93%), and the vgg16 model provides the lowest accuracy (90.02%) and sensitivity (90%), specificity (94%). The hidden layer models 3, 4, vgg16, and vgg19 have the same precision (92%).

Table 1 Different Hidden Layer models of Convolutional Neural Network (CNN) comparison.

Hidden Layer	Accuracy	Sensitivity	Specificity	Precision
3	91.52	92	96	92
4	91.57	92	96	92
5	93.26	93	97	93
Vgg16	90.02	90	94	92
Vgg19	91.91	92	96	92

Table 2 Comparison of Different Hidden Layer model of Convolutional Neural Network (CNN) to accurately predict disease.

Hidden Layer	CNV	DME	DRUSEN	Normal
3	90.98	87.23	82.98	96.47
4	93.35	86.68	82.2	94.25
5	92.07	92.15	85.34	97.47
Vgg16	89.51	93.07	85.86	90.57
Vgg19	95.33	89.42	70.42	95.17

CNN Model With Different Hidden Layers

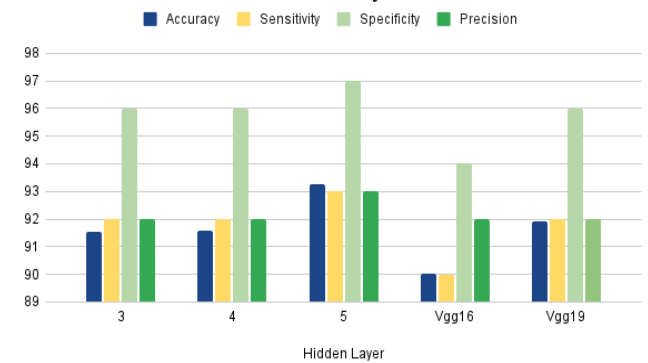


Fig. 6 Comparison of Different Hidden Layer model of Convolutional Neural Network (CNN) in terms of accuracy, sensitivity, specificity, and precision.

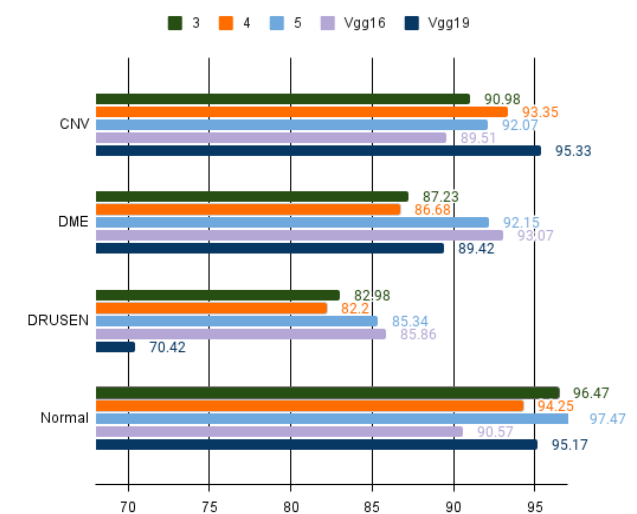


Fig. 7 Comparison of Different Hidden Layer model of Convolutional Neural Network (CNN) to accurately predict disease.

Also, if we carefully compare all the hidden layers, we will see a pattern of increment in accuracy, sensitivity, specificity, and precision among hidden layers 3, 4, and 5. It indicates that five hidden layers were more effective than 3 and 4 layers. Even between Vgg16 and Vgg19, Vgg19 showed better results than vgg16. We also measured the prediction accuracy in CNV, DME, DRUSEN disease, and regular eye prediction for 3, 4, 5, vgg16, and vgg19 layer models.

In Table 2, we can observe that the vgg19 layer model gives the highest accuracy for CNV disease prediction (95.33%). The vgg16 layer model offers the best accuracy (93.07%). In the case of DRUSEN disease prediction, the vgg16 layer model provides the best accuracy (85.86%). The 5 layer model gives the best accuracy (97.47%). Here Fig. 6 and Fig. 7 are the graphical representation of what is shown in Table 1 and Table 2.

In [27], research on the same dataset was conducted. They also used convolutional neural networks. In their paper, a model with four hidden layers produces the best result among all. Their four hidden layer model shows an accuracy score of 86.71. In contrast, our created five hidden layer model shows an accuracy score of 93.26. Their sensitivity, specificity, and precision scores are 85.04, 86.08, and 85.41, respectively, with four hidden layers. Our model's sensitivity, specificity, and precision scores are 93, 97, and 93, with five hidden layers.

## 5 Conclusion

In the forms of data analysis and data prediction, machine learning algorithms have surpassed all statistical models in the present time. But with the increasing amount of data, the limitations of the machine learning algorithms became clearer. That is the time the deep learning algorithm stepped up. Deep learning algorithms can select features independently and perform complex non-linear equations even though these algorithms are machine learning algorithms. For that reason, deep learning algorithms have taken up machine learning algorithms in various fields. Convolutional Neural Networks (CNN) dominate in the image processing sector.

The medical sector generates a massive quantity of image data, like ophthalmology. With this vast amount of imagery data, researchers used deep learning algorithms to predict diseases that might happen in our eyes. We inspired those research papers and applied Convolutional Neural Network (CNN) to separate three retinal diseases from normal vision.

Nevertheless, in the future, we would like to develop the algorithm to get more accuracy and also would like to apply other deep learning algorithms to compare and observe whether it performs better than Convolutional Neural Network (CNN) or not. Moreover, we can think of learning techniques that may be unsupervised in the future to see whether it surpasses convolution neural deep learning algorithms or not. Lastly, we would like to apply the same approach to other imagery datasets available for medical sectors and in other sectors where massive image datasets are used to classify and predict.

## References

- [1] Kantengwa, S., 2020. *Origin of ordinary things: Scanner*. The New Times, accessed 12 October 2021, Website: <https://www.newtimes.co.rw/lifestyle/origin-ordinary-things-scanner>
- [2] Litjens, G., Kooi, T., Bejnordi, B.E., Setio, A.A.A., Ciompi, F., Ghafoorian, M., Van Der Laak, J.A., Van Ginneken, B. and Sánchez, C.I., 2017. A survey on deep learning in medical image analysis. *Medical Image Analysis*, 42, pp.60-88.
- [3] Islam, J., Mubassira, M., Islam, M.R. and Das, A.K., 2019, February. A speech recognition system for Bengali language using recurrent neural network. In *2019 IEEE 4th international conference on computer and communication systems (ICCCS)* (pp. 73-76). IEEE.
- [4] Mumu, T.F., Munni, I.J. and Das, A.K., 2021. Depressed people detection from bangla social media status using lstm and cnn approach. *Journal of Engineering Advancements*, 2(01), pp.41-47.
- [5] Hossain, M.T., Hasan, M.W. and Das, A.K., 2021, January. Bangla Handwritten Word Recognition System Using Convolutional Neural Network. In *2021 15th International Conference on Ubiquitous Information Management and Communication (IMCOM)* (pp. 1-8). IEEE.
- [6] Das, A.K., Ashrafi, A. and Ahmmad, M., 2019, February. Joint cognition of both human and machine for predicting criminal punishment in judicial system. In *2019 IEEE 4th International Conference on Computer and Communication Systems (ICCCS)* (pp. 36-40). IEEE.
- [7] De Fauw, J., Ledsam, J.R., Romera-Paredes, B., Nikolov, S., Tomasev, N., Blackwell, S., Askham, H., Glorot, X., O'Donoghue, B., Visentin, D. and van den Driessche, G., 2018. Clinically applicable deep learning for diagnosis and referral in retinal disease. *Nature Medicine*, 24(9), pp.1342-1350.
- [8] Xiao, Y., Wu, J., Lin, Z. and Zhao, X., 2018. A deep learning-based multi-model ensemble method for cancer prediction. *Computer Methods and Programs in Biomedicine*, 153, pp.1-9.
- [9] Weston, A.D., Korfiatis, P., Kline, T.L., Philbrick, K.A., Kostandy, P., Sakinis, T., Sugimoto, M., Takahashi, N. and Erickson, B.J., 2019. Automated abdominal segmentation of CT scans for body composition analysis using deep learning. *Radiology*, 290(3), pp.669-679.
- [10] Rakib, O.F., Akter, S., Khan, M.A., Das, A.K. and Habibullah, K.M., 2019, December. Bangla word prediction and sentence completion using GRU: an extended version of RNN on N-gram language model. In *2019 International Conference on Sustainable Technologies for Industry 4.0 (STI)* (pp. 1-6). IEEE.
- [11] Das, A.K., Al Asif, A., Paul, A. and Hossain, M.N., 2021. Bangla hate speech detection on social media using attention-based recurrent neural network. *Journal of Intelligent Systems*, 30(1), pp.578-591.
- [12] Hossain, M.M., Labib, M.F., Rifat, A.S., Das, A.K. and Mukta, M., 2019, June. Auto-correction of english to bengali transliteration system using levenshtein distance. In *2019 7th International Conference on Smart Computing & Communications (ICSCC)* (pp. 1-5). IEEE.
- [13] Bombini, A., 2019. *Using CNN to classify images w/PyTorch, Kaggle*. accessed 12 October 2021, Website: <https://www.kaggle.com/androbomb/using-cnn-to-classify-images-w-pytorch>
- [14] Ker, J., Wang, L., Rao, J. and Lim, T., 2017. Deep learning applications in medical image analysis. *Ieee Access*, 6, pp.9375-9389.

- [15] Kim, S.J., Cho, K.J. and Oh, S., 2017. Development of machine learning models for diagnosis of glaucoma. *PLoS one*, 12(5), p.e0177726.
- [16] Lee, C.S., Baughman, D.M. and Lee, A.Y., 2017. Deep learning is effective for classifying normal versus age-related macular degeneration OCT images. *Ophthalmology Retina*, 1(4), pp.322-327.
- [17] Gulshan, V., Peng, L., Coram, M., Stumpe, M.C., Wu, D., Narayanaswamy, A., Venugopalan, S., Widner, K., Madams, T., Cuadros, J. and Kim, R., 2016. Development and validation of a deep learning algorithm for detection of diabetic retinopathy in retinal fundus photographs. *Jama*, 316(22), pp.2402-2410.
- [18] Arunkumar, R. and Karthigaikumar, P., 2017. Multi-retinal disease classification by reduced deep learning features. *Neural Computing and Applications*, 28(2), pp.329-334.
- [19] Kermany, D.S., Goldbaum, M., Cai, W., Valentim, C.C., Liang, H., Baxter, S.L., McKeown, A., Yang, G., Wu, X., Yan, F. and Dong, J., 2018. Identifying medical diagnoses and treatable diseases by image-based deep learning. *Cell*, 172(5), pp.1122-1131.
- [20] Grassmann, F., Mengelkamp, J., Brandl, C., Harsch, S., Zimmermann, M.E., Linkohr, B., Peters, A., Heid, I.M., Palm, C. and Weber, B.H., 2018. A deep learning algorithm for prediction of age-related eye disease study severity scale for age-related macular degeneration from color fundus photography. *Ophthalmology*, 125(9), pp.1410-1420.
- [21] Abbas, Q., 2017. Glaucoma-deep: detection of glaucoma eye disease on retinal fundus images using deep learning. *Int J Adv Comput Sci Appl*, 8(6), pp.41-5.
- [22] Poplin, R., Varadarajan, A.V., Blumer, K., Liu, Y., McConnell, M.V., Corrado, G.S., Peng, L. and Webster, D.R., 2018. Prediction of cardiovascular risk factors from retinal fundus photographs via deep learning. *Nature Biomedical Engineering*, 2(3), pp.158-164.
- [23] Raman, R., Srinivasan, S., Virmani, S., Sivaprasad, S., Rao, C. and Rajalakshmi, R., 2019. Fundus photograph-based deep learning algorithms in detecting diabetic retinopathy. *Eye*, 33(1), pp.97-109.
- [24] Sayres, R., Taly, A., Rahimy, E., Blumer, K., Coz, D., Hammel, N., Krause, J., Narayanaswamy, A., Rastegar, Z., Wu, D. and Xu, S., 2019. Using a deep learning algorithm and integrated gradients explanation to assist grading for diabetic retinopathy. *Ophthalmology*, 126(4), pp.552-564.
- [25] Schlegl, T., Waldstein, S.M., Bogunovic, H., Endstraßer, F., Sadeghipour, A., Philip, A.M., Podkowinski, D., Gerendas, B.S., Langs, G. and Schmidt-Erfurth, U., 2018. Fully automated detection and quantification of macular fluid in OCT using deep learning. *Ophthalmology*, 125(4), pp.549-558.
- [26] Ting, D.S.W., Cheung, C.Y.L., Lim, G., Tan, G.S.W., Quang, N.D., Gan, A., Hamzah, H., Garcia-Franco, R., San Yeo, I.Y., Lee, S.Y. and Wong, E.Y.M., 2017. Development and validation of a deep learning system for diabetic retinopathy and related eye diseases using retinal images from multiethnic populations with diabetes. *Jama*, 318(22), pp.2211-2223.
- [27] Hasib, M.H., Sultana, T. and Chowdhury, C., 2020. *Efficient image processing and machine learning approach for predicting retinal diseases* (Doctoral dissertation, Brac University).
- [28] Bhuiyan, M., Rahman, A., Ullah, M. and Das, A.K., 2019. iHealthcare: Predictive model analysis concerning big data applications for interactive healthcare systems. *Applied Sciences*, 9(16), p.3365.
- [29] Labib, M.F., Rifat, A.S., Hossain, M.M., Das, A.K. and Nawrine, F., 2019, June. Road accident analysis and prediction of accident severity by using machine learning in Bangladesh. In *2019 7th International Conference on Smart Computing & Communications (ICSCC)* (pp. 1-5). IEEE.
- [30] Thapa, D., Raahemifar, K. and Lakshminarayanan, V., 2015. Reduction of speckle noise from optical coherence tomography images using multi-frame weighted nuclear norm minimization method. *Journal of Modern Optics*, 62(21), pp.1856-1864.
- [31] Pamar, R., 2018. *Demystifying Convolutional Neural Networks, towards data science*, accessed 12 October 2021, Website: <https://towardsdatascience.com/demystifying-convolutional-neural-networks-384785791596>.
- [32] Mooney, Paul.(2017, October). *Retinal OCT Images (Optical Coherence Tomography)*, Version 2. accessed July 20,2021 , Website: [www.kaggle.com/paultimothymooney/kermany2018](http://www.kaggle.com/paultimothymooney/kermany2018).
- [33] Ullah, M.R., Bhuiyan, M.A.R. and Das, A.K., 2017, September. IHEMHA: Interactive healthcare system design with emotion computing and medical history analysis. In *2017 6th International Conference on Informatics, Electronics and Vision & 2017 7th International Symposium in Computational Medical and Health Technology (ICIEV-ISCMHT)* (pp. 1-8). IEEE.
- [34] Emon, E.A., Rahman, S., Banarjee, J., Das, A.K. and Mitra, T., 2019, June. A deep learning approach to detect abusive bengali text. In *2019 7th International Conference on Smart Computing & Communications (ICSCC)* (pp. 1-5). IEEE.
- [35] Drovo, M.D., Chowdhury, M., Uday, S.I. and Das, A.K., 2019, June. Named entity recognition in bengali text using merged hidden markov model and rule base approach. In *2019 7th International Conference on Smart Computing & Communications (ICSCC)* (pp. 1-5). IEEE.
- [36] Khan, M.S.S., Rafa, S.R. and Das, A.K., 2021. Sentiment Analysis on Bengali Facebook Comments To Predict Fan's Emotions Towards a Celebrity. *Journal of Engineering Advancements*, 2(03), pp.118-124.
- [37] Islam, S., Khan, S.I.A., Abedin, M.M., Habibullah, K.M. and Das, A.K., 2019, July. Bird species classification from an image using VGG-16 network. In *Proceedings of the 2019 7th international conference on computer and communications management* (pp. 38-42).

This page is left intentionally blank

# Journal of Engineering Advancements (JEA)

DOI: <https://doi.org/10.38032/jea>

---

Indexed by:



Volume 02 Issue 04

DOI: <https://doi.org/10.38032/jea.2021.04>

---

**Published by: SciEn Publishing Group**

Website: [www.scienpg.com](http://www.scienpg.com)